学位論文

Suzaku Studies of Mass Accretion Flows in Weakly-Magnetized Neutron Star Binaries

(「すざく」による弱磁場中性子星連星における質量降着流の研究)

平成26年12月　博士 (理学) 申請

東京大学大学院理学系研究科

物理学専攻

櫻井 壮希

Abstract

In order to clarify the physics of accretion flows onto weakly-magnetized neutron-star (NS) binaries, so-called Low-Mass X-ray Binaries (LMXBs), we investigated their *Suzaku* broad-band spectra spanning < 1 keV to $\gtrsim 100$ keV. We mainly focused on their hard state utilizing 17 spectra of 8 LMXBs, which were obtained from the *Suzaku* archive. The luminosity $L_{\rm x}$ of the data sets ranges from 10^{32} erg s^{-1} to 10^{38} erg s^{-1}.

Over the wide range of $L_{\rm x}$, all the spectra were expressed successfully and in a unified way by at most three ingredients: emission from an optically-thick accretion disk, blackbody (BB) from the NS surface, and a Comptonizing corona. The BB emission was found to be always Comptonized, while the disk emission is Comptonized only in a certain luminosity range of $L_{\rm x} \sim 10^{37}$ erg s^{-1}. When $L_{\rm x} \gtrsim 10^{36}$ erg s^{-1}, the disk has an innermost temperature of ~ 0.3 keV, and is truncated at a radius $R_{\rm in} \gtrsim 20$ km. The BB emission has a radius $R_{\rm bb}$ which is consistent with the canonical NS radius ($R_{\rm bb} \sim 10$ km $= R_{\rm NS}$) and a temperature of ~ 0.5 keV, and is strongly Comptonized by the corona with a temperature of $T_{\rm e} \sim 50$ keV and optical depth of $\tau \sim 1$. The implied view is that the optically-thick flow (i.e. the standard accretion disk) transforms, at $R_{\rm in}$, into an optically-thin and geometrically-thick flow, namely, the corona, which accretes rather spherically onto the NS surface. The heated surface emits the BB photons, which are then Compton scattered by the succeeding corona, to form the hard X-ray continuum extending to ~ 100 keV.

In the luminosity range of $L_{\rm x} < 10^{36}$ erg s^{-1}, the spectra were reproduced by Comptonized BB alone. The disk emission was not detectable possibly due to its low temperature ($T_{\rm in} \lesssim 0.1$ keV). As $L_{\rm x}$ became lower, we observed a decrease of the apparent $R_{\rm bb}$ from < 10 km down to ~ 3 km, although it may be an artificial effect due to the color hardening. In addition, the $L_{\rm x}$-dependent change of τ indicates a decrease either of the flow radial infall velocity or its cross-section at low $L_{\rm x}$. These phenomenon can be simultaneously explained the emergence of an NS magnetosphere, which funnels the flow and makes the flow cross-section (and $R_{\rm bb}$ too) smaller. Assuming an NS magnetic field strength of $\sim 10^7$ G, the Alfven radius becomes larger than 10 km at $L_{\rm x} < 10^{36}$ erg s^{-1} .

Across a hard-to-soft state transition seen in Aql X-1 data, the spectral parameters ($T_{\rm in}, R_{\rm in}, T_{\rm bb}, R_{\rm bb}, T_{\rm e}$, and τ) were found to change rapidly but continuously. The energetics of the system changed from Compton-dominant ($\sim$ half $L_{\rm x}$ is carried by the corona) to disk-dominant ($\sim 0.5 L_{\rm x}$ is carried by the disk emission, in turn) scheme. We introduced a new parameter $Q = T_{\rm e}/T_{\rm bb}$ proposed by Makishima (2014), which clearly divides the soft state and the hard state. In the $Q - y$ diagram, all the sources were found to line up along a single locus, regardless of their spectral state.

In conclusion, we have successfully constructed a unified picture of the LMXBs in their hard state, and clarified how it connects the previously established view of the soft state.

Contents

List of Figures

List of Tables

Chapter 1

INTRODUCTION

Neutron stars (NSs) are one of the most attractive celestial objects in various aspects of science. They form a crucial subject in nuclear physics as the heaviest nuclei in the universe. In terms of astrophysics, they are of importance as one of the fates of nuclear-burning stars, and provide a unique laboratory of various high-energy phenomena, including matter-radiation interactions and fluid dynamics under extremely strong gravity. The present thesis focuses on the third topic, namely the physics of accretion flows around neutron stars, by investigating radiation from the flow. As a target of such studies, we selected low-mass X-ray binaries (LMXBs) where a NS with weak magnetic field ($< 10^9$ G) forms a binary system with a low-mass star ($\lesssim 1 M_\odot$). LMXBs provide an ideal opportunity to study accretion physics, because they have a clear advantage over black hole binaries (BHBs) that accreting matter radiates all the gravitational energy of ~ 200 MeV/nucleon finally at the NS surface, while that in BHBs can disappear into the event horizon, carrying some (and often unknown) fraction of the released energy. Since thermalized matter in the system typically has a temperature of ~ 1 keV, X-rays provide the best probe to the accretion flows therein.

Like BHBs, LMXBs are known to exhibit two spectral states; the "soft state" when the mass accretion rate is high (with the luminosity of $L > 10^{37}$ erg s^{-1}), and the "hard state" with $L \lesssim 10^{37}$ erg s^{-1}. The former literally exhibits a bright soft spectrum confined in $\lesssim 20$ keV, whereas the latter fainter and much hard spectrum extending to > 100 keV. Studies of accreting flows in LMXBs have made a steady progress since the 1980s. In particular, their soft state has been extensively studied, and the results have converged to a firm picture (Mitsuda et al. 1984). The accreting matter forms a flat, optically thin "standard" accretion disk down to the NS surface, in which about half the gravitational energy is released in the form of multi-color blackbody radiation. The remaining half, once stored in the Keplerian kinetic energy of the accreting matter, is finally radiated as blackbody radiation when it plunges onto the NS surface. This

progress of the soft-state studies was driven by instruments such as *Tenma* (Tanaka et al. 1984) and *Ginga* (Makino 1987), which provided high-quality spectral information of up to ~ 20 keV in the early era.

Contrary to those of the soft state, studies of the hard state have been hampered until the beginning of the 2000s. This is because the hard-state LMXBs are often faint as $L < 10^{36}$ erg s^{-1} and exhibit hard spectra extending over a broad energy band up to 100 keV, while there were few instruments sensitive above 20 keV. Since then, the hard X-ray instrumentation has made a significant progress. Especially, *Suzaku* (Mitsuda et al. 2007) is the most suitable tool for hard state studies, because the combination of X-ray Imaging Spectrometer (XIS; Koyama et al. 2007) and Hard X-ray Detector (HXD; Takahashi et al. 2007) onboard *Suzaku* provides broad-band and high-quality spectra from < 1 keV to > 100 keV, which is essential for investigating the hard state. Working in orbit for nearly 10 years since the launch in 2005 July, *Suzaku* has been observing a fair number ($\gtrsim 50$) of LMXBs, covering both states, and the acquired data are available as an archive. Therefore, we utilize this precious accumulation, and try unified analysis of those acquired in the hard state of LMXBs.

The understanding of the soft state is a story in the luminosity range of 10^{37} erg s^{-1} $< L \lesssim 10^{38}$ erg s^{-1}, whereas any such a picture of the hard state needs to cover a much wider range as 10^{32} erg s^{-1} $< L \lesssim 10^{37}$ erg s^{-1}. In the present thesis, we hence investigate 17 wide-band spectra of 8 sources, which span a range of $10^{32} - 10^{37.5}$ erg s^{-1}. We already analyzed some of the data sets for a particular object Aql X-1, and obtained a promising working hypothesis (Sakurai et al. 2012, 2014). In the present thesis, we strengthen and further develop this view through much more extensive and comprehensive data analysis, trying to explain the accretion dynamics in a unified way as a function of luminosity. Moreover, fortunately, one of the Aql X-1 data caught a very precious moment of the hard-to-soft transition; the details of the transition are also addressed in our comprehensive study.

Chapter 2

REVIEW

2.1 Low-Mass X-ray Binaries

2.1.1 Overview

A Low-Mass X-ray Binary, hereafter LMXB, is an X-ray emitting binary system consisting of a low-mass star hosting and a mass-accreting neutron star (NS). The mass-donating stars (or called "companions") are main-sequence stars of spectral types A, F, or later ($\lesssim 1M_{\odot}$). As LMXBs are often found in globular clusters, they are thought to be aged systems belong to population II. Since such type of stars do not have strong stellar winds, mass transfer in LMXBs is considered to occur via so-called Roche lobe overflow. As illustrated in figure 2.1, a particular potential contour (called separatrix) around the two stars has a shape like "8", taking the first Lagrangian point as a pivot (saddle point). The gas of the companion passes through that point and flows onto the NS.

The matter accreting onto the NS is thermalized and cooled via radiation. Let us demonstrate that a typical photon energy emitted by an LMXB falls in the X-ray band. For a compact star with mass of M and accreting matters with solar abundance, the Eddington luminosity at which the gravity is balanced by radiation pressure, is given as

$$L_{\rm edd} = 1.5 \times 10^{38} \left(\frac{M}{M_{\odot}} \right) \ {\rm erg \ s^{-1}}, \tag{2.1}$$

and is calculated as $L_{\rm edd} = 2.1 \times 10^{38}$ erg s^{-1} for the canonical NS mass of $1.4M_{\odot}$. When this is carried by blackbody (BB) emission with a typical area of $4\pi R_{\rm NS}^2$, the BB

temperature ($T_{\rm bb}$) is estimated as

$$\sigma T_{\rm bb}^4 = \frac{L_{\rm edd}}{4\pi R_{\rm NS}^2} \quad \Rightarrow \quad T_{\rm bb} = 2.00 \text{ keV} \simeq 2.3 \times 10^7 \text{ K}, \tag{2.2}$$

where $R_{\rm NS} = 10$ km is the canonical NS radius and σ is the Stefan-Boltzmann constant. This corresponds to the local Eddington temperature at the NS surface. Thus, the typical photon energy is estimated to be of the order of $\sim$ keV, which is right in the X-ray wavelengths,

An NS in LMXBs is considered to have magnetic fields as low as $B \lesssim 10^9$ G, Therefore, the accreting matter is almost free from magnetic pressure, only obeying the gravity, the centrifugal force, and the gas pressure. As a result, LMXBs seldom show X-ray pulsations at the spin period (typically $\sim$ 10 ms) of the NSs. For reference, a High-Mass X-ray Binary (HMXB), in which the mass donor is a massive O- or B- type star, usually has a strongly magnetized ($B \sim 10^{12}$ G) NS as the compact component, and exhibits clear X-ray pulsations with a period of $\gtrsim 1$ s.

Since the discovery of Sco X-1 by Giacconi et al. (1962) as the first cosmic X-ray source, more than 150 LMXBs have been found so far (Liu et al. 2007, for a catalogue), mostly with the help of *Uhuru* (Giacconi et al. 1971; Forman et al. 1978). Their X-ray emission has been well studied since 1980s, with *Tenma* (Tanaka et al. 1984), *EXOSAT* (White & Peacock 1988), *Ginga* (Makino 1987), and succeeding instruments. In this section, we review major studies of LMXBs performed in the past with these satellites.

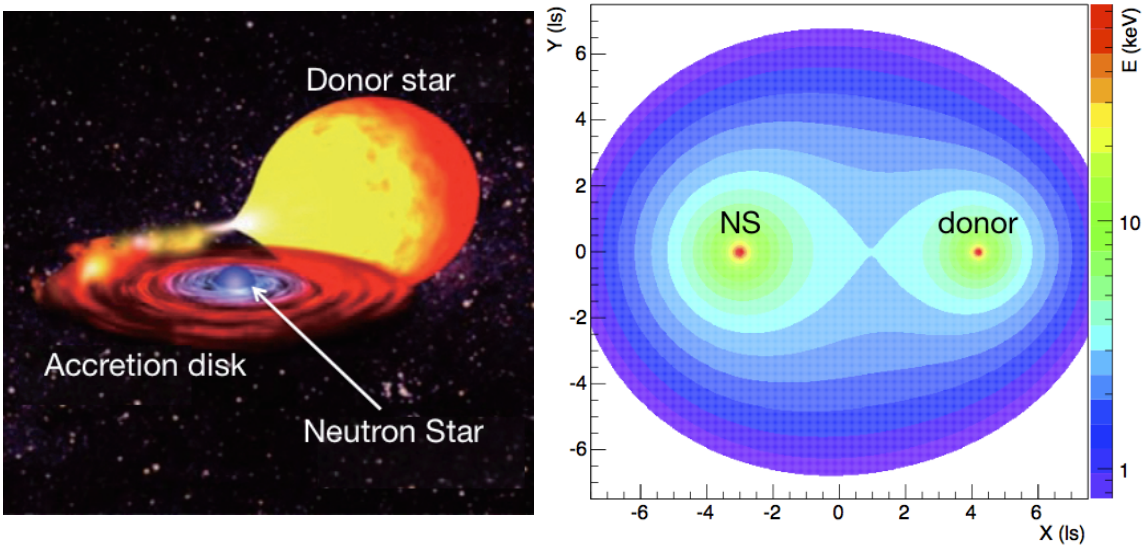

Figure 2.1: A drawing of an LMXB (left panel) and a contour of the energy potential (sign inversed) for a proton in the system (right panel). The left picture is taken from a web site (http://www.kmi.nagoya-u.ac.jp/jpn/spotlight/spotlight02.php) and modified. The right panel was calculated by assuming mass of $1.4M_\odot$ and $1M_\odot$ for the NS and the donor star, respectively. The effect of cetrifugal force is ignored.

2.1.2 X-ray Spectra

Since the 1980s, it has been known that LMXBs exhibit two different types of spectra, or spectral "states", depending on the mass accretion rate (White & Mason 1985; Mitsuda & Tanaka 1986; Mitsuda et al. 1989). As shown in figure 2.2, spectra of the two states are clearly different: the red one has a high flux in the soft band of $\lesssim$ 10 keV, while the black has power-law-like shape with a photon index of $\Gamma \sim 2$, with their cross-over located around 20 keV. Literally, the former (red) is called "soft state", and the latter "hard state". The object is more luminous when in the soft state, with a luminosity of $> 0.1 L_{\rm edd}$, while that of the hard state typically $\lesssim 0.01 L_{\rm edd}$.

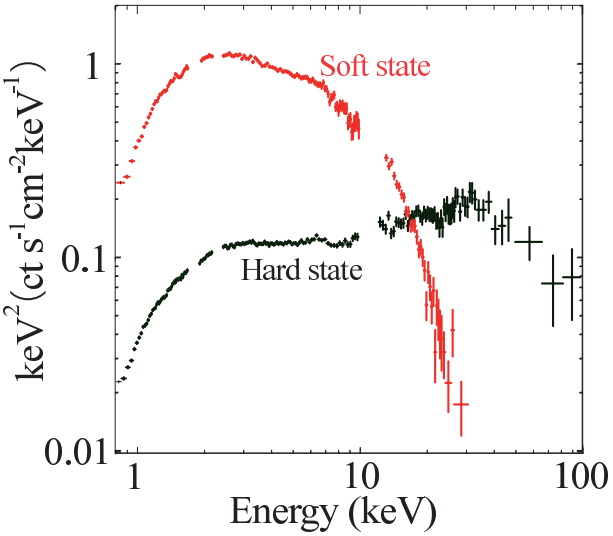

Figure 2.2: Spectra (in $\nu F\nu$ form) of the LMXB Aql X-1 in the soft state (red) and in the hard state (black), obtained with *Suzaku*. Analyses of these spectra are presented in Chapter 5.

The soft-state spectra have been extensively studied from as early as the 1980s, when a breakthrough was achieved with *Tenma*. Figure 2.3 shows a light curve and spectra of the LMXB Sco X-1 (Mitsuda et al. 1984, hereafter M84). As shown in panel (a), the source intensity was found to exhibit larger variations in a hard band of $\gtrsim$ 3 keV, than in a soft band below 3 keV. In panel (b), two spectra, accumulated when the source was brighter and fainter in $>$ 10 keV, are compared; the ratio increases towards higher energies, and becomes constant at $>$ 10 keV. This indicated the presence of a hard spectral component that varies in intensity while keeping the spectral shape. Thus, as shown in panel (c), M84 succeeded in decomposing the overall emission into a variable hard component, and a softer stable one. The varying component was found to be a BB with temperature of $T_{\rm bb} \sim 2$ keV, which is considered to originate from the NS surface. The stable one was explained by a multi-color disk emission (see §2.2.2) with its innermost temperature of $T_{\rm in} \sim 1.5$ keV. Later, the BB component was found to be

affected by inverse Comptonization (Mitsuda et al. 1989; Nakamura et al. 1989, ; §2.3). These results have been repeatedly reconfirmed by studies with succeeding instruments (e.g. Makishima et al. 1989; Lavagetto et al. 2004; Takahashi et al. 2011; Sakurai et al. 2012; Mück et al. 2013).

As demonstrated by figure 2.2, an LMXB is fainter by an order of magnitude in $<$ 10 keV in the hard state than in the soft state, while the opposite is true in the hard band of $>$ 20 keV. Since there were few instruments sensitive to hard X-rays above 20 keV, the hard state remained poorly understood until the end of 1990s. Nowadays, hard-state studies are making progress with the help of *BeppoSAX* (Boella et al. 1997), *RXTE* (Bradt et al. 1993), *INTEGRAL* (Winkler et al. 2003), and *Suzaku* (Mitsuda et al. 2007). It has been suggested that the hard-state spectra are also composed of two emission components, a soft optically-thick component and a hard power-law-like component: some studies pointed out that the soft component is either a BB or disk emission, and hard one the Comptonized BB (e.g. Guainazzi et al. 1998; in 't Zand et al. 1999; Gierlinski & Done 2002; Barret et al. 2003a; Tarana et al. 2008; Raichur et al. 2011; Tarana et al. 2011a). However, the interpretation of the spectra is not yet settled, partly because different interpretations can often describe the observed spectra with a similar degree of success (often called "model degeneracy"), particularly when the available energy band is limited. Thus, the hard state of LMXBs has been waiting for comprehensive understandings and a unified interpretation, just as was given to the soft state 3 decades ago. As already demonstrated by Sakurai et al. (2012, 2014), a great leap has been brought about by the *Suzaku* observatory (§3). The present thesis tries to construct a comprehensive *Suzaku* view of LMXBs in the hard state.

2.1.3 Phenomenological classification

Aside from the spectral studies with e.g. *Tenma* and *Ginga* (§2.1.2), an emipirical classification scheme of LMXBs in X-rays was employed in *EXOSAT* studies by(Hasinger & van der Klis 1989, ; hereafter H89), who produced Color-Color Diagrams (CCDs) for many LMXBs. A CCD is a plot between "soft color" and "hard color", where "color" means an intensity ratio of a certain band to another softer band. In H89, energy bands of $(3-4.5$ keV$)/(1-3$ keV$)$ and $(6-20$ keV$)/(4.5-6$ keV$)$ were employed for the soft color and the hard color, respectively. Since energy-independent intensity changes cancel out in the ratios, a CCD can visualize how the spectrum changes in shape as the source varies (i.e. moves on the plane), and to compare the variability/spectral characteristics among different sources. Examples of CCDs by H89 are reproduced in figure 2.4 and figure 2.5. They found that LMXBs can be classified into two types, according to the shapes of their loci on a CCD. One, exemplified in figure 2.4, is called "Z" source, of

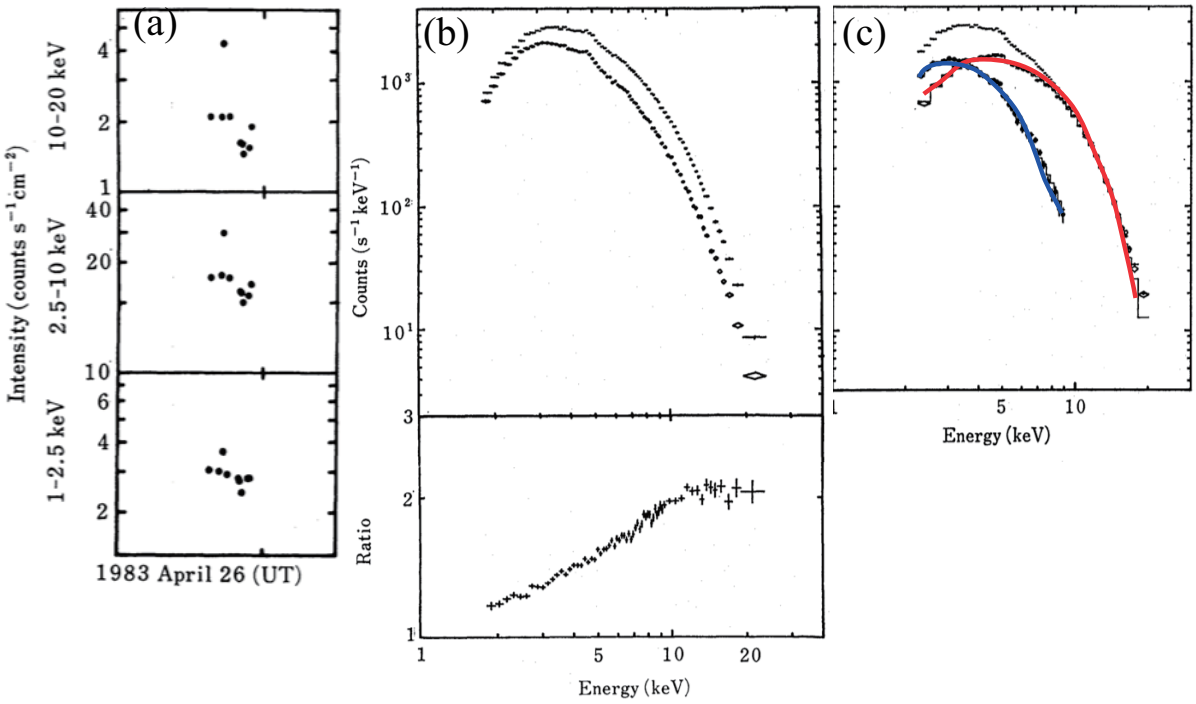

Figure 2.3: Light curves and spectra of Scorpius X-1 obtained with *Tenma*. (a) Light curves binned with $10-30$-min in three energy bands, $1-2.5$ keV (bottom), $2.5-10$ keV (middle), and $10-20$ keV (top). (b) Response-inclusive X-ray spectra in the high-intensity periods (crosses) and in the other periods (diamonds), with their ratios in the lower panel. (c) Difference between the two spectra in (b) fitted with a BB model (red), and a complementary soft component fitted with `diskBB` (blue). These figures are taken from Mitsuda et al. (1984).

which the data points form a "Z"-like shape. The loci are continuous, and consist of horizontal branch (HB in the figure), normal branch (NB), and flaring branch (FB). The other shown in figure 2.5 is named "Atoll" source because its shape looks like coral atolls. Unlike that of "Z"-source, the loci of "atoll"-sources are separated mainly into two, "island" (I in the figure) and "banana" (UB and LB).

As revealed by Takahashi (2004), Takahashi et al. (2011), and several others (e.g. Gierlinski & Done 2002; Lin et al. 2007), these empirical classifications can be translated into more physical descriptions: the Z-sources and atoll sources differ only in their luminosity, where the former correspond to $\sim L_{\rm edd}$, while the latter to $0.1 - 0.5 L_{\rm edd}$ (banana) and $\lesssim 0.1 L_{\rm edd}$ (island). Since the present thesis aims at physical descriptions of LMXBs rather than their empirical classification, we do not use CCDs in the present thesis; neither do we consider whether a source is a Z-type object or an atoll-type one.

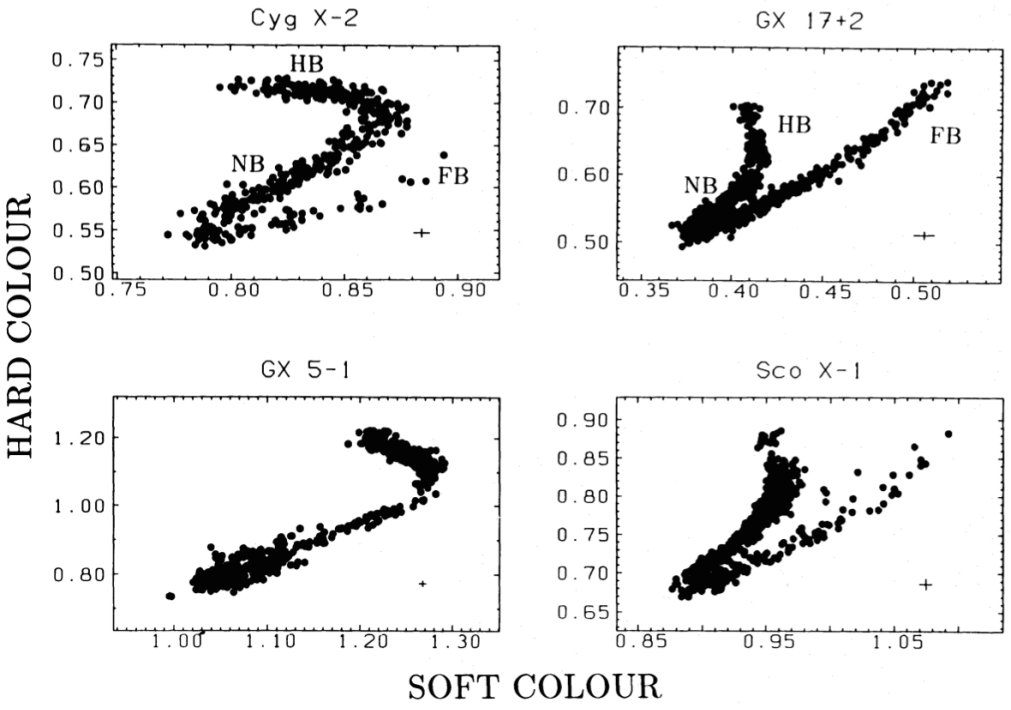

Figure 2.4: CCDs of four typical Z sources with *EXOSAT*. The energy bands of soft color and hard color are $(3 - 4.5\text{keV})/(1 - 3\text{keV})$ and $(6 - 20\text{keV})/(4.5 - 6\text{keV})$, respectively. The figures are taken from Hasinger & van der Klis (1989).

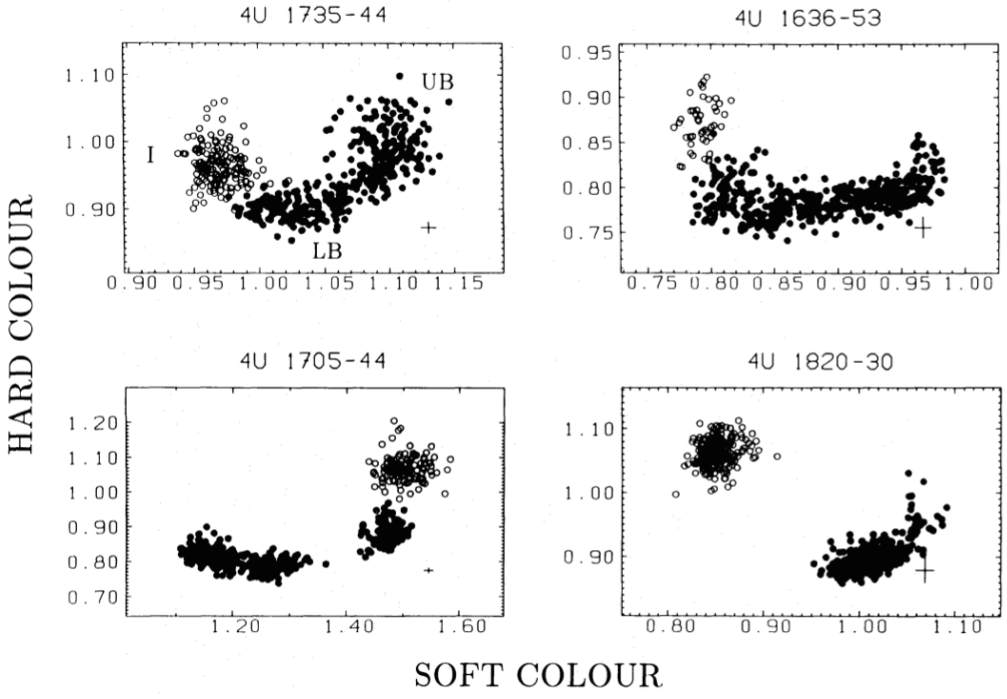

Figure 2.5: Same as figure 2.4 with four atoll sources. The figures are taken from Hasinger & van der Klis (1989).

2.2 Accretion Disk

In many of the accreting binary systems like LMXBs and BHBs, matters from the mass donating component form an accretion disk around the accreting component because of their angular momentum. After the concept of accretion disk was first proposed by Lynden-Bell (1969), Shakura & Sunyaev (1973) constructed a model called "standard accretion disk" which assumes geometrically-thin and optically-thick matter flows. In this section, we explain this concept of standard accretion disk model.

2.2.1 Standard accretion disk

In general, mainly four forces act on a matter in the accretion disk; the gravity, the centrifugal force, the Coriolis force, and pressure gradient. In the standard accretion disk model (Shakura & Sunyaev 1973), it is assumed that the radial velocity is negligible (i.e. no Coriolis force) and the radial pressure gradient is much lower than the gravity. This approximation is considered valid when the mass accretion rate $\dot{M}$ is lower than the Eddington rate, namely the luminosity is lower than the Eddington luminosity (equation 2.1), and yet high enough so that the matter can radiate efficiently. As a result, motion of the matter becomes Keplerian, and the overall flow forms an geometrically-thin disk.

Since the Keplerian angular velocity ($\propto \sqrt{GM/r^3}$) decreases with r, the disk rotation is not rigid but differential. Matters rotating at r have a higher angular velocity than those at $r + dr$, so that the angular momentum of the former is transferred to the latter via friction, i.e. viscosity. The viscosity generates heat which is assumed to be efficiently conducted to the disk surface, and radiated away as a blackbody emission. Since the heating by viscosity and the cooling by radiation is balanced, the heat and the Stefan-Boltzmann flux from both sides of the disk should be equated, and the innermost temperature is obtained as

$$T(r) = \left\{ \frac{3GM\dot{M}}{8\pi r^3 \sigma} \left(1 - \sqrt{\frac{r_{\rm in}}{r}} \right) \right\}^{\frac{1}{4}}, \tag{2.3}$$

where σ is the Stefan-Boltzmann constant, G is the gravitational constant, M is mass of a central compact star, and $r_{\rm in}$ is an innermost disk radius.

The flux $f(E)$ observed at a distance d from the source is obtained by integrating the local blackbody radiation over various disk radii (hence over T), and has a dependence on the inclination i as

$$f(E) = \frac{\cos i}{d^2} \int_{r_{\rm in}}^{r_{\rm out}} 2\pi r I(E;T) dr, \tag{2.4}$$

where

$$I(E;T) = \frac{2}{(h^3c^2}\frac{E^3}{e^{\frac{E}{kT}}-1} \tag{2.5}$$

is the blackbody flux density (i.e. per unit energy) emitted per unit solid angle.

2.2.2 Multi-Color Disk approximation

As an approximate treatment of equation 2.3, Multi-Color Disk (MCD) model (Mitsuda et al. 1984; Makishima et al. 1986) ignores the $\sqrt{r_{\rm in}/r}$ term, and assumes

$$T_{\rm mcd} = \left(\frac{3GM\dot{M}}{8\pi r^3\sigma}\right)^{\frac{1}{4}} := T_{\rm in}\left(\frac{r}{r_{\rm in}}\right)^{-3/4} \quad (r > r_{\rm in}) \tag{2.6}$$

where $T_{\rm in}$ is the inner edge temperature. Since the boundary condition at the inner radius is different from that of the genuine standard disk, $r_{\rm in}$ in the MCD model should be converted to the true $R_{\rm in}$ by

$$R_{\rm in} = \xi\kappa^2 r_{\rm in} \simeq 1.19\left(\frac{\xi}{0.41}\right)\left(\frac{\kappa}{1.7}\right)^2 r_{\rm in}, \tag{2.7}$$

where $\xi = 0.41$ is a correction factor for the inner edge temperature obtained by regarding $T_{\rm in}$ as the maximum temperature in equation 2.3 (Kubota et al. 1998), and $\kappa = 1.7$ is "color hardening factor" due to up-scatterings by electrons in the disk (Shimura & Takahara 1995). By substituting this $T_{\rm mcd}$ into equation 2.4, the energy flux density integrated from $r_{\rm in}$ to $r \to +\infty$ is calculated as

$$\begin{aligned} f_{\rm mcd}(E) &= \frac{\cos i}{d^2}\int_{r_{\rm in}}^{\infty} 2\pi r I(E;T_{\rm mcd})dr \\ &= \frac{16\pi r_{\rm in}^2 (kT_{\rm in})^3\cos i}{3d^2h^3c^2}\left(\frac{E}{kT_{\rm in}}\right)^{\frac{1}{3}}\int_{\frac{E}{kT_{\rm in}}}^{\infty}\frac{x^{\frac{5}{3}}}{e^x-1}dx. \end{aligned} \tag{2.8}$$

At $E \ll kT_{\rm in}$ where the last (integration) factor can be regarded as constant, the MCD model hence has an energy index of 1/3 which corresponds to a photon index of $-2/3$ and a slope of 4/3 in the $\nu F\nu$ presentation (Makishima et al. 1986). While in $E \gg kT_{\rm in}$, the last factor exponentially decreases. Hence, as shown in figure 2.6, an overall spectral shape of the MCD is like a power law with photon index of $-2/3$ and a cutoff around $E = kT_{\rm in}$. Later in Chapter 5, we utilize `diskBB` code (Mitsuda et al. 1984; Makishima et al. 1986) which provides above MCD spectrum, for quantitative evaluations of observed spectra of LMXBs.

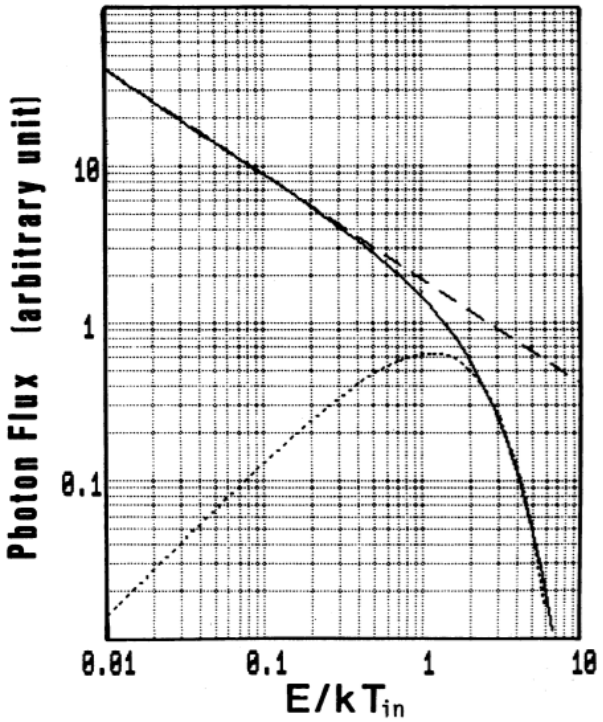

Figure 2.6: A photon spectrum of the MCD (solid line). The dotted and broken lines represent a blackbody spectrum with temperature of $0.71T_{\rm in}$ and a power law with photon index of $-2/3$, respectively. The figure is taken from Makishima et al. (1986).

As the matter at r is considered as an isolated and pure gravitational system in a bounded orbit, it must obey the virial theorem

$$< K > + \frac{1}{2} < \Omega >= 0 \tag{2.9}$$

which describes the relation between time averages of the kinetic energy K and gravitational energy Ω. When the radial velocity is neglected, this relation is considered to hold at each r. Therefore, the kinetic energy of matter (with mass of m) at $r = r_{\rm in}$ should be just half $GMm/r_{\rm in}$. In other words, the total luminosity which the disk emits over $r = [r_{\rm in}, \infty]$ must be

$$L_{\rm d} = \frac{GM\dot{M}}{2r_{\rm in}}. \tag{2.10}$$

This can be also confirmed by integrating equation 2.8 over E.

2.3 Comptonization

Like BHBs and other accreting systems, LMXBs often exhibit cutoff-PL-like spectra which are considered to arise via inverse Comptonization of optically-thick emission from either the disk or the NS surface, by some hotter electrons.

2.3.1 Compton kinematics

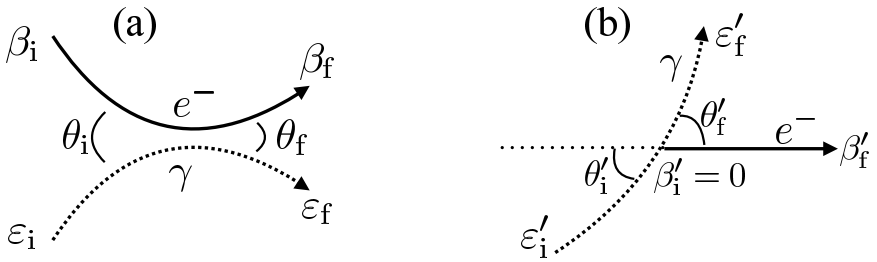

Figure 2.7: A schematic diagram of Compton scattering in the laboratory frame (panel a) and the electron rest system (panel b).

A Compton scattering between a photon and an electron, with the electron speed of β_i and a scattering angle of θ_i indicated in figure 2.7, changes the photon energy ε_i into a final-state energy as

$$\begin{aligned}\varepsilon_\mathrm{f}(\theta'_\mathrm{f},\phi;\varepsilon_\mathrm{i},\beta_\mathrm{i}) &= \frac{\varepsilon_\mathrm{i}\gamma_\mathrm{i}(1-\beta_\mathrm{i}\cos\theta_\mathrm{i})}{1+\frac{\varepsilon_\mathrm{i}\gamma_\mathrm{i}(1-\beta_\mathrm{i}\cos\theta_\mathrm{i})}{m_\mathrm{e}c^2}(1-\cos\theta'_\mathrm{f})} \\ &\quad\times\gamma_\mathrm{i}(1+\beta_\mathrm{i}(\cos\theta'_\mathrm{i}\cos\theta'_\mathrm{f}-\sin\theta'_\mathrm{i}\sin\theta'_\mathrm{f}\cos\phi)),\end{aligned} \tag{2.11}$$

where

$$\theta'_\mathrm{i}=\tan^{-1}\left(\frac{\sin\theta_\mathrm{i}}{\gamma_\mathrm{i}(\cos\theta_\mathrm{i}-\beta_\mathrm{i})}\right),$$

$m_\mathrm{e}c^2=511$ keV is the electron rest mass, and ϕ is the twist angle of $\vec{\varepsilon}'_\mathrm{f}$ around $\vec{\beta}'_\mathrm{f}$ in the electron rest system. By assigning $\beta_\mathrm{i}=0$, equation 2.11 reduces to the formula for "normal" Compton scattering

$$\varepsilon_\mathrm{f}=\frac{\varepsilon_\mathrm{i}}{1+\frac{\varepsilon_\mathrm{i}}{m_\mathrm{e}c^2}(1-\cos\theta)}$$

where the photon always loses its energy. On the other hand, when the electron is relativistic ($\beta_\mathrm{i}\sim 1$ or $\gamma_\mathrm{i}=1/\sqrt{1-\beta_\mathrm{i}^2}\gg 1$), the photon can take much energy from the electron as $\varepsilon_\mathrm{f}/\varepsilon_\mathrm{i}\propto\gamma_\mathrm{i}^2$, which is called "inverse" Comptonization.

2.3.2 Comptonization of monochromatic photons

Consider Comptonization effect on a seed photon source which emits monoenergetic photons with energy of ε. When the source is covered with a hot thermal electron cloud (hereafter "corona") with temperature of $T_{\rm e}$, a fraction of the photons are Compton-scattered in the corona, and their energy is changed from ε according to equation 2.11. The resulting emission depends on the electron energy distribution and the (mean) number of scatterings. The former is determined by $T_{\rm e}$, and the latter is usually characterized by optical depth

$$\tau = \sigma_{\rm T} n_{\rm e} l, \tag{2.12}$$

where $\sigma_{\rm T}$ is the Thomson cross-section, $n_{\rm e}$ is electron number density in the corona, and l is a characteristic size of the corona which corresponds to the radius if spherical. Since the number of scatterings (or opacity of the corona) increases with τ, the photons can gain more energies with larger τ.

Figure 2.8 shows schematic spectra of Comptonization of monochromatic photons ($\varepsilon = kT_{\rm s}$). As shown in panel (a), when τ is moderately small as $\tau \lesssim 1$, the resulting spectrum in the hard band ($E > kT_{\rm s}$) becomes a power law with a cut off. The photon index of the power law is determined by a product of $T_{\rm e}$ and τ as

$$\Gamma = -\frac{1}{2} + \sqrt{\frac{9}{4} + \frac{4}{y}}\ , \tag{2.13}$$

where

$$y = \frac{4kT_{\rm e}}{m_{\rm e}c^2}\max(\tau, \tau^2) \tag{2.14}$$

is called Compton y-parameter. The power-law spectrum extends up to $E \sim kT_{\rm e}$, and drops exponentially beyond. On the other hand, as shown in panel (b), the spectrum does not become a simple cutoff power law when τ is very high ($\tau \gg 1$). As equation 2.13 yields $\Gamma \to 1$ when $\tau \gg 1$, the slope becomes $2 - \Gamma = 1$. Since the photons are scattered so many times due to a large τ, the sufficient momentum transfer leads to an energy equilibrium between the photons and electrons. As a result, in higher energy range of $E \sim 3kT_{\rm e}$, the spectrum becomes blackbody-like (called Wien hump), which directly reflects the Maxwellian energy distribution of the electrons.

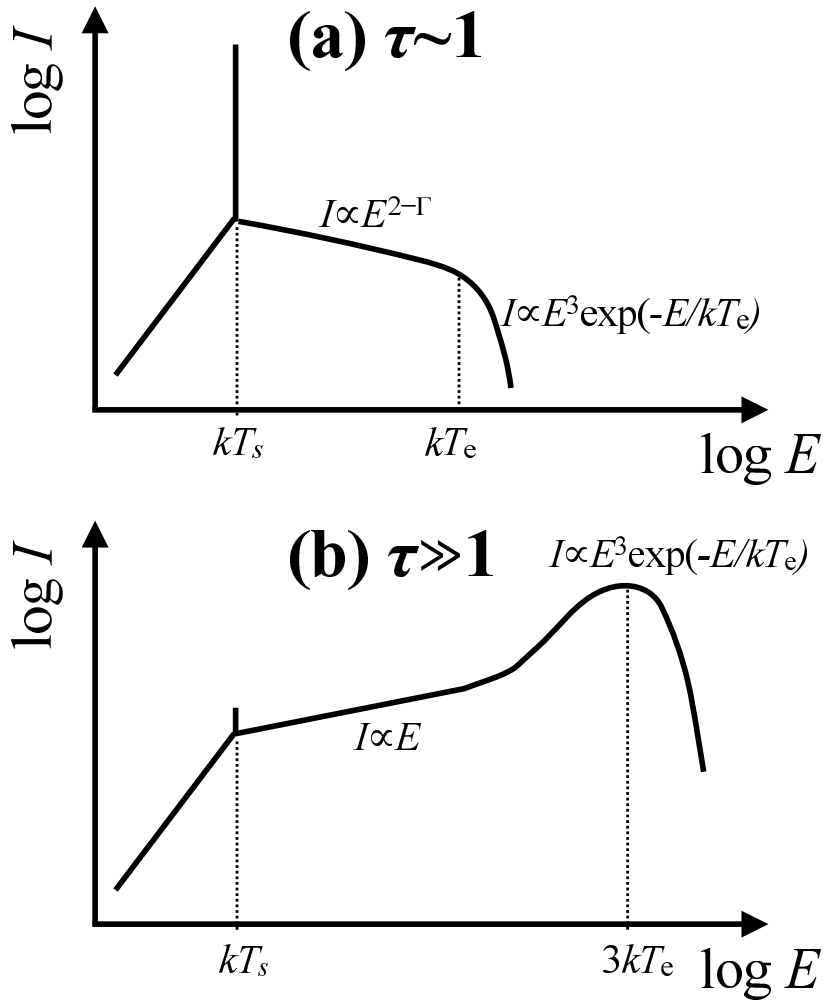

Figure 2.8: A schematic drawing of a Comptonized spectrum, when the seed photons have a monochromatic energy $kT_{\rm s}$, and the coronal temperature is $T_{\rm e}$.

2.3.3 Comptonization of thermal photons

In general applications of Comptonization to astrophysics, for instance in LMXBs and BHBs, the seed-photon source is often assumed to be blackbody emission. In this case, the resulting energy spectrum can be calculated as a convolution of the input spectrum and the result of monochromatic case described in §2.3.2. Examples of Comptonized BB spectra are shown in figure 2.9. The spectral shape in $E > kT_{\rm bb}$ approximately corresponds to that in the monochromatic-seed case, while the soft band reflects the seed spectrum. Thus, Comptonization of BB results in a spectrum where the peaks of input BB spectrum and a hidden Wien spectrum at $E \sim 3kT_{\rm e}$ are connected by a power law with Γ which is given by equation 2.13. The heights of the peaks are determined by τ, because that of the seed photons decreases with τ, while that of $E \sim 3kT_{\rm e}$ in the opposite way.

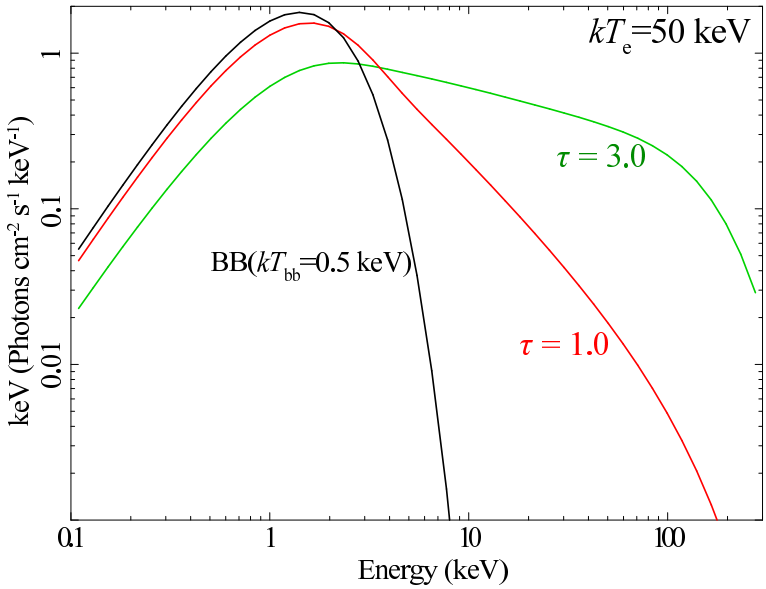

Figure 2.9: Comptonized spectra provided by `compPS` (Poutanen & Svensson 1996). The black, red, and green represents the BB seed spectrum with temperature of $T_{\rm bb} = 0.5$ keV, its Comptonization with $\tau = 1$, and that with $\tau = 3$, respectively. The corona is assumed here to be spherical and have $T_{\rm e} = 50$ keV.

As a practical and analytic method to calculate spectra reprocessed by Comptonization, numerical solutions of Kompaneets equation (Kompaneets 1956) are mostly utilized. The equation is derived from Boltzmann equation describing an evolution of phase-space densities of electrons and photons through their collisions. Applying several perturbative expansions (e.g. with $kT_{\rm e}/m_{\rm e}c^2$), it yields

$$\frac{\partial n}{\partial y} = \frac{1}{x^2}\frac{\partial}{\partial x}\{x^4(n' + n + n^2)\} \quad (x = E/m_{\rm e}c^2), \tag{2.15}$$

where n is the phase-space density of the photons and

$$y \equiv \frac{(n_{\rm e}\sigma_{\rm T}ct)kT_{\rm e}}{m_{\rm e}c^2} = \frac{\tau kT_{\rm e}}{m_{\rm e}c^2} \tag{2.16}$$

(Kompaneets 1956). In the spectral analyses in Chapter 5, we make use of a Comptonization code `nthcomp` (Lightman & Zdziarski 1987; Lightman et al. 1987; Zdziarski et al. 1996; Zycki et al. 1999), which provides numerical solutions to equation 2.15 with certain relativistic corrections.

The other code utilized in the present thesis, `compPS` (Poutanen & Svensson 1996), provides Comptonized spectra by solving a radiative transfer equation numerically. It more accurately treats relativistic effects (e.g. using Klein-Nishina cross-section), although the application range is confined as $\tau < 3$, within which its iterative calculation converges. In Chapter 5, we utilize either of these two codes to quantify observed spectra.

Chapter 3

INSTRUMENTATION

In this Chapter, we briefly introduce the *Suzaku* satellite which is utilized in the present thesis.

3.1 Overview of the *Suzaku* Observatory

The X-ray observatory *Suzaku* (Mitsuda et al. 2007) is the Japanese fifth X-ray astronomy satellite. *Suzaku* is the successor of previous four, *Hakucho* (Kondo et al. 1981), *Tenma* (Tanaka et al. 1984), *Ginga* (Makino 1987), and *ASCA* (Tanaka et al. 1994). This mission, also called *ASTRO-E2* before the launch, is a re-challenge of *ASTRO-E*, which was lost by the failure of M-V-4 rocket launch in 2000 February. As well as *ASCA*, *Suzaku* was developed by collaborating works between Japan and US.

The *Suzaku* satellite was launched in 2005 July by Japan Aerospace Exploration Agency (JAXA) from Uchinoura Space Center (USC). It was successfully put into a low earth orbit with altitude of 550 km and inclination of 32°. The satellite orbital period is 96 min. Among the ∼15 orbits a day, it contacts with USC ground system ∼ 5 times, each for 10-15 min.

As illustrated in figure 3.1, *Suzaku* has overall height of 6.5 m, with its weight of 1680 kg. Three co-aligned scientific instruments, X-Ray Spectrometer (XRS), X-ray Imaging Spectrometer (XIS), and Hard X-ray Detector (HXD), are carried inside. Although XRS have been unavailable due to a certain trouble in the helium and neon coolant tanks, the other two have been demonstrating their high performance of wide-band X-ray observations in $0.5 - 600$ keV. More than 2700 *Suzaku* observations have conducted in these 9 years. Their archival data are publicly available via DARTS[a] system.

[a] http://www.darts.isas.jaxa.jp/astro/suzaku/

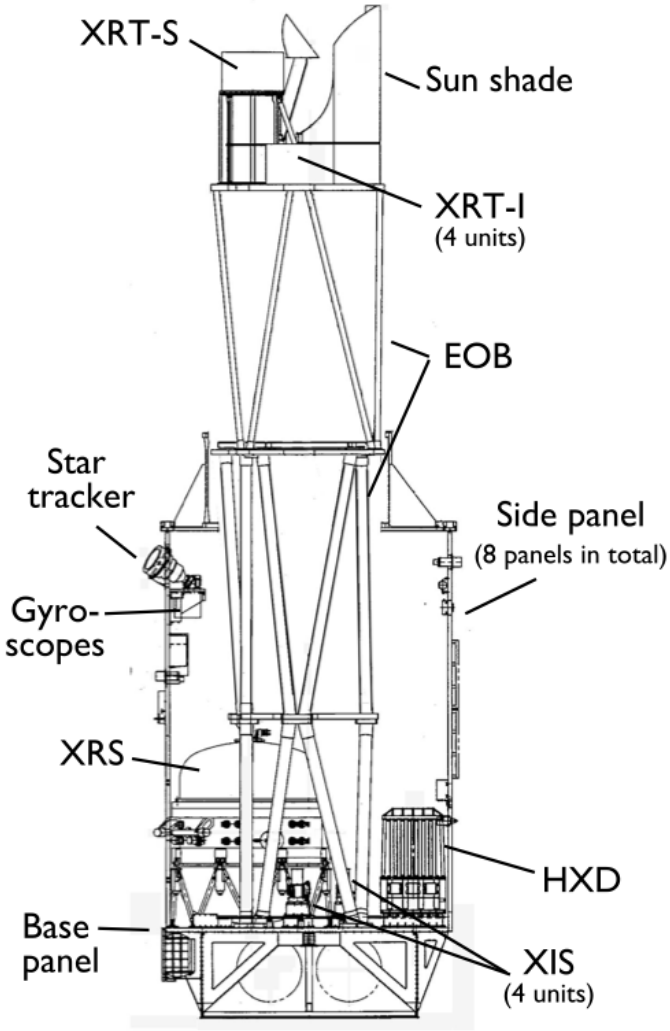

Figure 3.1: Schematic view of the *Suzaku* satellite (left) and its side view (right). The figure is taken from Mitsuda et al. (2007).

3.2 X-Ray Telescope

The X-ray Telescope (XRT; Serlemitsos et al. 2007) consists of five imaging X-ray optics mounted at an extendible optical bench as illustrated in figure 3.1. They, one of which is shown in figure 3.2 (a), are all thin-foil-nested Wolter-I type telescope (Serlemitsos 1988), which focus incoming X-rays to the XRS and the XRT placed at the focal length of 4.75 m. The one for the XRS is called XRT-S, while the other four for the XIS are labeled as XRT-I1..I4. Below, specifications of the XRT-I are addressed.

Figure 3.2 (b) shows on-axis effective areas of the XRT. Combining the four XRT-I units, the overall effective area becomes larger than that of *Chandra* (Weisskopf et al. 2000), but slightly smaller than that of *XMM* (Strider et al. 2001; Turner et al. 2001).

In the energy range of $0.8 - 10$ keV, which we utilize in the present thesis, there are a few edge-like features around 2 keV. Since the effective area is relatively uncertain in this range, the band is mostly ignored in spectral analyses in Chapter 5.

Upper panels in figure 3.3 show point-spread functions (PSFs) of the XRT-I. Their cumulative form, encircle-energy fractions (EEFs) are shown in the lower panels. Although slight scatters, EEFs of the four XRT-I reach 0.5 at the radius of ~ 1 arcmin. Thus the angular resolution of the XRT-I is $\sim 2'$ in terms of half-power diameter (HPD) within which half of the total focused X-ray photons are accumulated.

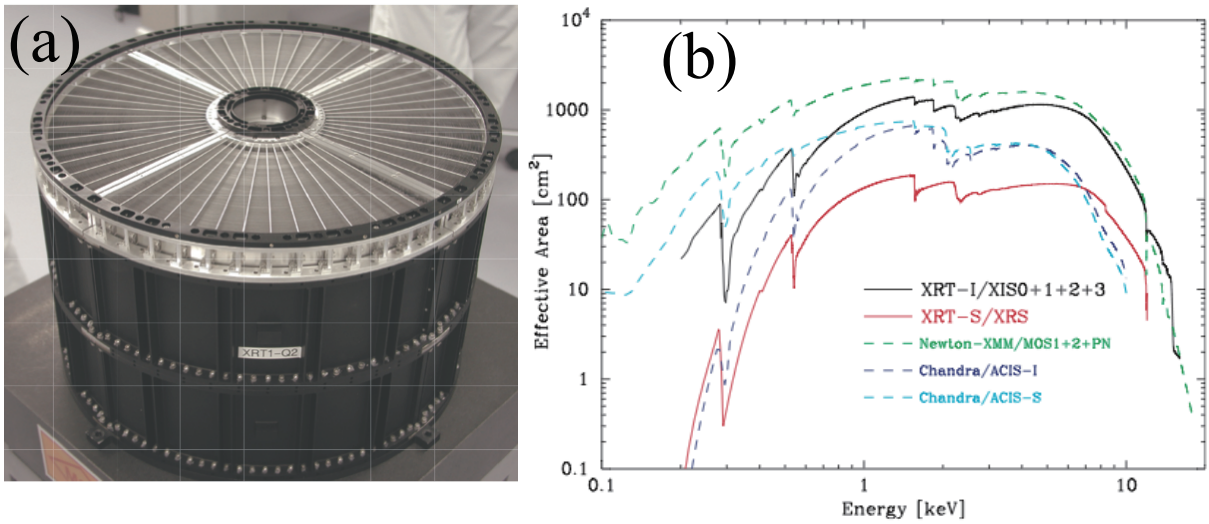

Figure 3.2: A photograph of the XRT-I1 (a) and effective areas of the XRT units (b). These figures are taken from Serlemitsos et al. (2007).

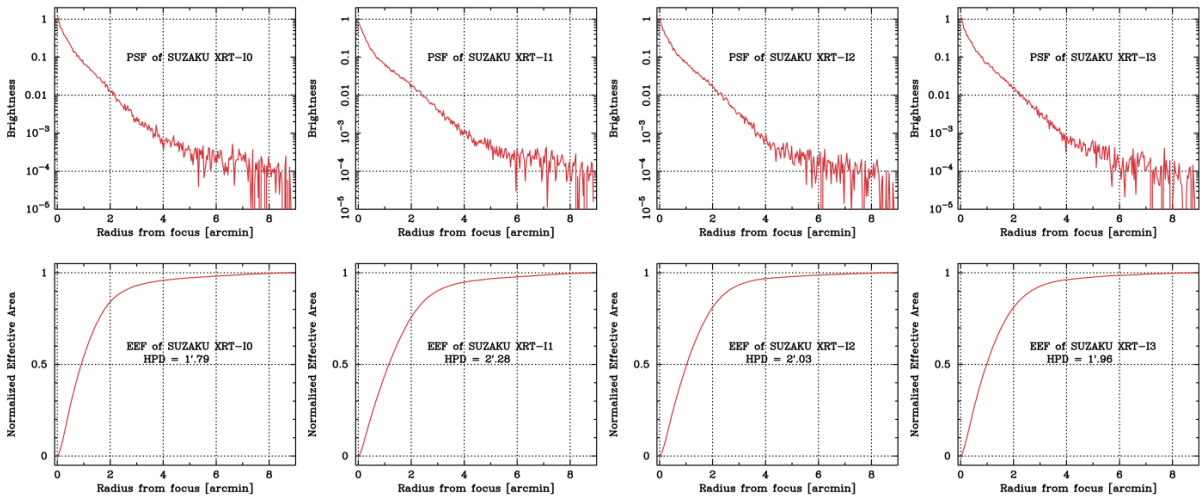

Figure 3.3: Point Spread Functions (upper panels) and Encircled Energy Functions (lower panels) of XRT-I. Left and right panels are of XRT-I2 and XRT-I3, respectively. The figure is taken from Serlemitsos et al. (2007).

3.3 X-ray Imaging Spectrometer

The X-ray Imaging Spectrometer (XIS; Koyama et al. 2007) is composed of four cameras, which are dedicated to perform imaging and spectroscopy of X-rays in the soft energy band of $0.2 - 12$ keV, with the help of XRT-I. Basic parameters of the XIS are listed in table 3.1. The XIS camera (one among the four) is shown in figure 3.4, in which the main sensor is an X-ray sensitive silicon charge-coupled device (CCD). They are operated in a photon-counting mode like *ASCA*/SIS.

The four sensors are labeled as XIS0, XIS1, XIS2, and XIS3. Among them, XIS0, XIS2 and XIS3 are front-illuminated (FI) CCDs, while XIS1 is a back-illuminated (BI) CCD. The former three have lower quantum efficiency in $\lesssim 4$ keV than the latter, because the front side of the CCD has a gate structure composed of thin Si and SiO_2 layers, and a certain fraction of incoming X-rays are lost by photo-electric absorption. Since a BI CCD has relatively thin depletion layer, its quantum efficiency above ~ 4 keV is lower than that of FI CCD, in turn.

In order to accommodate demands for various source fluxes. the XIS offers several observation options: window mode and burst clock mode. When the XIS is operated without specifying these, all the pixels (1024×1024) are read out every 8 seconds. There are three window mode called normal (full), 1/4, and 1/8, which literally specifies the size of the image. For instance, when operated with 1/4 window option, the XIS reads out only 256×1024 pixels every 2s. Thus, the 1/4 or 1/8 window modes confine the image, but improves the time resolution, which is usually suitable for point sources. The other option, the burst clock mode, specifies a snap time (data-taking live time) of the XIS, which can prevent the CCD from piling up when the observation target is very bright. The 1/4 window mode with 1.0 s burst clock option means that 1-s image is taken every 2 s, and photons of the remaining 1 s are abandoned.

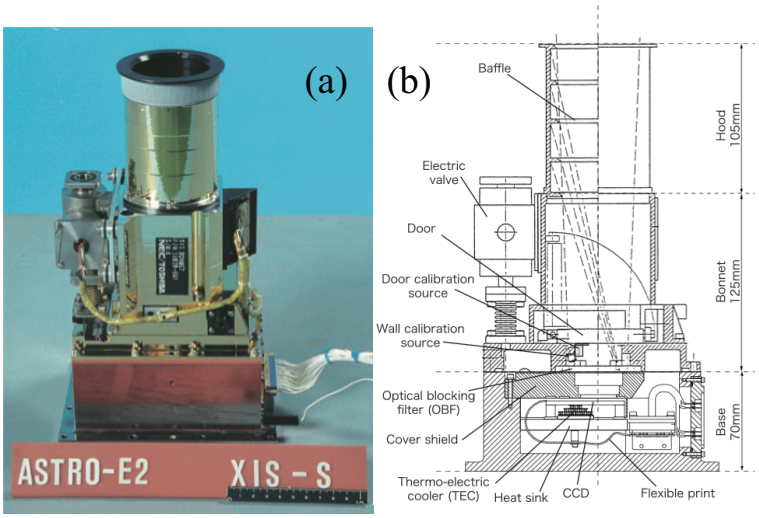

Figure 3.4: A picture of an XIS sensor (a) and its cross-section (b), taken from Koyama et al. (2007).

Table 3.1: Basic properties of the XIS.

Field of view	$18' \times 18'$	
Energy range	$0.2 - 12$ keV	
Format	1024×1024	
Pixel size	24μm $\times 24\mu$m	
Energy resolution[a]	~ 130 eV	
Effective area	(FI)	(BI)
1.5 keV	330 cm^2	370 cm^2
8 keV	160 cm^2	110 cm^2
Time resolution	8 s (full window)	

[a]In FWHM at 5.9 keV.

3.4 Hard X-ray Detector

The Hard X-ray Detector (HXD; Takahashi et al. 2007) is a scintillating instrument developed jointly by the University of Tokyo, ISAS/JAXA, and many other institutes. The parameters of the HXD are listed in table 3.2. It is aimed at hard X-ray observations from $\sim$ 10 keV to $\sim$ 600 keV, and hence plays a leading role in our study of hard-state LMXBs. As shown in figure 3.5, the HXD has a rectangular shape consist of 4×4 so-called "well"-counter units surrounded by 20 BGO active shields.

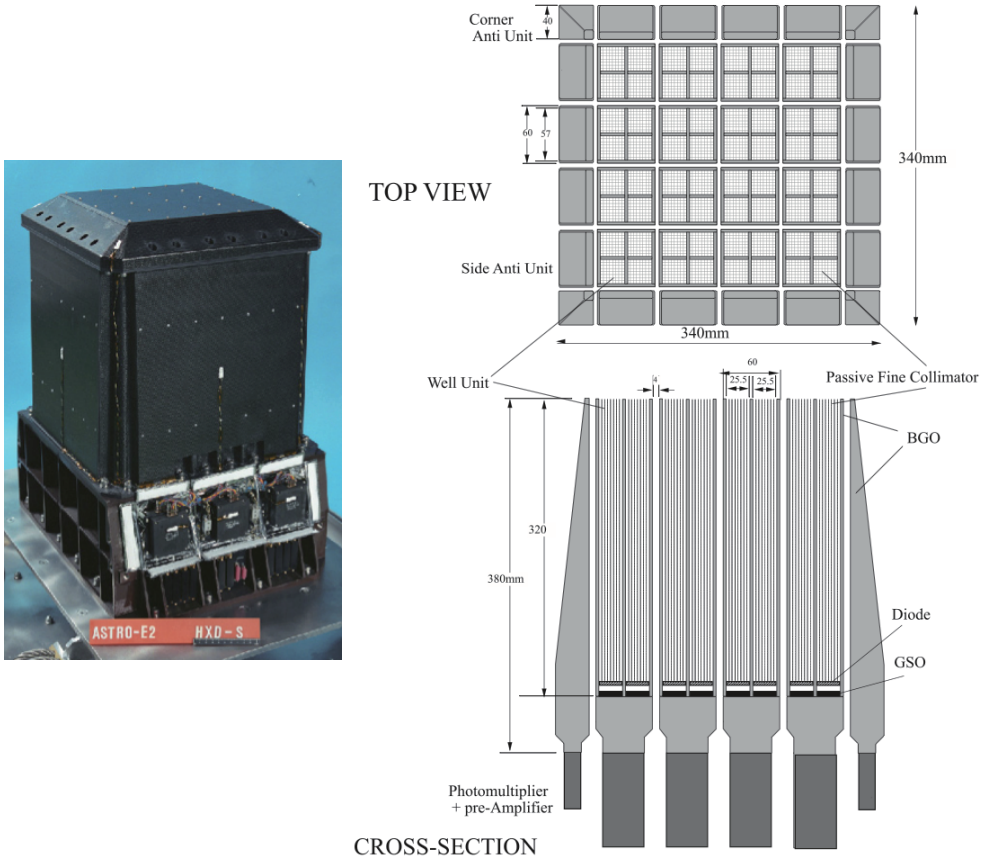

Figure 3.5: A photograph of the HXD (left) and a schematic view of HXD-S (right), both taken from Takahashi et al. (2007).

Table 3.2: Basic parameters of the HXD.

Field of view ($\gtrsim$ 100 keV)	$4.5^\circ \times 4.5^\circ$
Field of view ($\lesssim$ 100 keV)	$34' \times 34'$
Energy range	$10 - 600$ keV
-PIN	$10 - 70$ keV
-GSO	$40 - 600$ keV
Energy resolution	
-PIN	~ 3 keV (FWHM)
-GSO	$7.6/\sqrt{E_{\rm MeV}}\%$ (FWHM)
Effective area	
- 20 keV	~ 160 cm^2
- 100 keV	~ 260 cm^2
Time resolution	61 μs

As shown in figure 3.6, a well-counter unit is composed of 4 Si-PIN diode assemblies PIN diode assembly, GSO scintillators, and BGO crystals glued to form the well-like shape. The latter two scintillators are read out by single photo-multiplier tube, namely, used in a phoswich configuration. Since the decaying times of the scintillation between the two are different, by sampling pulse heights (PHs) with two different shaping times, we can determine from which scintillator the signal came. Figure 3.7 (left) shows a fast-slow diagram, where PH with fast (time constant of 150 ns) shaper is plotted against that with slow (1 μs) shaper. The data points are split into two lines, reflecting the decaying time of BGO and GSO. Since the decaying time of GSO, $\sim$ 122 ns at a temperature of -20°C, is shorter than that of BGO ($\sim$ 706 ns), signals from GSO can be identified as those with lower slow-to-fast ratio (i.e. milder slope in the diagram). As shown in figure 3.7 (right), the signals of GSO are successfully extracted by this pulse shape discrimination (PSD). Thus, background signals which mostly arises from charged particles in the orbit can be significantly reduced by PSD, because the particles should penetrate BGO and exhibit higher slow-to-fast ratio. The 4 PIN diodes, each made of 2 mm thick Si, are read out via 4 independent analog chains. They share trigger timings with the GSO/BGO phoswich. Thus the BGO signals can be latched and used for anti-coincidence screening for PIN events, as well. In-orbit performance of the HXD is shown in (Kokubun et al. 2007), in detail.

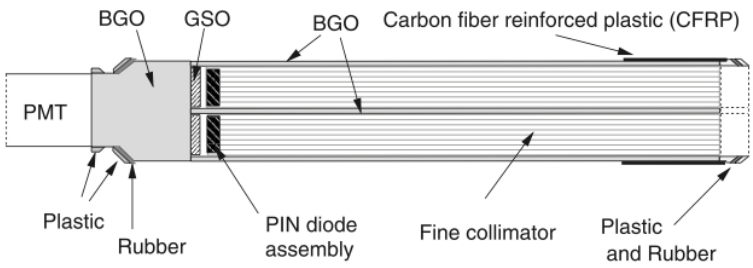

Figure 3.6: A detailed schematic drawing of a well-counter unit in the HXD.

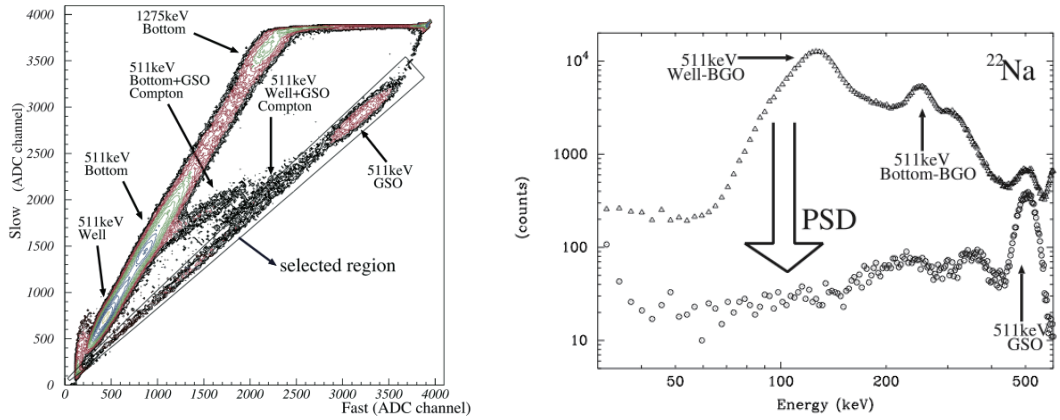

Figure 3.7: A fast-slow diagram of a well-counter unit for the ^{22}Na irradiation (left) and corresponding spectra with/without the PSD selection (right).

Chapter 4

OBSERVATION

4.1 Source Selection

4.1.1 Strategy

As described in Chapter 2, many of the past LMXB studies have been focused on their classification by e.g. CCD. In other words, the true goal of understanding their physics were often replaced by more superficial attempts of empirical characterization. As a result, there has been little progress in establishing physical understanding of these systems and the involved phenomena, including the accretion geometry, X-ray emission mechanism, and the overall energetics.

When we regard an LMXB as one system, we may roughly describe its physical condition with some small number of characteristic quantities, including the NS mass $M_{\rm NS}$, the NS radius $R_{\rm NS}$, the NS magnetic field $\vec{B}$, the mass accretion rate $\dot{M}$, its hysteresis $M_{\rm h} \equiv \int_{-\infty}^{t} dt' \dot{M}(t-t')h(t')$ where $h(t)$ is a certain response function, the system inclination i, and the abundance $\mathbf{A}$ of the accreting matters. Among them, $M_{\rm NS} \sim 1.4 M_{\odot}$ and $R_{\rm NS} \sim 10$ km are considered to be rather well determined, and $\vec{B}$ is considered to play a minor role in LMXBs. As a result, their intrinsic behavior must be principally determined by $\dot{M}$ and possibly by $M_{\rm h}$ as well, and their observed (apparent) behavior is further affected by i. While $M_{\rm h}$ and i are relatively difficult to estimate, $\dot{M}$ can be directly related to the luminosity $L_{\rm x}$ as

$$L_{\rm x} = \eta \frac{G M_{\rm NS} \dot{M}}{R_{\rm NS}} \tag{4.1}$$

where η is the efficiency of conversion from gravitational to radiative energies ($0 < \eta < 1$); we assume $\eta \sim 1$, considering the non-radiative energy losses (e.g. in outflows) are negligible. This $L_{\rm x}$, in turn, can be estimated from the observed (band-limited) X-ray

flux $f_{\rm X}$ using the source distance. Here, major uncertainties affecting $L_{\rm x}$ are those in the distance estimates, in i, and the bolometric correction.

In the present study, we analyze broad-band spectra of a sufficient number of LMXBs employing quantitative emission models, and examine the derived results mainly as a function of $\dot{M}$, or $L_{\rm x}$. If we find any scatter among LMXBs with nearly the same $\dot{M}$, then effects of i, $M_{\rm h}$, or $\mathbf{A}$ should be considered as subsidiary parameters. Since the soft state of these objects has been well understood by previous studies, we mainly focus on the hard state which is realized when $\dot{M}$ is relatively low and the spectra extend from ~ 1 keV to over ~ 100 keV (§2.1.2).

4.1.2 *Suzaku* data sets

Table 4.1 shows all LMXBs so far observed by *Suzaku*. In order to reduce the freedom of $\vec{B}$ and $\mathbf{A}$, we exclude some particular sources such as those with high B like 4U1822-37 (Sasano et al. 2014), and a subgroup called Ultra Compact X-ray Binaries (UCXB) which have white dwarfs as the donor component, and hence the accreting matter is devoid of hydrogen. The number of observations of transient sources such as 4U1608-52 are clearly larger than that of persistent sources like GX* sources. Among them, the observation of 4U1812-12 observation (406008010) is based on our own proposal in the *Suzaku* Announcement Opportunity 6 (AO6), while the rest is from the archive. Thus, our data sample consists of 43 observations of 16 sources.

To characterize all the data sets to be utilized, we plotted them in figure 4.1, where abscissa is absorbed $0.8-60$ keV luminosity, $L_{\rm abs}$, while ordinate is a ratio H between a hard-band count rate to that in a soft band. To avoid effects of interstellar absorption on H, we selected the soft band as $5-10$ keV XIS-FI count rates, and the hard band as $20-40$ keV HXD-PIN rates, both with the background subtracted as described in §4.2. The luminosity $L_{\rm abs}$ was calculated as a sum of the background-subtracted $0.8-10$ keV flux with XIS-FI and that in $12-60$ keV from HXD-PIN, multiplied by $4\pi D^2$ where D is the distance given in table 4.1. The quoted errors take into account distance uncertainties if available. Although we should in principle use absorption-corrected luminosity rather than $L_{\rm abs}$, we have chosen to use the latter, because the correction for absorption would require an accurate spectral fitting (to be described in Chapter 5). In the two observations of Aql X-1 (402053060 and 402053070) and that of Cen X-4 (403057010), the source was too dim to detect significantly with the HXD. We therefore extrapolated their $L_{\rm abs}$ and H with best-fit models described later in Chapter 5.

The simple two-dimensional information in figure 4.1 already gives us some clues to our data sample. When $L_{\rm abs} \gtrsim 10^{37}$ erg s^{-1} , our data sets mostly lie in a region of low hardness as $H \lesssim 0.03$. On the contrary, those with $L_{\rm abs} \lesssim 10^{37}$ erg s^{-1} all have

$H \gtrsim 0.04$. This is considered to represent the known bimodality $--$ the soft state at high $L_{\rm abs}$, and the hard state at low $L_{\rm abs}$ (§2.1.2). In other words, our sample covers both states.

In the present thesis, we define that a source is in the soft state if $H < 0.03$, and in the hard state if $H > 0.03$. According to this definition, the soft-state and hard-state observations are colored in figure 4.1 black and red, respectively. In terms of luminosity, the two states thus overlap at $5 \times 10^{36} < L_{\rm abs} < 4 \times 10^{37}$ erg s^{-1} , or $0.03 - 0.2 L_{\rm edd}$, but the classification becomes clearcut when employing H. The classification of soft/hard states is given in table 4.1. Surprisingly, there is a particular observation of Aql X-1 (406010020) within which the source seems to have made a hard-to-soft state transition, indicated as a dotted arrow in figure 4.1. Detailed observation properties of the hard state (including the soft-state Aql X-1: 402053010) are shown in table 4.2.

Table 4.1: *Suzaku* observations of LMXBs utilized in the present thesis.

Name	tag	OBSID	Date	E^a	$L^b_{\rm abs}$	$L_{\rm abs}/L_{\rm edd}$	H	State	D (kpc)	Ref.[c]
4U 1608-52		404044010	2010/03/11	28.0	1.4E+37	0.08	$(4.65 \pm 0.04) \times 10^{-3}$	soft	3.6	1
		404044020	2010/03/15	25.2	7.7E+36	0.04	$(5.38 \pm 0.07) \times 10^{-3}$	soft		
		404044030	2010/03/18	14.2	3.3E+36	0.02	$(3.97 \pm 0.04) \times 10^{-2}$	hard		
		404044040	2010/03/22	14.5	1.0E+36	0.006	$(5.19 \pm 0.09) \times 10^{-2}$	hard		
4U 1636-536		401050010	2007/02/09	20.3	6.5E+36	0.04	$(5.18 \pm 0.05) \times 10^{-2}$	hard	5.9	2
		401050020	2007/02/22	33.2	1.1E+37	0.07	$(5.85 \pm 0.08) \times 10^{-3}$	soft		
		401050030	2007/03/01	45.2	8.7E+36	0.05	$(1.64 \pm 0.01) \times 10^{-2}$	soft		
		401050040	2007/03/27	26.1	8.5E+36	0.05	$(6.6 \pm 0.1) \times 10^{-3}$	soft		
		401050050	2007/03/29	11.0	8.6E+36	0.05	$(5.0 \pm 0.1) \times 10^{-3}$	soft		
4U 1705-44		401046010	2006/08/29	14.4	8.1E+36	0.05	$(4.59 \pm 0.05) \times 10^{-2}$	hard	$7.4^{+0.8}_{-1.1}$	3
		401046020	2006/09/18	14.7	1.7E+37	0.1	$(2.46 \pm 0.06) \times 10^{-3}$	soft		
		401046030	2006/10/06	16.7	6.7E+36	0.04	$(2.14 \pm 0.08) \times 10^{-3}$	soft		
		402051010	2007/09/05	8.8	5.7E+37	0.3	$(3.48 \pm 0.06) \times 10^{-3}$	soft		
		402051020	2007/10/08	14.8	3.7E+37	0.2	$(3.44 \pm 0.06) \times 10^{-3}$	soft		
		402051030	2008/02/20	19.5	1.5E+37	0.09	$(4.16 \pm 0.09) \times 10^{-3}$	soft		
		402051040	2008/03/18	12.4	4.0E+37	0.2	$(3.60 \pm 0.06) \times 10^{-3}$	soft		
		406076010	2012/03/27	84.5	4.6E+36	0.03	$(6.10 \pm 0.04) \times 10^{-2}$	hard		
4U 1728-34		405048010	2010/10/04	88.3	5.9E+36	0.03	$(1.77 \pm 0.01) \times 10^{-2}$	soft	5.2	4
4U 1812-12		406008010	2011/10/04	49.9	1.4E+36	0.008	$(1.208 \pm 0.009) \times 10^{-1}$	hard	4	5
Aql X-1	D1	402053010	2007/09/28	12.5	9.6E+36	0.06	$(2.06 \pm 0.08) \times 10^{-3}$	soft	5.2 ± 0.7	6
	D2	402053020	2007/10/03	11.2	1.9E+36	0.01	$(7.2 \pm 0.1) \times 10^{-2}$	hard		
	D3	402053030	2007/10/09	16.1	2.3E+36	0.01	$(6.6 \pm 0.1) \times 10^{-2}$	hard		
	D4	402053040	2007/10/15	16.3	1.8E+36	0.01	$(7.1 \pm 0.1) \times 10^{-2}$	hard		
	D5	402053050	2007/10/19	15.9	3.5E+35	0.002	$(7.1 \pm 0.3) \times 10^{-2}$	hard		
	D6	402053060	2007/10/24	19.8	9.1E+33	5e-5	$(6 \pm 2) \times 10^{-2}$	hard		
	D7	402053070	2007/10/30	13.4	1.1E+34	6e-5	$(1.2 \pm 0.3) \times 10^{-1}$	hard		
	R1	406010010	2011/10/18	32.8	1.0E+37	0.06	$(6.89 \pm 0.03) \times 10^{-2}$	hard		
	R2	406010020	2011/10/21	35.2	(2.7-3.7)E+37	0.2	$0.12 - 0.008$	trans.		
	R3	406010030	2011/10/24	34.0	4.7E+37	0.3	$(3.08 \pm 0.02) \times 10^{-3}$	soft		

Name	tag	OBSID	Date	E^a	$L^b_{\rm abs}$	$L_{\rm abs}/L_{\rm edd}$	H	State	D (kpc)	Ref.^{c}
Cen X-4		403057010	2009/01/16	124.0	5.1E+31	3e-7	$(9 \pm 3) \times 10^{-2}$	hard	1.2 ± 0.3	7
Cyg X-2		401049010	2006/05/16	34.5	5.7E+37	0.3	$(2.15 \pm 0.02) \times 10^{-3}$	soft	7.2	8
		403063010	2008/07/01	81.9	5.9E+37	0.3	$(6.50 \pm 0.04) \times 10^{-3}$	soft		
GS 1826-238		404007010	2009/10/21	82.0	1.1E+37	0.06	$(1.038 \pm 0.004) \times 10^{-1}$	hard	7^{+1}_{-3}	9
GX 17+2		402050010	2007/09/19	15.0	1.5E+38	0.9	$(6.23 \pm 0.05) \times 10^{-3}$	soft	9.8	10
		402050020	2007/09/27	17.7	7.2E+37	0.4	$(1.92 \pm 0.01) \times 10^{-2}$	soft		
		406070010	2011/10/19	81.1	1.8E+38	1.0	$(6.28 \pm 0.02) \times 10^{-3}$	soft		
GX 340+0		403060010	2009/03/02	80.3	8.5E+37	0.5	$(9.05 \pm 0.04) \times 10^{-3}$	soft	11 ± 3	11
GX 349+2		400003010	2006/03/14	18.7	4.5E+37	0.3	$(3.82 \pm 0.03) \times 10^{-3}$	soft	5	12
		400003020	2006/03/19	23.9	1.9E+37	0.1	$(2.94 \pm 0.02) \times 10^{-2}$	soft		
GX 9+9		404071010	2010/03/16	57.6	7.6E+37	0.4	$(4.57 \pm 0.04) \times 10^{-3}$	soft	10	13
LMC X-2		401012010	2006/04/24	69.0	1.5E+38	0.9	$(1.01 \pm 0.05) \times 10^{-3}$	soft	50	14
Ser X-1		401048010	2009/03/11	15.3	4.8E+37	0.3	$(2.82 \pm 0.03) \times 10^{-3}$	soft	8.4	12
SLX 1737-282		503103010	2006/10/24	29.0	3.5E+35	0.003	$(8.2 \pm 0.4) \times 10^{-2}$	hard	$5 - 8$	15

[a]Net exposure in ks per XIS sensor.

[b]Absorbed $0.8 - 60$ keV luminosity in erg s^{-1}

[c]References from which D is quoted.

[1]Nakamura et al. (1989), [2]Cornelisse et al. (2003), [3]Haberl & Titarchuk (1995) [4]Galloway et al. (2003), [5]Cocchi et al. (2000), [6]Jonker & Nelemans (2004) [7]Chevalier et al. (1989), [8]Orosz & Kuulkers (1999), [9]Barret et al. (2000) [10]Kuulkers et al. (2002), [11]Fender & Hendry (2000), [12]Christian & Swank (1997) [13]Savolainen et al. (2009), [14]Feast (1999), [15]in 't Zand et al. (2002)

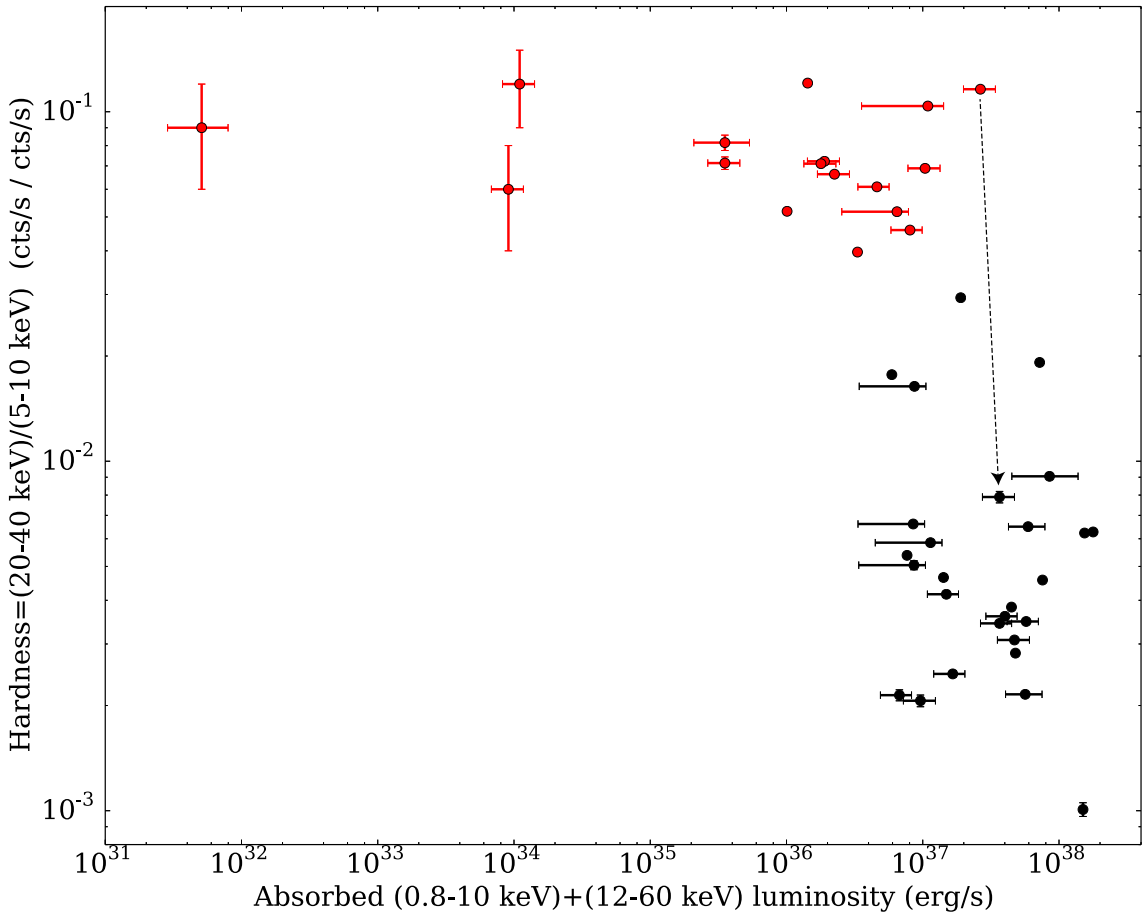

Figure 4.1: The hardness versus absorbed $0.8 - 60$ keV source luminosity of the observations in table 4.1. See text for the definition of the hardness. Black and red denote the soft and hard states, respectively, as defined in the present thesis.

Table 4.2: The XIS operation mode and the source intensity of the present *Suzaku* observations in the hard state.

Name	OBSID	Nom.[a]	Win.[b]	Clock[c]	Snap[d]	Rate[e]
4U1608-52	404044030	HXD	1/4	burst	0.5	55.4
	404044040	HXD	1/4	burst	0.993	17.4
4U1636-536	401050010	XIS	1/4	burst	0.993	46.2
4U1705-44	401046010	XIS	1/4	burst	1.6	17.7
	406076010	XIS	1/4	normal	2	11.1
4U1812-12	406008010	XIS	1/4	normal	2	11.2
AqlX-1	402053010	XIS	1/4	burst	0.5	159
	402053020	XIS	1/4	normal	2	15.2
	402053030	XIS	1/4	normal	2	17.8
	402053040	XIS	1/4	normal	2	13.7
	402053050	XIS	1/4	normal	2	3.1
	402053060	XIS	1/4	normal	2	0.19
	402053070	XIS	1/4	normal	2	0.16
	406010010	XIS	1/4	burst	0.5	59.9
	406010020	XIS	1/4	burst	0.5	257
CenX-4	403057010	XIS	full	normal	8	0.26
GS1826-238	404007010	HXD	1/4	normal	2	23.2
SLX1737-282	503103010	XIS	full	normal	8	1.8

[a]Nominal pointing position (XIS or HXD).
[b]XIS window mode (full, 1/4, or 1/8).
[c]XIS clock mode.
[d]XIS snap time (data-taking live time) in second.
[e]XIS0 count rate (Hz) in whole energy band and full region.

4.2 Data Reduction

In order to obtain light curves and spectra of the sources listed in §4.1.2, we processed the data with HEASoft[a] (version 6.16) in the following manner.

4.2.1 XIS data processing

Among the three available XIS sensors, the present thesis utilizes FI ones, namely XIS0 and XIS3, by summing up them. We selected their events of which the GRADE was either 0, 2, 3, 4, or 6, and set time intervals after exits from the South Atlantic Anomaly (SAA) to be longer than 436 s. If not specified individually in or after §4.3, we extracted on-source events from a $2'$ circle region, larger by a factor of > 2 than the HPD of the XRT (§3.2), and background events from an annulus with inner radius of $4'$ and outer radius of $5'$. The latter includes both the NXB (§3.3) and Cosmic X-ray Background (CXB).

Those observations which caught bright periods of the objects, such as that of Aql X-1 (402053010), may be affected by pile-up effects (Yamada et al. 2012). In such cases, we need to discard a core region of the source image in order to recover a correct spectrum. For instance, if an observation operated in a 1/4 window mode without any burst clock option has an XIS-0 count rate of ~ 90 cts s^{-1}, a circular region within $\sim 40''$ is piled up by 3%, as Yamada et al. (2012) estimated for 4U1705-44 (401046020). Comparing the XIS count rates and the snap times (data-taking live times) with those in Yamada et al. (2012), observations with mean snap counts (rate$\times$ snap time) larger than $\gtrsim 45$ are likely to need corrections. Among our data sets listed in table 4.2, those of Aql X-1 (Obs-D1 and Obs-R2) and GS1826-238 (404007010) applies. The correction details for these sources are stated individually in §4.3 and §4.4.6.

In Chapter 5, we analyze XIS spectra mostly in $0.8 - 10$ keV energy ranges. In order to avoid the instrumental effect, we exclude 1.7-1.9 keV and 2.2-2.4 keV ranges, corresponding to silicon K-edge and gold M-edge, respectively. This is due to the large calibration uncertainties around these energy bands.

4.2.2 HXD data processing

We screened the HXD data for all observations using the following common criteria; the time intervals after exits from the SAA should be longer than 500 s; the target elevation above the earth limb should be > 5 deg; and the geomagnetic cutoff rigidity at the spacecraft location should be higher than 8 GV. The NXB spectra and NXB light

[a] http://heasarc.nasa.gov/lheasoft/

curves were synthesized, considering actual observing conditions of each data set, from a huge reservoir of NXB events which were accumulated while the HXD was pointing to the night Earth (Fukazawa et al. 2009). We simulated the CXB spectra by assuming the emission model as

$$\mathrm{CXB}(E) = 9.4 \times 10^{-3} \left(\frac{E}{1\ \mathrm{keV}} \right)^{-1.29} \exp\left(-\frac{E}{4\ \mathrm{keV}} \right) \quad \text{photons s}^{-1}\text{cm}^{-2}\text{keV}^{-1}\text{FOV}^{-1} \tag{4.2}$$

from Boldt (1987), and subtracted from the source spectra as well.

In the spectral analysis in Chapter 5, we simultaneously fit the XIS and HXD spectra with a common model. Namely, the model is convolved with the XIS and HXD responses (§3.3 and §3.4), to be compared with the actual XIS and HXD spectra, respectively. The cross normalization between the XIS and HXD, in reality deviates slightly from the nominal value of 1.00. It has been calibrated with the Crab Nebula data obtained on many occasions (Ishida 2006, 2007; Maeda 2008); the model prediction for the HXD should be multiplied by a factor of 1.09 and 1.14, if the source is placed at the "XIS nominal" and "HXD nominal" pointing positions, respectively. We use these canonical values for our spectral analyses in Chapter 5. Unless explicitly stated in §4.3 and later, we produce spectra for XIS and HXD by integrating whole exposure time. If type-1 bursts are present, ~ 300 s before and after the peaks are discarded.

4.3 Aql X-1

As a typical recurrent-transient LMXB, Aql X-1 is located at a distance of 5.2 ± 0.7 kpc (Jonker & Nelemans 2004), and forms a 18.95-hour binary together with an optical companion of which the magnitude in X-ray quiescence is $V = 21.6$ in X-ray quiescence (Chevalier et al. 1999). The object exhibits outbursts quasi-periodically in every $200-300$ days (Kitamoto et al. 1993; Simon 2002) with their typical duration of ~ 1 month. It is also known to produce type-1 X-ray bursts (Koyama et al. 1981; Czerny et al. 1987). During its type-1 bursts, nearly coherent oscillations were found by Zhang et al. (1998) at 549 Hz. The pulsation was reconfirmed by Casella et al. (2008), during a very short (150 s) portion of persistent emission in the past ~ 10 years, and is considered to represent the NS spin.

Among the hard-state observations listed in table 4.1, those of Aql X-1 obviously dominate in number, and cover a wide range of luminosity across four orders of magnitude. These data sets hence allow us to study purely the effects of $\dot{M}$ (and possibly $M_{\rm h}$). Therefore, among the hard-state sources, we selected this Aql X-1 as a "first bite" of our research (Sakurai et al. 2012, 2014).

4.3.1 Outburst in 2007: decaying phase

As presented in figure 4.2, Aql X-1 exhibited an outburst in 2007, starting from the beginning of September and lasting to the end of October. The source was observed by *Suzaku* for seven times at the decaying phase of the outburst, with a typical exposure of $10 - 20$ ks each. These observations are indicated with arrows in the figure. The luminosity varied from $\sim 10^{37}$ erg s^{-1} down to $\sim 10^{34}$ erg s^{-1} in these observations. For convenience, as written in table 4.1, we label the seven observations as " Obs-D#".

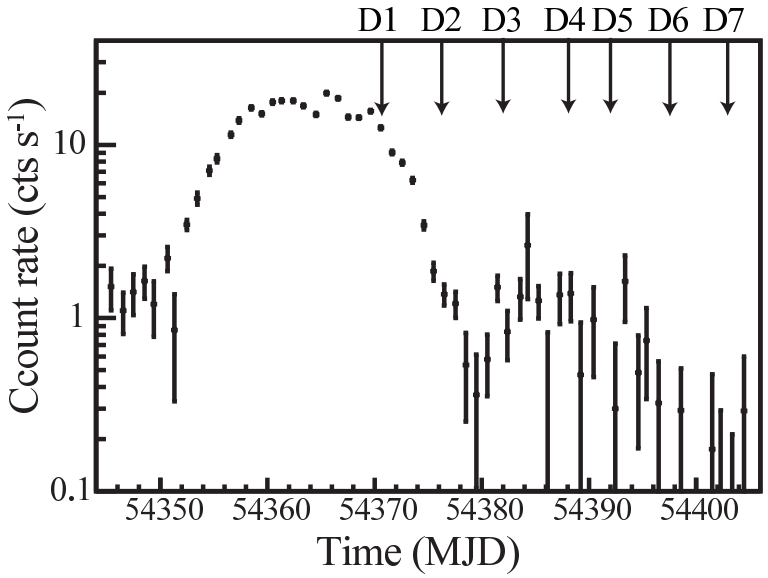

Figure 4.2: A $2-12$ keV long-term light curve of Aql X-1 around the outburst in 2007, obtained with the *RXTE* /ASM. The binning time is 1 day. Arrows indicate the epoch of the 7 *Suzaku* observations.

All the seven observations were operated with 1/4 window mode. The burst clock option with 0.5 s was employed in Obs-D1 because the expected count rate was high, while the others were done with the normal option. Among the seven, thus we should be careful of the pile-up effects (§4.2.1) on Obs-D1. As Yamada et al. (2012) examined, the effect can be seen in Obs-D1 by 3% within 16" circular region or 1% within 50". Therefore, we discarded a central 30" region from the on-source region for Obs-D1 to create its spectra and light curves.

Figure 4.3 shows background-subtracted light curves of the seven observations, namely Obs-D1 to Obs-D7. Burst-like events were found in none of them. In Obs-D2, Obs-D5, and Obs-D6, the source gradually faded by $\lesssim 5\%$ per 10 ks, while in the others it was nearly constant within statistical errors. Even in the former cases, the hardness, which is here defined as the count-rate ratio (12-60 keV)/(0.8-10 keV), are essentially constant within errors.

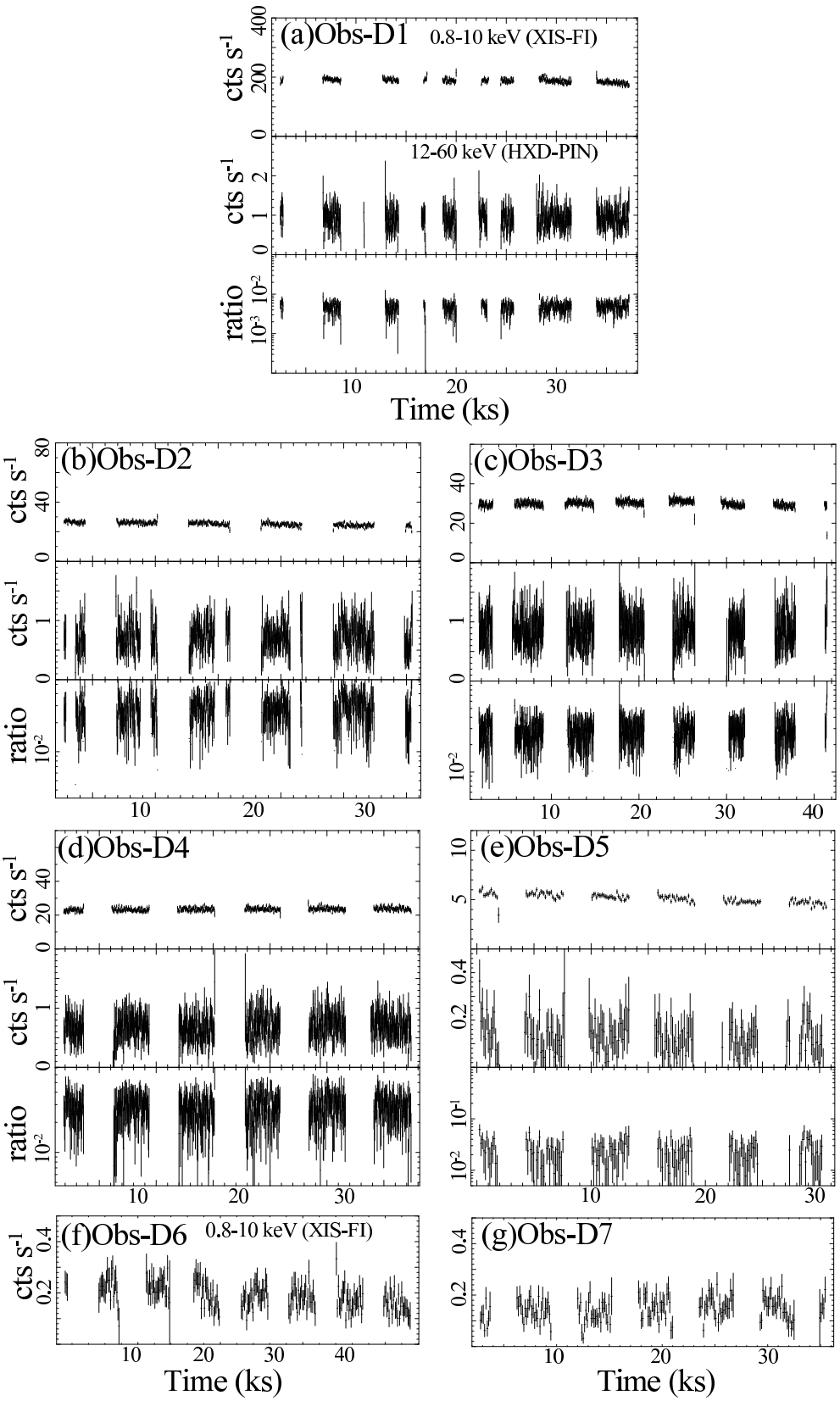

Figure 4.3: Short-term light curves of Aql X-1 in the hard state in 2007 (Obs-D1 - Obs-D7). Panels (a), (b), (c), (d) and (e) shows XIS-FI ($0.8-10$ keV) count rates at the top, HXD-PIN ($12-60$ keV) rates at the middle, and their ratio (PIN/XIS) at the botom. Panels (f) and (g) show only the XIS data, since the object was undetectable with the HXD. The binning times are 32 s for (a)-(d) and 128 s for (e)-(g). Panel (a) is corrected for pile-up as described in text.

4.3.2 Outburst in 2011: rising phase

In 2011 October, *Suzaku* was able to observe another outburst of Aql X-1 in three pointings separated by 3 days (table 4.1). Fortunately, the observations caught the source in a rising phase, contrary to those in 2007 made in a decaying phase. These data sets hence allow us to study the hysteresis effects, $M_{\rm h}$. Figure 4.2 shows a long-term light curve of Aql X-1 on this occasion, as observed with MAXI (Monitor of All-sky X-ray Image) which started its operation since 2009 August. The three observations indicated with arrows were conducted in almost midst of the rising slope. In the same manner as §4.3.2, we label these observations as " Obs-R#".

In all the three observations, the XIS were operated with 1/4 window mode using the XIS-nominal position, employing the burst clock option with 0.5 s. Since the source was very luminous ($L_{\rm abs} > 10^{37}$ erg s^{-1} ; table 4.1), we should be careful about the pile-up effects (§4.2.1). Over a 2′-radius region around the image centroid, the raw 0.8-10 keV count rates per XIS camera was $\sim$ 60 cts s^{-1} , $\sim$ 300 cts s^{-1} , and $\sim$ 500 cts s^{-1} , in Obs-R1, Obs-R2, and Obs-R3, respectively. Estimating from several results in Yamada et al. (2012), the effects on the latter two can be significant, though that on Obs-R1 is negligible as $< 3\%$. The radius within which a fraction of 3% is piled-up is $\sim 40''$ for Obs-R2 and $\sim 50''$ for Obs-R3. We hence discarded the central 1′-radius region in the latter two observations, and took larger 2.5′-radius on-source region to compensate for the statistical loss.

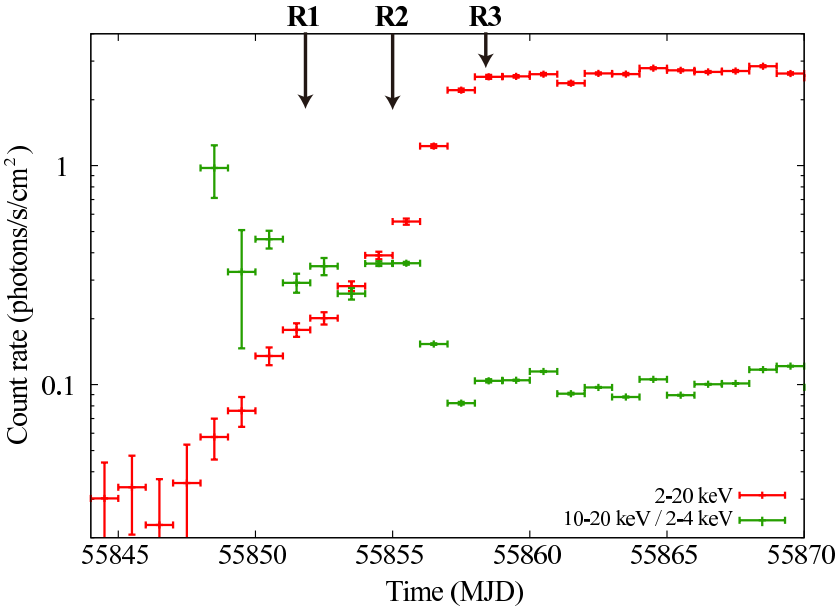

Figure 4.4: A long-term light curve of Aql X-1 around the outburst beginning in 2011, obtained with the *MAXI* /GSC. The red and green points are 2–20 keV rates and the hardness ratio (10–20 keV)/(2–4 keV), respectively.

The first observation Obs-R1 was in the hard state, but the observed $L_{\rm abs} = 1.0 \times 10^{37}$ erg s^{-1} was higher by 1 order of magnitude than that of Obs-D3. The source light curve is shown in figure 4.5. The XIS count rate and that of HXD-PIN are almost constant within 20%, so is their ratio in the bottom panel. One type-1 burst occurred at 11.4 ks after the beginning of the observation, and some may be hidden in the earth occultation periods.

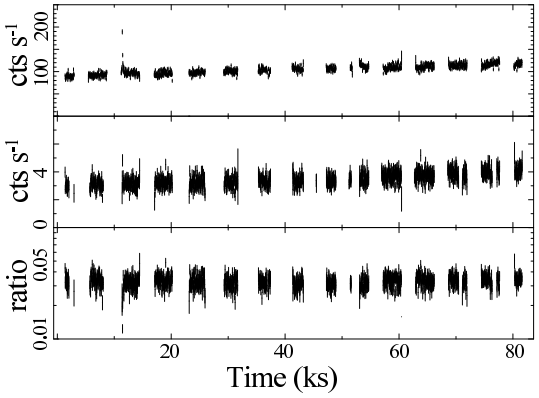

Figure 4.5: Light curves of AqlX-1 in the hard state (Obs-R1). The panel configuration is the same as figure 4.3.

As seen in figure 4.6, the second observation Obs-R2 recorded a factor ~ 2.5 increase in the XIS count rate on 80 ks, and an associated (anti-correlated) decrease by a factor of ~ 2.5 in the HXD-PIN rate. This suggests that this observation successfully captured a hard-to-soft state transition. As mentioned in §4.1.2 and given in table 4.1, $L_{\rm abs}$ changed from 2.7×10^{37} erg s^{-1} to 3.7×10^{37} erg s^{-1} , by a factor of ~ 2, and the latter is more than twice higher than that of the soft state in 2007 (Obs-D1). This is considered to represent a hysteresis effect. For following spectral analysis in Chapter 5, we divided the exposure time into ten intervals P$_i$ ($i = 0...9$) as indicated in figure 4.6.

We should also pay attention to type-1 bursts seen in figure 4.6. It recurred almost every ~ 5 ks from the beginning, probably due to high $\dot{M}$. However, it ceased after the middle of the transition. This behavior agrees with a general understanding that the accreted material undergoes steady nuclear burning when $\dot{M}$ is high. (e.g. Cornelisse et al. 2003; Cumming 2004; Galloway et al. 2008). Like in Obs-R1, we exclude these bursts from on-source intervals.

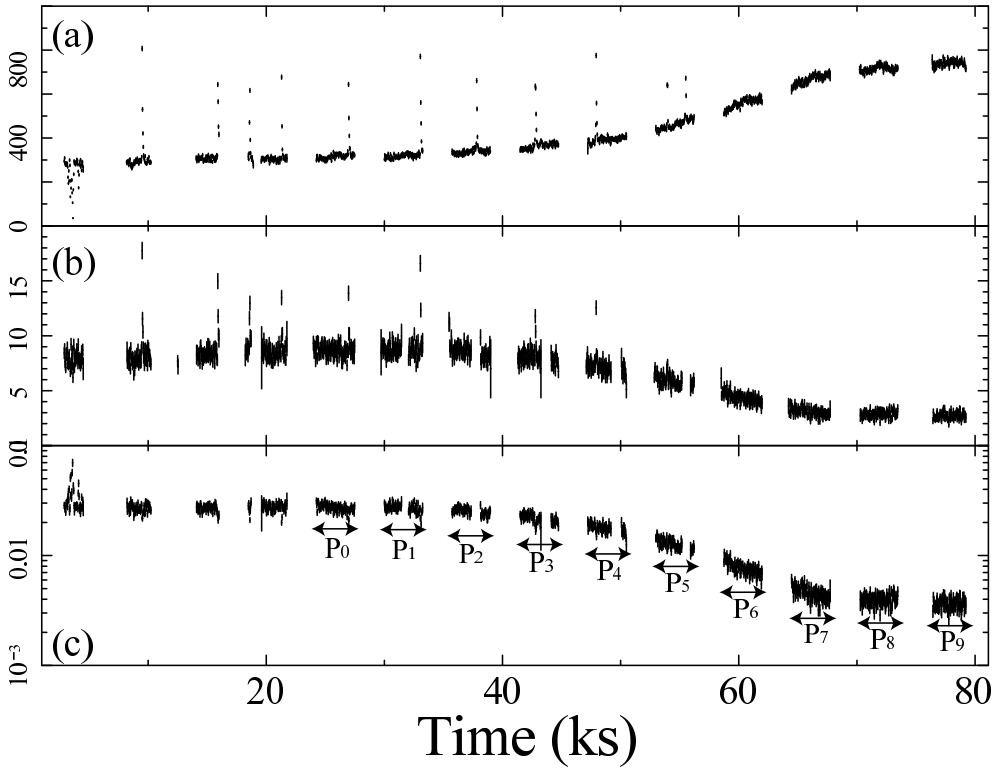

Figure 4.6: Short-term light curves of Aql X-1 on MJD 55855 (2011/10/21) capturing a moment of the hard-to-soft state transition. Panels (a) and (b) are 32s-binned curves of XIS-FI ($0.7 - 10$ keV) and HXD-PIN ($12 - 60$ keV), respectively. Panel (c) shows the ratio PIN/XIS as the hardness.

4.4 Other Sources

Below, we briefly introduce the *Suzaku* observations of the sources selected in §4.1.2 other than Aql X-1.

4.4.1 4U1608-52

Like Aql X-1 (§4.3), 4U1608-52 is a recurrent transient with a typical recurrence period of ~ 85 or ~ 150 days (Lochner & Roussel-Dupre 1994). The *Suzaku* observations of this source were performed in 2010 March, which are divided into four. As shown in figure 4.7 (a), the four caught a decaying phase of an outburst, which involved a soft-to-hard state transition around MJD 55272 because of a rapid increase of the hardness ratios. In the light curve, data from the *Swift*/BAT (Barthelmy et al. 2005) were utilized for the hard band ($12 - 50$ keV). Among the four, the latter two (404044030 and 404044040), performed after the transition, provide the hard-state data to be analyzed in Chapter 5. The two hard-state observations may correspond to the phase between Obs-D1 and Obs-D2 in the case of Aql X-1 (§4.3.1).

The short-term *Suzaku* light curves obtained on the two occasions are shown in figure 4.7 (panels b and c). On the first occasion, the source exhibited type-1 bursts (Belian et al. 1976; Murakami et al. 1980; Nakamura et al. 1989) at least twice in a gross time coverage of 14 ks (net exposure of ~ 80 ks). It also varied; we hence divide the observation into the first 20 ks (I_1) when the source was $\sim 30\%$ brighter in the soft band, a middle 15 ks (I_2) when the hardness increased by $\sim 30\%$, and the remaining 35 ks (I_3). On the other hand, neither type-1 bursts nor intensity variations were observed in the 2nd observation (404044040). We hence produce its spectrum by integrating the whole exposure time.

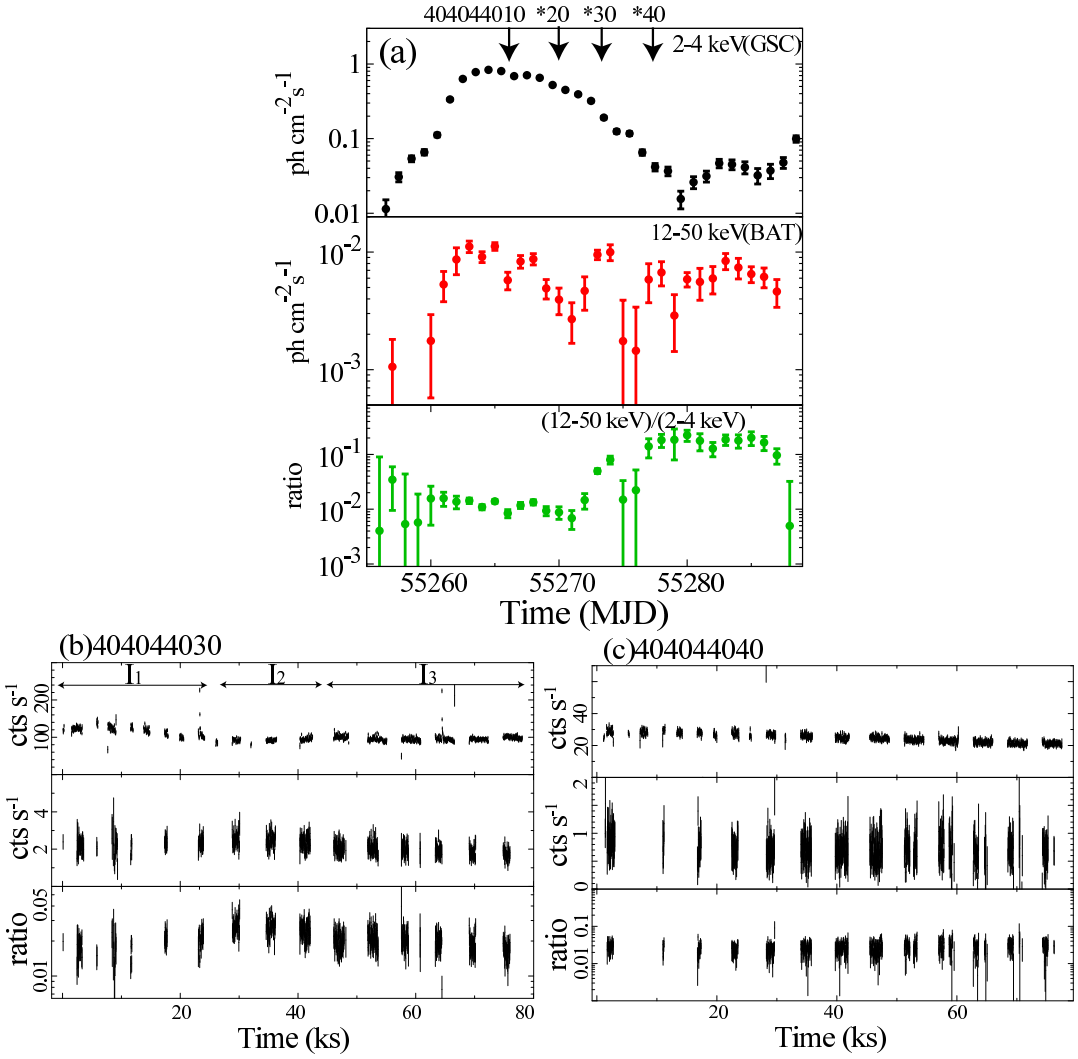

Figure 4.7: Long-term (1-day binned) and short-term (32-s binned) light curves of 4U1608-52. The former (panel a) shows the count rates of the *MAXI* /GSC ($2-4$ keV), that of the *Swift*/BAT ($12-50$ keV), and their ratios around an outburst in 2010 March. The epochs of *Suzaku* observations are indicated therein. The latter (panels b and c) are *Suzaku* light curves in the hard state (404044030, 404044040) in the same manner as figure 4.6.

4.4.2 4U1636-536

As shown in figure 4.8 (a), *Suzaku* observations of 4U 1636-536 were conducted in 2007 on five occasions (separated by $2 \sim 30$ days), when the source exhibited time variations on a time scale of ~ 10 day. Among them, the first one (401050010) caught a period when the soft-band flux dropped while the hard band increased by ~ 1 order of magnitude, and is considered to be in the hard state as we expected in §4.1.2. In Chapter 5, we hence analyze only the 1st data set. In contrast to the long-term behavior, the short-time light curve, figure 4.8 (b), recorded no time variations above 10%.

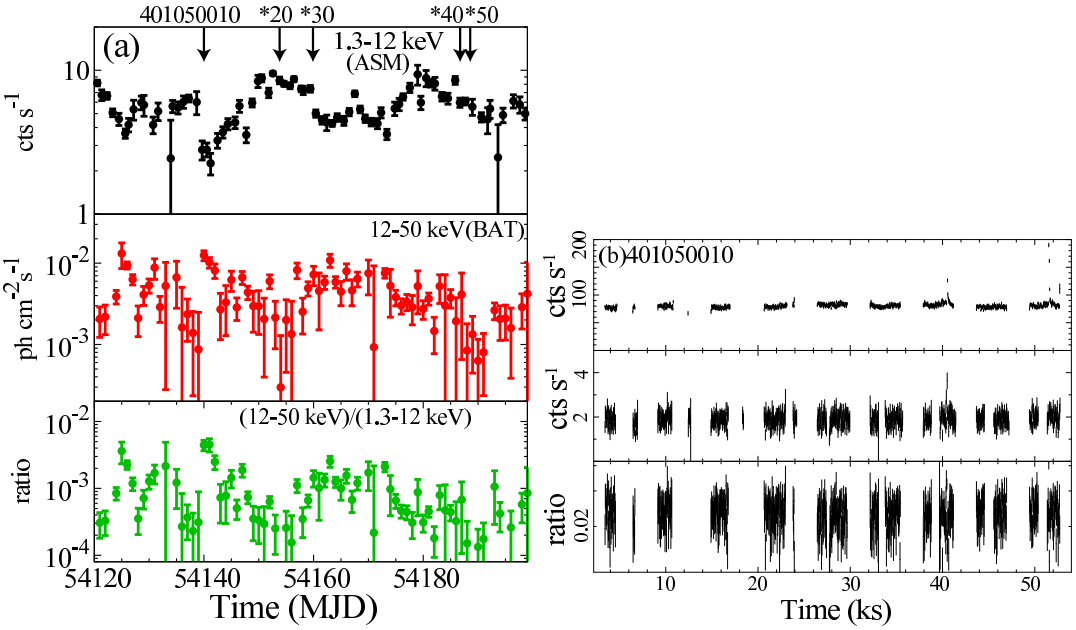

Figure 4.8: The same as figure 4.7 but for 4U 1636-536. The count rates in the soft band (panel a) were obtained with the *RXTE*/ASM ($1.3 - 12$ keV).

4.4.3 4U1705-44

As shown in table 4.1, observations of 4U1705-44 by *Suzaku* were conducted in 2006, 2007, and 2012. Since that in 2007 caught the soft state with very high $L_{\rm abs}$ ($> 10^{37}$ erg s^{-1}) and low H (< 0.01), we utilize the other two, those in 2006 and 2012. As shown in figure 4.9 (a), observations in 2006 were divided into three, of which the first one (401046010) caught a rising phase of an outburst. About 8 days later, the hard-band flux dropped by ~ 1 order of magnitude, which is interpreted as the hard-to-soft transition. Therefore, 401046010 may be compared with Aql X-1 Obs-R1. The *Suzaku* light curve of 401046010 shown in panel (c) resembles that of Aql X-1 Obs-R1, in insignificant variations ($< 10\%$) and a couple of type-1 bursts. The three observations (401046010-401046030) were previously analyzed by Lin et al. (2010). These authors showed that the first one was actually in the hard state while the other two the soft state, and modeled spectra of the three by optically-thick emission (BB or `diskBB`) and a power-law with cutoff around ~ 40 keV.

The observation in 2012 was conducted with a long exposure of 82 ks. Figure 4.9 (b) shows a long-term light curve around that period, which indicates that the observation caught the hard state because of a relatively high hardness ratio ($12 - 50$ keV vs. $2 - 4$ keV), although it lacks the soft-band information in $56012 - 56016$ MJD. Its *Suzaku* light curve is shown in figure 4.9 which reveals about 5 type-1 bursts. Since a gradual flux increase seen from the beginning to the end is within 20%, we produce time-averaged

spectrum for following analysis in Chapter 5.

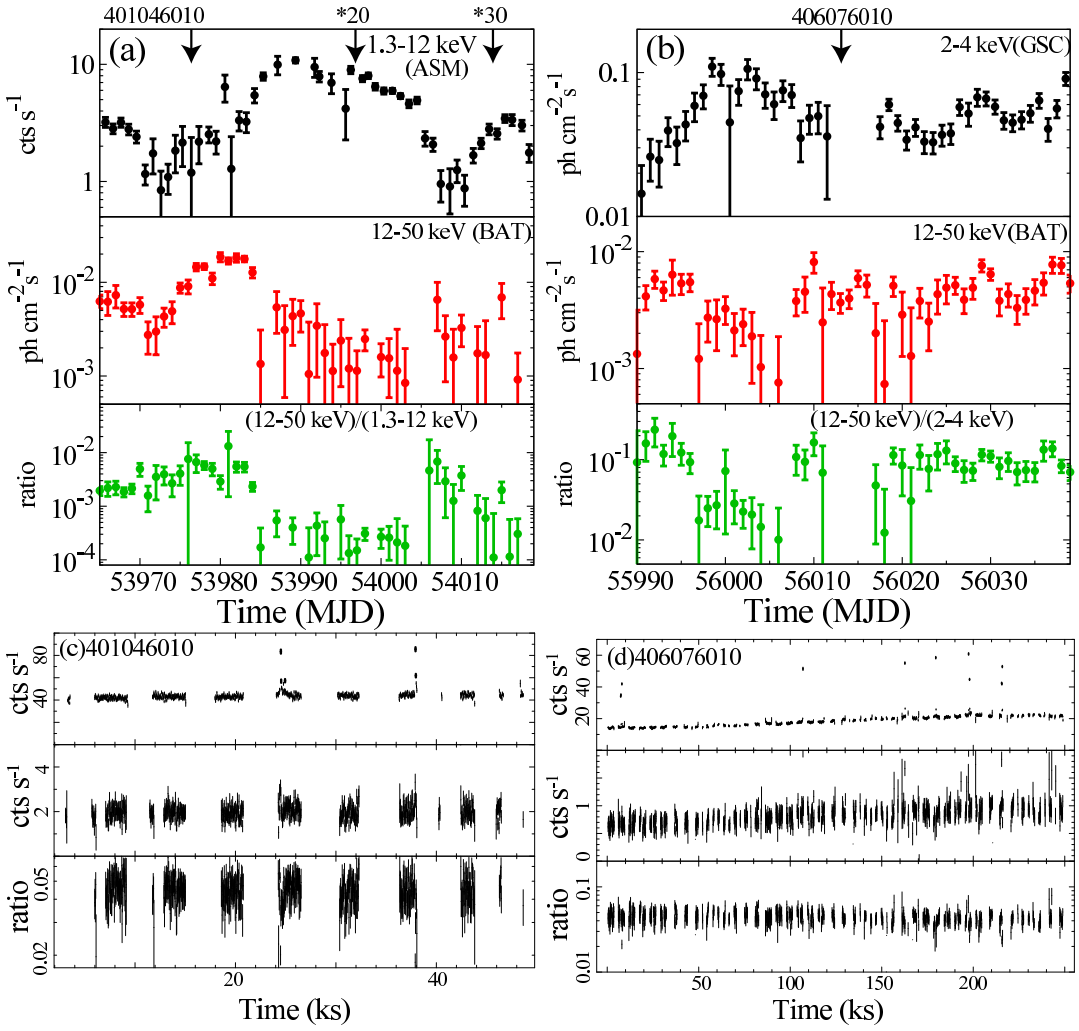

Figure 4.9: The same as figure 4.7, but for 4U1705-44.

4.4.4 4U1812-12

The source 4U1812-12 is known as a persistent source, always residing in the hard state (Wilson et al. 2003; Muno et al. 2005; Tarana et al. 2006). This is the reason why we proposed its *Suzaku* observation as a good target for the hard state study. Our approved *Suzaku* observation was performed in 2011 October. Long-term light curve around then is shown in figure 4.10 (a). It stayed almost constant (although only the hard-band one is available), so did the *Suzaku* light curve one in panel (b). The luminosity of $L_{\rm abs} = 1.4 \times 10^{36}$ erg s^{-1} was also consistent with that obtained previously as 2×10^{36} erg s^{-1} in 2005 (Tarana et al. 2006).

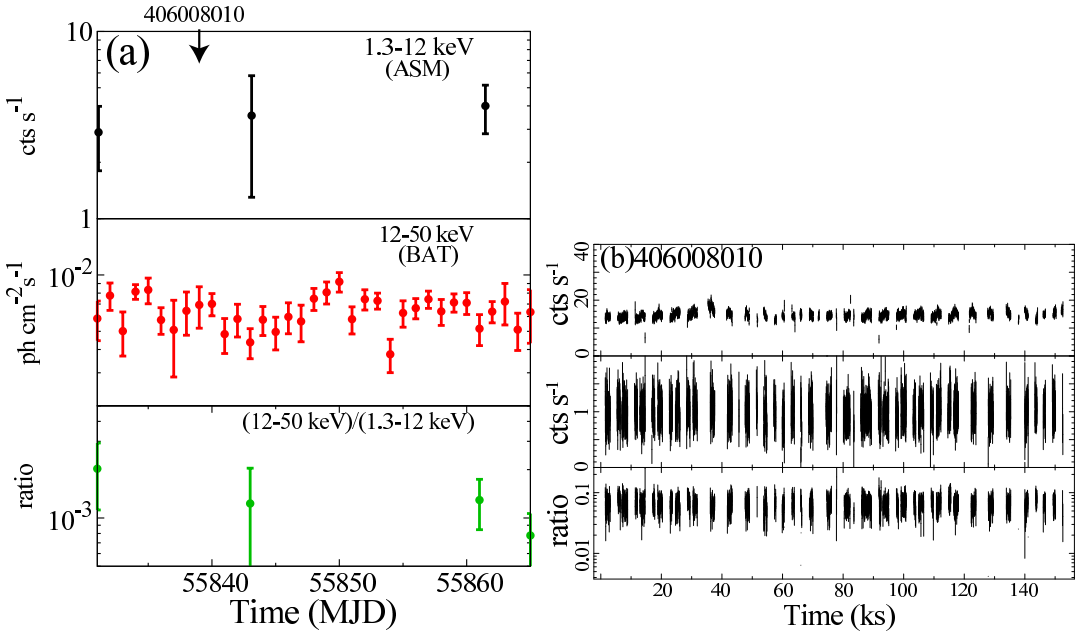

Figure 4.10: Light curves of 4U1812-12 in the same manner as figure 4.7.

4.4.5 Cen X-4

Centaurus X-4, a recurrent transient by far the dimmest source among our data sets, because its luminosity was $L_{\rm abs} = 5.1 \times 10^{31}$ erg s^{-1} . *Suzaku* observation was conducted in 2009/1/16, for a long exposure as $>$ 120 ks. A long-term light curve around the date is shown in figure 4.11, where no significant variation was seen. Although the time variability by a factor of $\sim$ 3 within 4 days is reported by Campana et al. (1997), the *Suzaku* light curve in panel (b) can be regarded as constant within the statistical errors. This phase may correspond to those of Aql X-1 Obs-D6 and Obs-D7 which also have very low luminosity as $L_{\rm abs} \lesssim 10^{34}$ erg s^{-1} . A spectrum of this observation was analyzed by Cackett et al. (2010), and was suggested to consist of optically-thick emission and a very hard power-law-like component with its photon index of $\sim$ 0.7. The source was undetectable with the HXD.

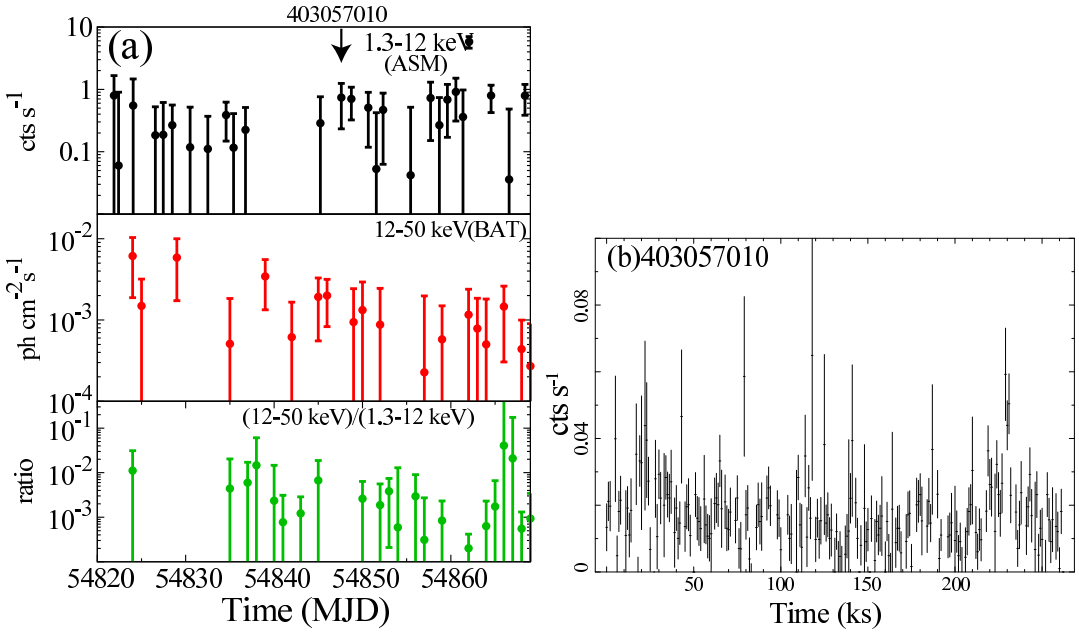

Figure 4.11: The same as figure 4.7 but for Cen X-4. Panel (b) shows a light curve by the *Suzaku*/XIS binned with 1000 s; no HXD results are available.

4.4.6 GS1826-238

GS1826-238 was discovered by *Ginga* in 1988 (Makino 1988). This source is known to be almost persistently in the hard state (Cocchi et al. 2011) and exhibit quasi-periodic type-1 bursts every ~ 5.8 hours (Ubertini et al. 1999). As shown in figure 4.12 (a), the hard-band count rates were relatively high and the long-term variation was insignificant. An observation of this source by *Suzaku* was conducted in 2009 October with a relatively long exposure (82 ks). The *Suzaku* light curve shown in panel (b) actually reveals 7 type-1 bursts with an interval of $\sim$ 20 ks ($\sim$ 6 hours), although some more may be hidden in earth occultation periods.

In this *Suzaku* observation, the XIS was affected by the pile up effect, as mentioned in §4.2. Since the effects would be limited to be $\lesssim 3\%$ outside $30''$ in the XIS image, we produced its time-averaged spectrum for following Chapter by discarding the central $30''$ from the source region.

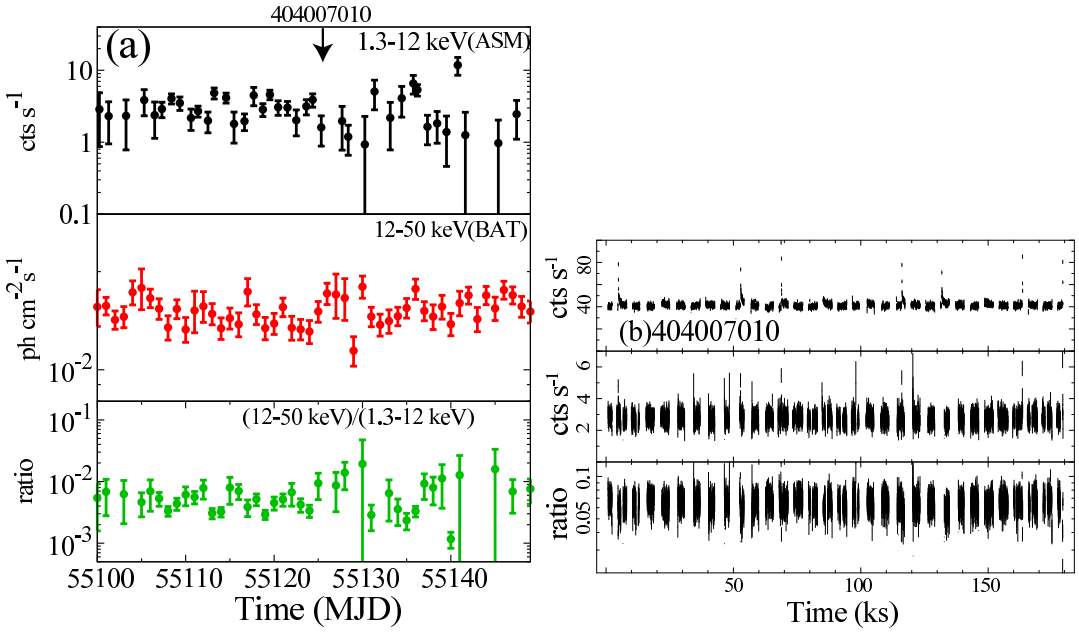

Figure 4.12: Light curves of GS1826-238 with the same panel composition as figure 4.7.

4.4.7 SLX1737-282

The persistent source SLX1737-282 was discovered by *Spacelab*-2 in 1985 (Skinner et al. 1987). It was suggested to be an LMXB by spectral and timing analysis with *ASCA* (Sakano et al. 2002), and later confirmed by the presence of thermo-nuclear bursts (in 't Zand et al. 2002). It was observed by *Suzaku* in 2006 for a duration of 29 ks. As shown in panel (b), *Suzaku* light curve of this source exhibited some flares with duration of $\gtrsim 1$ ks. We exclude these periods when producing a spectrum for the analysis in Chapter 5.

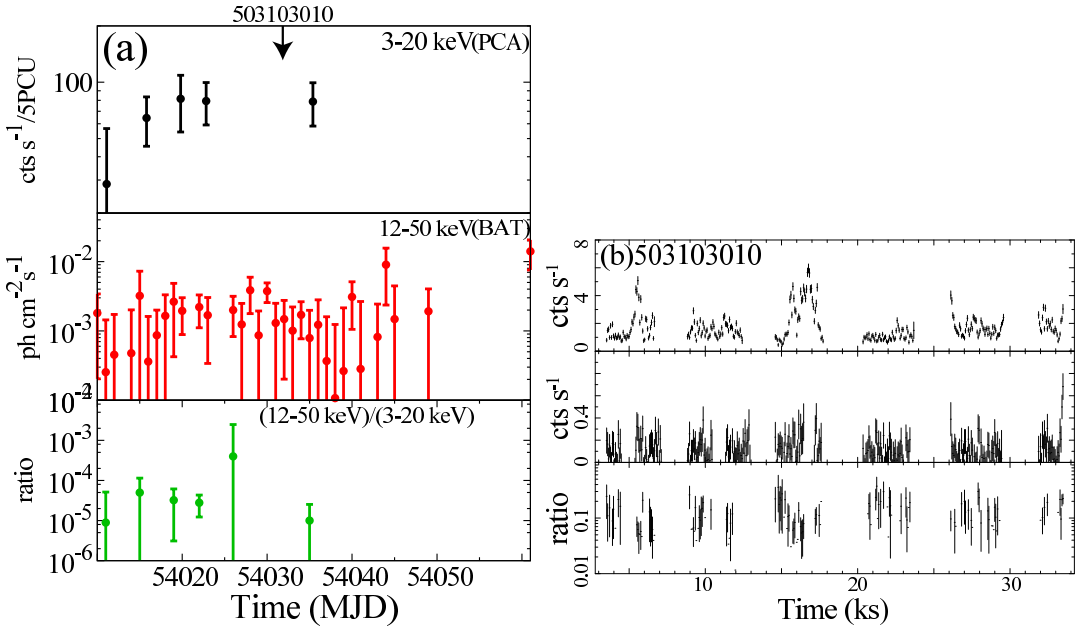

Figure 4.13: The same as figure 4.7 but for SLX1737-282. In panel (a), *RXTE*/PCA monitoring data ($3 - 20$ keV) was employed.

Chapter 5

DATA ANALYSIS AND RESULTS

In this Chapter, we examine the LMXB spectra mainly in their hard state. As declared in §4.3, the analysis begins with the Aql X-1 data sets, obtained at various levels of $L_{\rm abs}$ occasions. On the way tracing luminosity-dependent changes of the Aql X-1 spectra, the other sources introduced in §4.4 are also examined in the same manner.

5.1 Aql X-1: Soft-to-Hard Transition

5.1.1 Overview

All the seven background-subtracted spectra of Aql X-1, acquired in the decaying phase of the 2007 outburst (§4.3.1), are displayed in figure 5.1. Among them, only Obs-D1 (red) exhibits a very soft spectrum, while the others hard spectra extending up to 100 keV, thus reconfirming our quick-look estimation in §4.1.2. As already reported in Sakurai et al. (2012), Obs-D1 clearly caught the soft state, while the other six all the hard state with a wide range of $L_{\rm abs}$ from 2.3×10^{36} erg s^{-1} to 9.1×10^{33} erg s^{-1} .

Below, we divide the seven observation into four groups; Obs-D1 as the soft state with $L_{\rm abs} \sim 0.1 L_{\rm edd}$; Obs-D2, Obs-D3, and Obs-D4 as the hard state with $L_{\rm abs} \sim 0.01 L_{\rm edd}$; the intermediate Obs-D5 ($L_{\rm abs} \sim 0.001 L_{\rm edd}$); and Obs-D6 and Obs-D7 as the very dim hard state with $L_{\rm abs} \sim 10^{-4} L_{\rm edd}$. We analyze the four in this order, corresponding to a descending order of $L_{\rm abs}$, to see changes of the spectra and the implied accretion physics as $\dot{M}$ decreases.

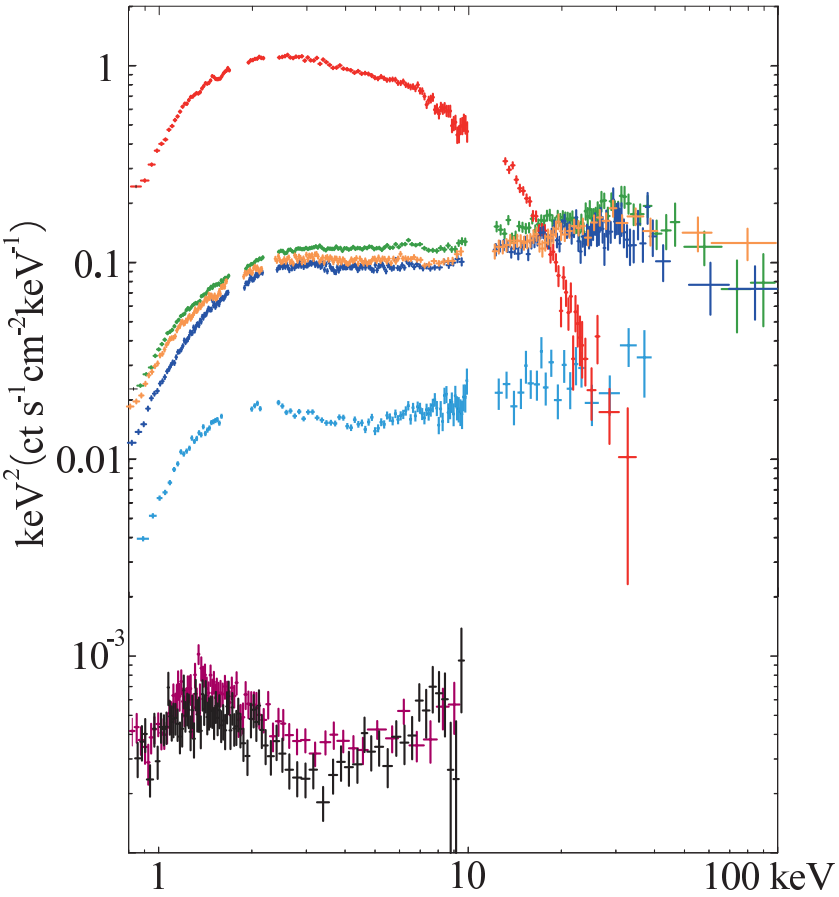

Figure 5.1: Background-subtracted *Suzaku* spectra of Aql X-1, obtained during a decaying phase of the outburst in 2007 (§4.3.1). The spectrum of Obs-D1, Obs-D2, ..., and Obs-D7 is shown in red, yellow, green, dark blue, light blue, purple, and black, respectively.

5.1.2 The soft state with $L_{\rm abs} \sim 0.1 L_{\rm edd}$

Since Aql X-1 showed little ($< 10\%$) time variations in the soft state (§4.3.1), we below analyze an exposure-averaged spectrum. Let us start our spectral fitting with the canonical model (Mitsuda et al. 1984, 1989; Makishima et al. 1989) already described in §2.1.2. This model is hereafter denoted as DB; all model abbreviations used in this Chapter are listed in table 5.1. Emission from a multi-color disk is represented by `diskBB` model (equation 2.8 in §2.2.2), with its inner-edge temperature $T_{\rm in}$ and its inclination-uncorrected inner radius $R_{\rm in}/\sqrt{\cos i}$ as free parameters. Since i is usually uncertain unless the source exhibits dip or eclipse phenomena, it is assumed to be 45° throughout our analysis. The effect of interstellar absorption is represented by `wabs` model (Morrison & McCammon 1983),

$$\texttt{wabs}(E) = \exp\left(-N_{\rm H}\sigma(E)\right), \tag{5.1}$$

where its column density $N_{\rm H}$ is usually left free, and $\sigma(E)$ is the photo-electric cross-section assuming the solar abundance by Anders & Ebihara (1982). This absorption factor is hereafter multiplied to all spectral models (e.g. DB means `wabs`×[`diskBB`+BB]). The DB model as a function of energy is explicitly written as

$$\mathrm{DB}(E; T_{\rm in}, R_{\rm in}, T_{\rm bb}, R_{\rm bb}, N_{\rm H}) = e^{-N_{\rm H}\sigma(E)} \left[f_{\rm mcd}(E; T_{\rm in}, R_{\rm in}) + K \left(\frac{R_{\rm bb}}{D} \right)^2 I(E; T_{\rm bb}) \right] \quad (5.2)$$

where D is the distance, K is a certain constant, and $f_{\rm mcd}$ and I are from equation 2.8 and equation 2.5, respectively.

Figure 5.2 (a) shows a model fit to the Obs-D1 spectrum with DB. Thus, significant features are seen around 1.8 keV, 2.3 keV, and weakly at $\sim$ 1.5 keV. As described in §4.2.1, these are due to instrumental effects: Si K-edge absorption (1.84 keV) in the XIS CCD, Au M-edge ($\sim$ 2.3 keV) in the XRT reflector, and Al K-edge (1.56 keV) in the XRT substrate. Since they are not fully accounted for by the XIS response, these bands are cut from the XIS spectra when the statistics are sufficiently high. Together with these, $\lesssim$ 15 keV band in the HXD-PIN spectra is not included either, because its lower discriminator is set around $10 - 12$ keV, and the band below $\sim$ 15 keV suffers thermal noise which depends on the detector temperature. After discarding the range of $1.7 - 2.4$ keV (XIS) and < 15 keV (PIN) in this case, as shown in figure 5.2 (b), DB roughly reproduced the spectrum, with $T_{\rm in} \sim 0.8$ keV, $R_{\rm in} \sim 10$ km, the BB temperature of $T_{\rm bb} \sim 1.9$ keV, and the BB radius of $R_{\rm bb} \sim 2$km. The best-fit parameters did not change significantly by masking the energy regions. However, the fit left significant residuals particularly in > 15 keV, and gave an unacceptable reduced χ^2 of 2.00(329).

Table 5.1: Our spectral modelings and their free parameters.

Abbr.[a]	Composition	Free parameters
DB	`diskBB + bbodyrad`	$T_{\rm in}, R_{\rm in}, T_{\rm bb}, R_{\rm bb}$
$\mathrm{C_d}$	`comp(diskBB)`	$T_{\rm in}, R_{\rm in}, \tau, T_{\rm e}$
$\mathrm{C_b}$	`comp(bb)`	$T_{\rm bb}, R_{\rm bb}, \tau, T_{\rm e}$
$\mathrm{BC_b}$	`bbodyrad+comp(bb)`	$T_{\rm bb}, R_{\rm bb}, \tau, T_{\rm e}$
$\mathrm{BC_d}$	`comp(disk) + bbodyrad`	$T_{\rm in}, R_{\rm in}, T_{\rm bb}, R_{\rm bb}, \tau, T_{\rm e}$
$\mathrm{DC_b}$	`diskBB + comp(bb)`	$T_{\rm in}, R_{\rm in}, T_{\rm bb}, R_{\rm bb}, \tau, T_{\rm e}$
$\mathrm{C_dC_b}$	`comp(disk) + comp(bb)`	$T_{\rm in}, R_{\rm in}, T_{\rm bb}, R_{\rm bb}, \tau, T_{\rm e}$

[a] Abbreviation.

The residuals in figure 5.2 (b) indicate Comptonization effects on BB, as pointed out repeatedly in previous studies (Mitsuda et al. 1989; Gierlinski & Done 2002; Lin et al. 2007; Cocchi et al. 2011; Tarana et al. 2011b; Takahashi et al. 2011). Therefore, a modified model, namely a disk blackbody plus a Comptonized BB (hereafter $\mathrm{DC_b}$:

table 5.1), was next applied to to the spectrum. As a Comptonization numerical code, we here employed `nthcomp` (Lightman & Zdziarski 1987; Lightman et al. 1987; Zdziarski et al. 1996; Zycki et al. 1999) which provides a numerical solution to the Kompaneets equation (§2.3) with a certain approximation which is valid in $\tau \gtrsim 2$ regime (Zdziarski et al. 1996). The code uses the spectral slope

$$\Gamma = -\frac{1}{2} + \sqrt{\frac{9}{4} + \frac{4}{y}} \tag{5.3}$$

as a free parameter, instead of the optical depth. Here,

$$y = \frac{4kT_{\rm e} \cdot \tau(1 + \tau/3)}{m_{\rm e}c^2} \tag{5.4}$$

is the Compton y-parameter, with τ the optical depth.

As shown in figure 5.2 (c), the $\rm DC_b$ model (`wabs` $\times$ [`diskBB` + `nthcomp`(BB)]) successfully removed the hard-band excess, and made the fit fully acceptable with $\chi^2/\nu = 1.16(328)$. Table 5.2 shows the best-fit parameters. Hereafter, errors in tables represent 90% confidence range, and unabsorbed luminosity $L_{\rm x}$ is calculated by integrating the spectral model over a sufficiently wide range of [1 eV, 10 MeV]. The weak Comptonization is characterized by a rather low $T_{\rm e} \sim 3$ keV and a steep $\Gamma \sim 2.9$, or a y-parameter of 0.10 ± 0.05. The result appears to be physically reasonable from following four viewpoints. First, the BB temperature, $T_{\rm bb} \sim 1.3$ keV, is a factor of ~ 1.7 higher than the disk temperature $T_{\rm in} \sim 0.76$ keV. Second, the innermost disk radius $R_{\rm in} \sim 13$ km is larger than the canonical NS radius of 10 km, and the BB radius $R_{\rm bb} \sim 3$ km is smaller than 10 km. Third, the value of $T_{\rm bb}$ is lower than the Eddington temperature ~ 1.9 keV at the NS surface. And fourth, the unabsorbed flux of the disk, $F_{\rm disk} \sim 3.1 \times 10^{-9}$ erg s^{-1} cm^{-2} , and of the BB, $F_{\rm bb} \sim 1.9 \times 10^{-9}$ erg s^{-1} cm^{-2} , have a ratio of $F_{\rm bb}/F_{\rm disk} \sim 0.62$. The ratio is expected to be $2/\pi = 0.63$ at an inclination $i = 45^\circ$ (Mitsuda et al. 1984), from virial theorem (§2.2.2) and assuming the BB geometry to be a belt shape on the NS equator. This result provide a posteriori justification of $i = 45^\circ$.

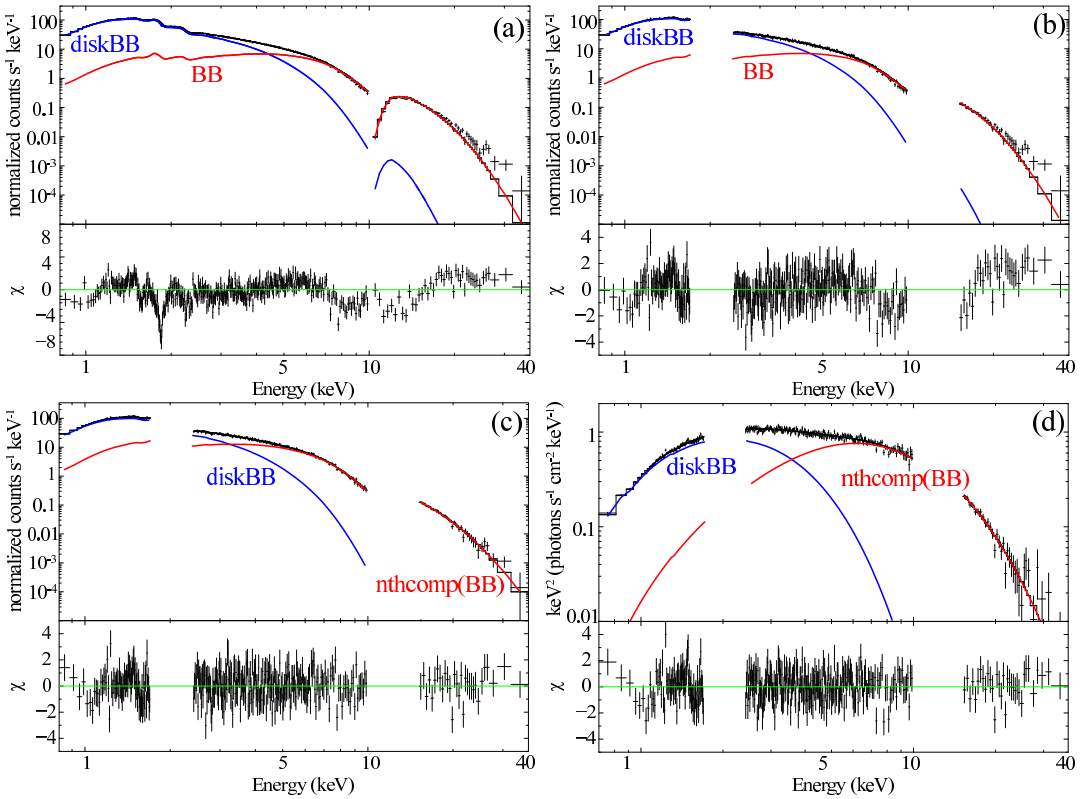

Figure 5.2: Simultaneous fitting of XIS-FI and HXD-PIN spectra of Aql X-1 in the soft state (Obs-D1). Employed models are `diskBB+bbodyrad` (panels a and b) and DC_b (panels c and d). Panels (a) and (b) are before and after discarding the two energy bands (see text). Panel (d) shows the same fit as (c), but in the response-resolved $\nu F\nu$ form. Each lower panel shows the residuals. In this figure and followings as well, the components which originate from the disk and the NS blackbody are colored in blue and red, respectively.

Table 5.2: The soft state (Obs-D1) best-fit parameters with model DC_b.

Component	Paramater	Value
wabs	$N_{\rm H}$ (10^{22}cm^{-2})	0.36 ± 0.01
diskBB	$T_{\rm in}$ (keV)	$0.70^{+0.02}_{-0.03}$
	$R_{\rm in}$ (km)[ab]	19 ± 1
nthcomp	$T_{\rm bb}$ (keV)	1.2 ± 0.1
(BB seed)	$R_{\rm bb}$ (km)[a]	4 ± 1
	$T_{\rm e}$ (keV)	$3.1^{+0.9}_{-0.5}$
	Γ	$2.9^{+0.6}_{-0.5}$
	τ	$5.9^{+0.8}_{-0.4}$
Fit goodness	$\chi^2_\nu(\nu)$	1.08 (327)
Luminosity	$L_{\rm x}$ (erg s^{-1})	1.68×10^{37}

[a]Assuming the distance of 5.2 kpc without propagating its error of 0.7 kpc.

[b]Assuming the source inclination of 45 degree, and corrected according to equation 2.7.

5.1.3 The hard state with $L_{\rm abs} \sim 0.01 L_{\rm edd}$

As described in §5.1.1 and shown in figure 5.1, the subsequent three data sets, Obs-D2, Obs-D3, and Obs-D4, have similar intensity and spectra. In contrast to that of the soft state, these spectra are so hard as being flat in the $\nu F\nu$ form, approximated by a power law with a photon index of $\Gamma \sim 2$. As a representative of the three, we here start from the analysis of Obs-D3 since it has a little ($\sim 20\%$) higher $L_{\rm abs}$. Below, the absorbing column density of `wabs` is fixed to $N_{\rm H} = 0.36 \times 10^{22}$ cm^{-2} as derived with the soft-state spectrum (§5.1.2).

The power-law-like spectrum extending up to $\sim$ 100 keV, with a possible cutoff around several tens of keV, can be considered as an effect of strong Comptonization. Since the implied electron temperature is rather high (e.g. several tens keV), we utilize instead of `nthcomp`, `compPS` (Poutanen & Svensson 1996) which more accurately considers relativistic effects (e.g. the Klein-Nishina cross-section instead of Thomson's), though it is available only in a relatively optically-thin regime as $\tau \leq 3$ where the iterative calculation converges. This model is available under several coronal geometries, like a slab and a hemisphere. We employed it under spherical geometry, namely the geometry parameter of 4 in XSPEC. In §5.3.3, the two odes, `nthcomp` and `compPS` are cross calibrated.

The possible simplest scenario is that the hard spectrum is generated by Comptonization of a single seed-photon population. We hence examined whether the spectrum can be reproduced by Comptonization of either the disk emission or the BB from the NS surface, hereafter $\rm C_d$ and $\rm C_b$ (table 5.1), respectively. As shown in figure 5.3 (a) and (b), however, neither of them was able to reproduce the spectrum sufficiently, with $\chi^2/\nu = 2.19(367)$ for $\rm C_d$ and $\chi^2/\nu = 4.85(367)$ for $\rm C_b$. The former and the latter gave the seed temperature of $T_{\rm in} \sim 0.6$ and $T_{\rm bb} \sim 0.3$, respectively. Both left significant positive residuals (or "soft excess") at $\lesssim 1$ keV, and failed to explain the highest several data points as well. The residuals in the soft band suggests the presence of another optically-thick component that is relatively free from the Comptonization.

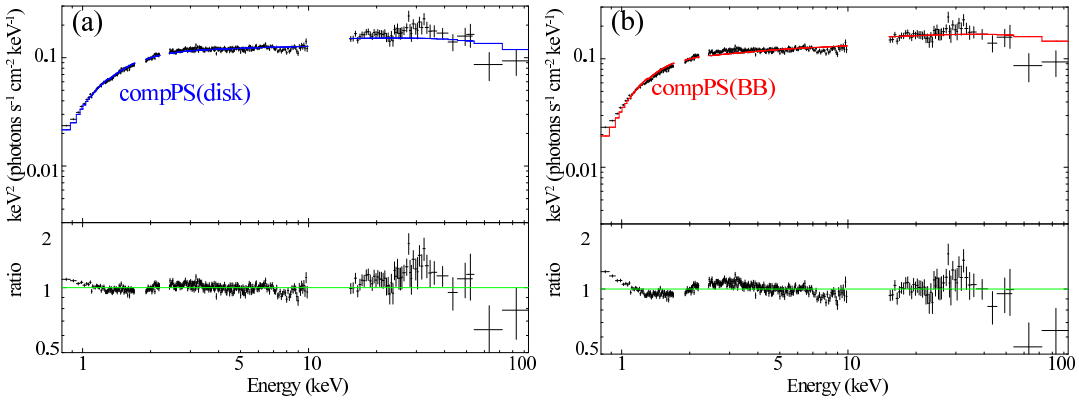

Figure 5.3: Spectral fits to Obs-D3 with models C_d (panel a) and C_b (panel b). Lower panels show ratios to the models. As written in the figure, The blue represents the disk or its Comptonization, and the red the BB or its Comptonization.

As the single photon population was unsuccessful, we should consider the co-existence of at least two emission components, namely both the disk emission and the BB, just like the soft-state case. Then, there are mainly three possibilities; the disk emission is Comptonized but the BB is directly-visible (hereafter BC_d: table 5.1); the disk is naked but the BB (NS) is covered with a corona (DC_b); both are covered with corona(e), and Comptonized to different degrees. We next tried the simpler former two modelings. As shown in figure 5.4, the soft excess in $\lesssim 1$ keV has disappeared in both cases with the help of the additional soft optically-thick component, namely, BB with $T_{\rm bb} \sim 0.16$ keV for BC_d, and `diskBB` with $T_{\rm in} \sim 0.29$ keV for DC_b. The fit has improved to $\chi^2/\nu = 1.33(365)$ for BC_d and $\chi^2/\nu = 1.32(365)$ for DC_b, although they are not yet unacceptable. The remaining problem is that they still leave significant negative residuals in $7-10$ keV and a hump around 30 keV.

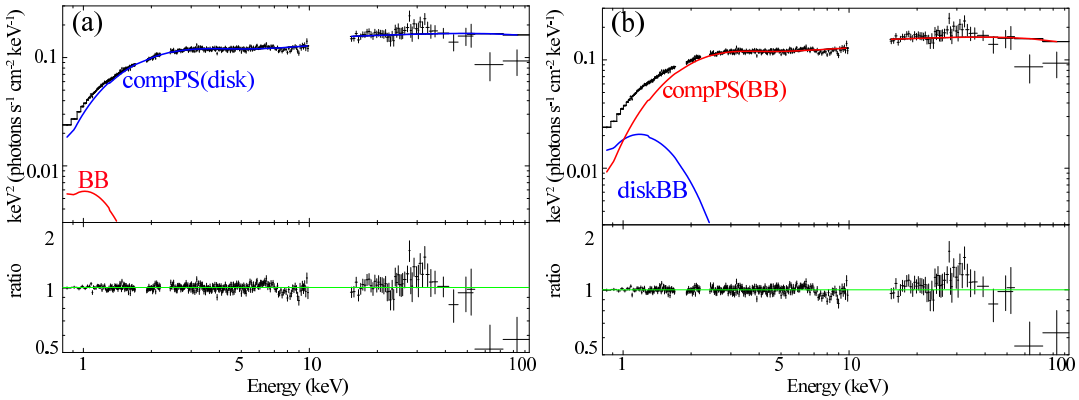

Figure 5.4: Same as figure 5.3, but with models BC_d (panel a) and DC_b (panel b), without reflection component.

In figure 5.4, the step-like negative residuals in $\gtrsim 7$ keV indicate an iron K-edge (7.1 keV) absorption. In addition, the positive hump at ~ 30 keV and negative residuals

above 40 keV are suggestive of Compton down scattering of a fraction of the continuum by some cold materials. Therefore, we further considered a contribution from Compton reflection by cold matters (e.g. White et al. 1988; Lightman & White 1988; Magdziarz & Zdziarski 1995). It is incorporated in the `compPS` model, with mainly two free parameters: the solid angle of matter as seen from the radiation source (the NS in the present case), and its abundance. An iron K_α line (6.4 keV) accompanied by the K edge absorption is also included in the model, with its width fixed to 0.1 keV and intensity allowed to vary. Then, as shown in figure 5.5, both models have successfully reproduced the spectrum in the whole energy band, with improved and acceptable χ^2/ν of 1.11 (363) for BC_d and 1.09 (363) for DC_b. The derived parameters are shown in table 5.3.

Now we have obtained the two possible model compositions, BC_d and DC_b, both with the reflection component. Although they cannot be distinguished from the fit goodness, a distinction may be possible from a physical point of view. Among the physical quantities listed in table 5.3, the radii $R_{\rm in}$ and $R_{\rm bb}$ are important since they carry geometrical information. Thanks to the large effective area of the XIS+XRT, the parameters of the weak optically-thick emission have been constrained as $T_{\rm bb} = 0.16^{+0.01}_{-0.02}$ keV and $R_{\rm bb} = 45^{+15}_{-10}$ km in BC_d, and $T_{\rm in} = 0.28^{+0.02}_{-0.03}$ keV and $R_{\rm in} = 27 \pm 4$ km in DC_b at 90% confidence. Even considering a usual systematic error of 1% as a calibration uncertainty of the XIS, the errors of the parameters stayed unchanged as $T_{\rm in} = 0.28^{+0.02}_{-0.03}$ keV in DC_b, for example. Thus, the statistical error is considered to be dominant over the systematic error in this data set. Here, the parameter errors have been derived by computing confidence contours as shown in figure 5.6, where all the other relevant parameters are left free (except $N_{\rm H}$). The 90% confidence level here is slightly larger than those in table 5.3 because the former assumes a χ^2 distribution with degree of freedom of $\nu = 2$, while the latter that of $\nu = 1$. When $N_{\rm H}$ is allowed to vary, for reference, the DC_b fit gives almost the same goodness of $\chi^2/\nu = 1.09(362)$ with $N_{\rm H} = 0.38^{+0.07}_{-0.05} \times 10^{22}$ cm^{-2}, and `diskBB` parameters of $T_{\rm in} = 0.27 \pm 0.04$ keV and $R_{\rm in} = 29^{+20}_{-9}$ km, which are consistent with those with $N_{\rm H}$ fixed and have larger errors. As an example of worse fit apart from the best one, figure 5.5 (c) shows a DC_b fit with $T_{\rm in} = 0.40$ keV fixed. It actually leaves significant residuals in $\lesssim 3$ keV and gave $\chi^2/\nu = 1.33(364)$.

From the examination above, we can conclude that $R_{\rm bb}$ in the former BC_d modeling exceeds the canonical NS radius, and the seed emission, the disk, has small inner radius as $R_{\rm in} = 5 \pm 1$ km $\ll 10$ km. These give an unphysical relation of relation of $R_{\rm bb} > 10$ km $> R_{\rm in}$. Even if the dilution effect could not be neglected, it would only make the radius apparently smaller, so that the too large value of $R_{\rm bb}$ remains unexplained. Thus, the model BC_d can be ruled out. The model DC_b, in contrast, satisfies the conditions as $R_{\rm bb} \leq 10$ km $\leq R_{\rm in}$ and $T_{\rm in} < T_{\rm bb}$, with a slightly better χ^2/ν.

The difference between BC_d and DC_b can be explained in the following way. The

soft excess has such a low temperature that it requires a large emission area, which is available with a disk but not with a NS surface. In contrast, the hard continuum is boosted by a very hot corona, so that it requires a relatively small number of seed photons that can be supplied by the NS surface. Finally, the electron temperature, ~ 50 keV, can explain the gradual data decline at $\gtrsim 50$ keV.

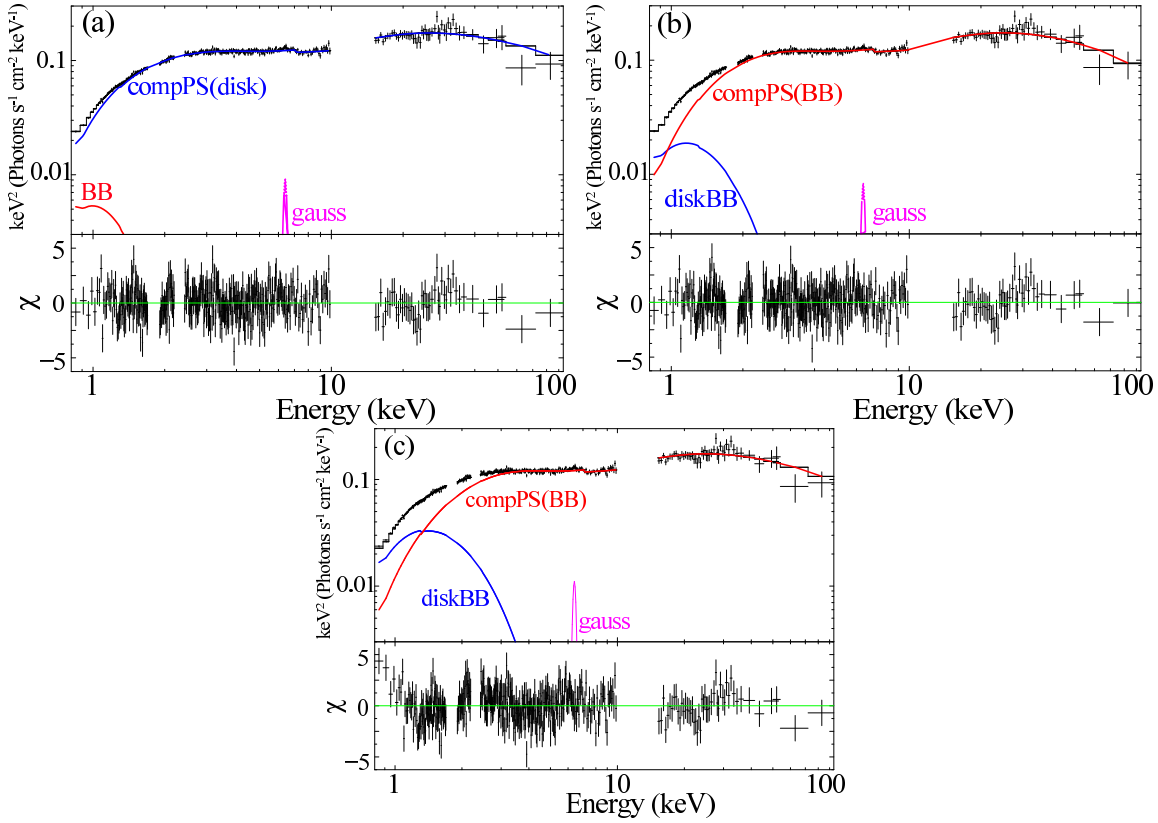

Figure 5.5: The same as figure 5.3, with models BC_d (panel a) and DC_b (panels b and c), but incorporating the reflection component and an iron K_α line (purple). In panel (c), the disk innermost temperature is fixed to $T_{in} = 0.4$ keV.

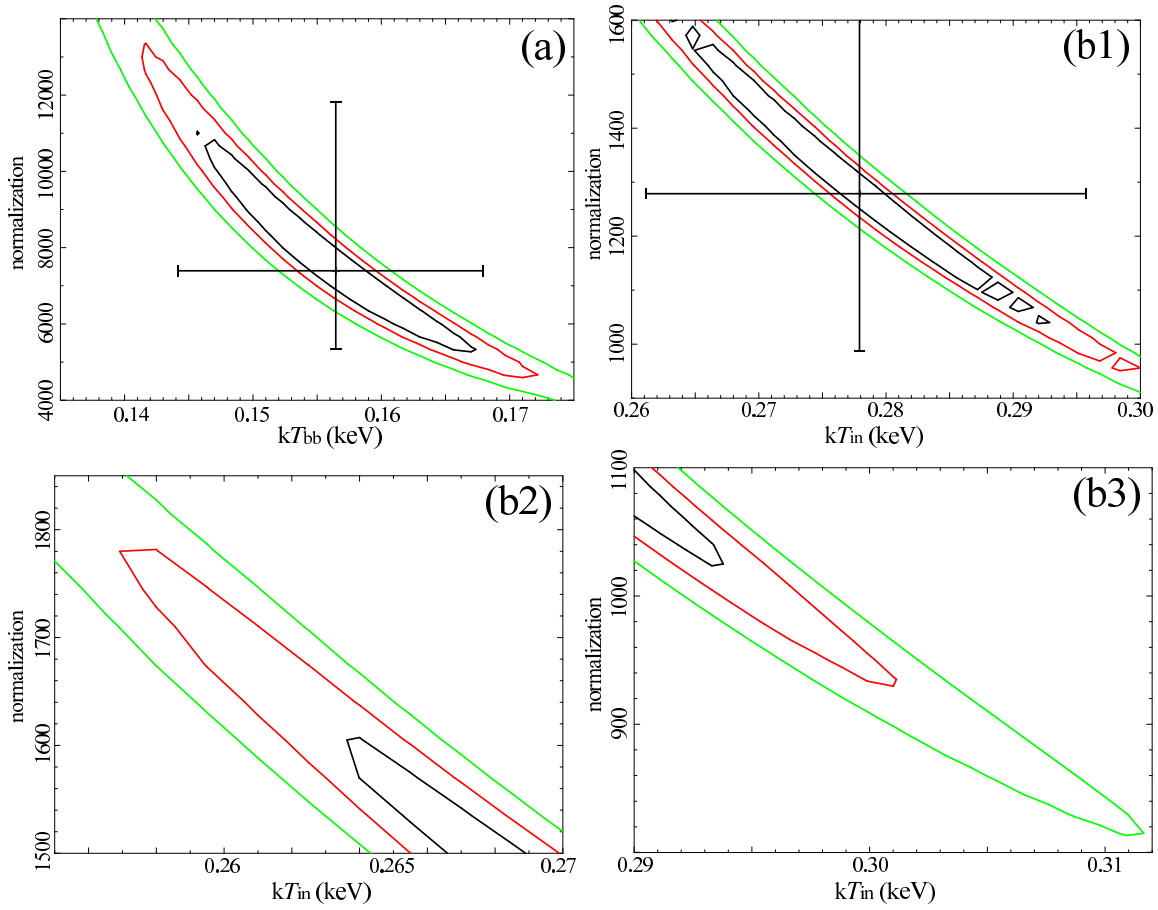

Figure 5.6: Chi-square confidence contours between the parameters of the optically-thick emission components, in the BC_d (panel a) and DC_b (panels b, c, and d) fits in figure 5.5. Panels (b1)−(b3) are the same contour plot, but were calculated and shown over separate T_{in} ranges for technical reasons. The best-fit values are summarized in table 5.3, and those of (T_{in}, normalization) are shown in a cross (corresponding to $\Delta\chi^2 = 2.7$). The black, red, green lines denote $\Delta\chi^2$ of 2.3 (68% confidence limit), 4.61 (90%), and 9.21 (99%), respectively. In both panels (a and b1−3), the vertical axis ("normalization") means $R_{bb}^2 \times (D/10\ \mathrm{kpc})$ and $R_{in}^2 \cos i \times (D/10\ \mathrm{kpc})$, where $D = 5.2$ kpc is the source distance, respectively.

Table 5.3: The best-fit parameters of BC_d and DC_b for Obs-D3.

Model		BC_d	DC_b
`wabs`	N_H (10^{22}cm^{-2})	0.36 (fixed)	
Soft excess	type	BB	diskBB
	T_{bb}/T_{in} (keV)	$0.16^{+0.01}_{-0.02}$	0.28 ± 0.02
	R_{bb}/R_{in} (km)[a]	45^{+11}_{-8}	27 ± 4
`compPS`	seed	diskBB	BB
	T_{in}/T_{bb} (keV)	0.74 ± 0.03	0.52 ± 0.02
	R_{in}/R_{bb} (km)[a]	5 ± 1	10 ± 1
	T_e (keV)	68 ± 9	51 ± 5
	τ	$0.95^{+0.10}_{-0.09}$	$0.98^{+0.06}_{-0.05}$
	reflection ($\Omega/2\pi$)	0.8 ± 0.2	0.9 ± 0.2
`Gaussian`[b]	EW[c] (eV)	19^{+5}_{-1}	17^{+13}_{-9}
Fit goodness	$\chi^2_\nu(\nu)$	1.11 (363)	1.09 (363)
Luminosity	L_x (erg s^{-1})	3.64×10^{36}	3.57×10^{36}

[a]Assuming the inclination of 45° for diskBB, and the distance of 5.2 kpc for both BB and diskBB. The distance uncertainty is not included in the error. The value of R_{in} is corrected as equation 2.7.

[b]The centroid energy and width are fixed to 6.4 keV and 0.1 keV, respectively.

[c]Equivalent width.

In order to examine whether the model DC_b, which was found successful on Obs-D3, also applies to Obs-D2 and Obs-D4, we fit the two spectra with the model. As shown in figure 5.7 and table 5.4, the model has given acceptable fits to both Obs-D2 with χ^2/ν =1.15 (363) and Obs-D4 with χ^2/ν =1.16 (363). The parameters of the three observations, except for those of the corona (T_e and τ), are consistent within errors. Thus, we conclude that DC_b, a natural extension of the soft-state modeling, provides appropriate explanation of the hard-state spectra at $L_{abs} \sim 0.01 L_{edd}$, as long as Aql X-1 is concerned.

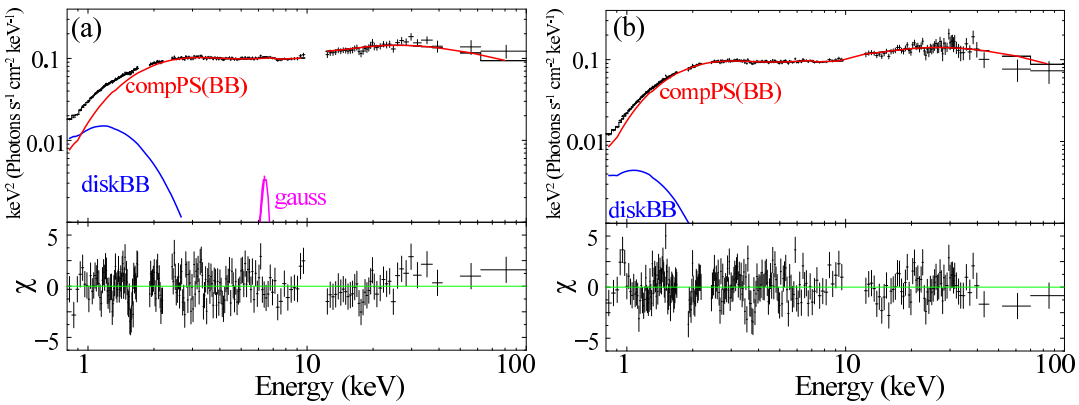

Figure 5.7: The spectra of Aql X-1 in the hard state, Obs-D2 (panel a) and Obs-D4 (panel b), both fitted with DC_b.

Table 5.4: Best-fit parameters of DC_b for Obs-D2 and Obs-D4.

Component	Paramater[a]	Obs-D2	Obs-D4
`wabs`	N_H (10^{22}cm^{-2})	0.36 (fixed)	
`diskBB`	T_{in} (keV)	0.28 ± 0.02	$0.28^{+0.07}_{-0.05}$
	R_{in} (km)[ab]	23^{+4}_{-3}	15^{+7}_{-5}
`compPS(BB)`	T_{bb} (keV)	0.53 ± 0.02	0.51 ± 0.02
	R_{bb} (km)[a]	9 ± 1	9 ± 1
	T_e (keV)	64 ± 6	64 ± 6
	τ	0.81 ± 0.04	0.81 ± 0.04
	reflection ($\Omega/2\pi$)	0.8 ± 0.3	$0.9^{+0.3}_{-0.2}$
`Gaussian`[c]	EW (eV)[d]	< 16	9^{+12}_{-8}
Fit goodness	$\chi^2_\nu(\nu)$	1.15 (363)	1.16 (363)
Luminosity	L_x (erg s^{-1})	3.07×10^{36}	2.75×10^{36}

[a]Assuming the distance of 5.2 kpc without propagating its error of 0.7 kpc.
[b]Assuming the source inclination of 45 degree.
[c]The centroid energy and width are fixed to 6.4 keV and 0.1 keV, respectively.
[d]Equivalent width.

5.1.4 The hard state with $L_{abs} \sim 0.001 L_{edd}$

We next proceed to Obs-D5, the data with $L_{abs} \sim 0.001 L_{edd}$, which is an order of magnitude lower than those of Obs-D2 to Obs-D4. The $\nu F\nu$ spectrum shown in figure 5.1 also has a power-law-like shape with $\Gamma \sim 2$ or a little harder, but exhibits a concave feature around ~ 4 keV. Figure 5.8 shows spectral ratios to the best-fit DC_b model of Obs-D3 obtained in §5.1.3.

In addition to the concaveness, the ratios reveal two more characteristic properties. One is the decrease softward of ~ 1.5 keV, suggestive of the disappearance or decrease of the soft excess. This, together with the concave structure, may be alternatively interpreted as the emergence of a hump at $1 - 3$ keV. The other is a slope change between $\lesssim 10$ keV and $\gtrsim 10$ keV. This suggests weakening of the reflection signature.

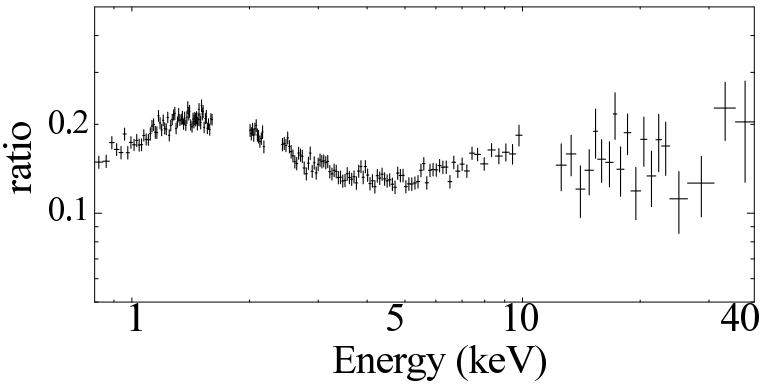

Figure 5.8: Ratios of the Obs-D5 spectrum to the best-fit model (DC_b) of Obs-D3.

Given the results in §5.1.3, we first examined the Obs-D5 spectrum with the same DC_b model without the reflection component. Although the fit, shown in figure 5.9, was acceptable with $\chi^2/\nu = 1.00(177)$, the disk component, weaker than the Comptonized BB by $\sim$ 1 order of magnitude, gave unreasonable parameters as $T_{\rm in} = 0.7^{+0.3}_{-0.4}$ keV $> T_{\rm bb} = 0.40^{+0.03}_{-0.01}$ and $R_{\rm in} < 6$ km. This is because the model tried to fit the $1-3$ keV hump with `diskBB`. Since the luminosity is very low, we had better consider that the disk emission became too soft to be detected.

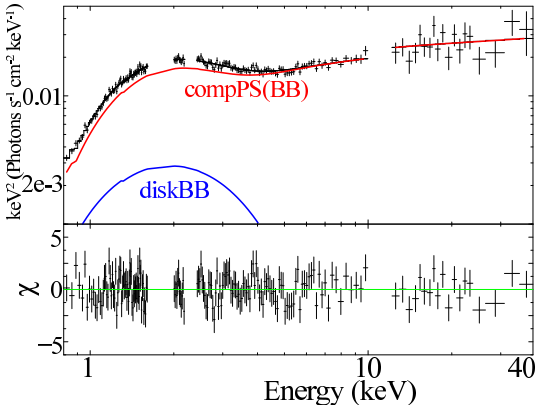

Figure 5.9: A spectral fit of Obs-D5 with the model DC_b without reflection component.

Since the `diskBB` component is thus unlikely to be needed any longer, we next applied the model C_b to the spectrum. As shown in figure 5.10 (a), it successfully reproduced the spectrum with $\chi^2/\nu = 1.05(179)$, and gave the parameters as listed in table 5.5. Importantly, $R_{\rm bb}$ has decreased to 7 ± 1 km (which itself is comparable to $R_{\rm in}$ in DC_b) from those of Obs-D2−D4 ($\sim$ 10 km). This can be roughly reconfirmed with the Stefan-Boltzmann law; the BB flux $F_{\rm bb}$, decreased to $\sim$ 20% of the previous (Obs-D2) value and $T_{\rm bb}$ did to $\sim$ 80%, so that $R_{\rm bb} \propto \sqrt{F_{\rm bb}/T_{\rm bb}^4}$ should become ~ 0.7 times the previous $R_{\rm bb} \sim 10$ km. In this fit, the $1-3$ keV hump is explained as "seen-through" fraction of the seed BB emission, and the rising hard tail in $\gtrsim 5$ keV as the genuine Comptonized

photons. This seen-through effect required a relatively low optical depth as $\tau = 0.42 \pm 0.02$, which is almost half of those in Obs-D2−4 ($\tau \sim 2$). This τ, together with the spectral slope at > 5 keV, made it possible to also constrain $T_{\rm e} = 150 \pm 10$ keV, even though the spectrum does not exhibit clear high-energy cutoff. Actually, as shown in figure 5.11 (a) in the form of $T_{\rm e}$ vs τ confidence contours, the two parameters are very well constrained. This is thanks to the broad-band sensitivity of *Suzaku*.

The successful fit of $\rm C_b$ with a low τ inspires us with another possibility. While the $\rm C_b$ fit assumes that the entire BB source is covered by the Comptonizing corona, BB can be only partially covered; then, the $1 - 3$ keV hump can be interpreted as the directly visible part of BB, and the > 5 keV hard tail as the remaining fraction which experienced Comptonization. We hence fitted the same spectrum with a raw BB plus its Comptonization, hereafter called $\rm BC_b$ model (table 5.1). As shown in figure 5.10 (b), this alternative model is also successful with $\chi^2/\nu = 1.03(178)$. The parameters are shown in table 5.5. Thus, the fraction of directly-visible component is $\sim 50\%$, and the remaining half is Comptonized by a corona, which is rather optically thick ($\tau \sim 2$) to suppress the seen-through effect, and somewhat cooler ($T_{\rm e} \sim 40$ keV) to reproduce the hard-tail slope under a larger value of τ. The data can now provide only a lower limit on τ and an upper limit on $T_{\rm e}$, because they are strongly (anti-)correlated as represented by the confidence contours in figure 5.11 (b)−(d). This is because the model attains a freedom of expressing the soft hump either entirely as the naked BB (with a larger τ and low $T_{\rm e}$), or partially as seen-through seed photons (a small τ and a high $T_{\rm e}$). The data can only constrain $y = 0.7 \pm 0.1$ from the slope. Nevertheless, the total BB emission radius has remained unchanged as $\sqrt{5^2 + 5^2} \sim 7$ km (sum of the directly-visible and Comptonized areas).

Thus, we have confirmed that the spectrum in Obs-D5 with $L_{\rm abs} \sim 0.001 L_{\rm edd}$ is reproduced by a Comptonized BB emission, and within the modeling ambiguity, either the whole BB emission is Comptonized by a high-$T_{\rm e}$ and low-τ corona ($\rm C_b$), or only a fraction of BB is covered with a low-$T_{\rm e}$ and high-τ corona ($\rm BC_b$). The truth may lie in between the two. In order to distinguish them, we need to know precisely the cut-off energy present in $\gtrsim 50$ keV.

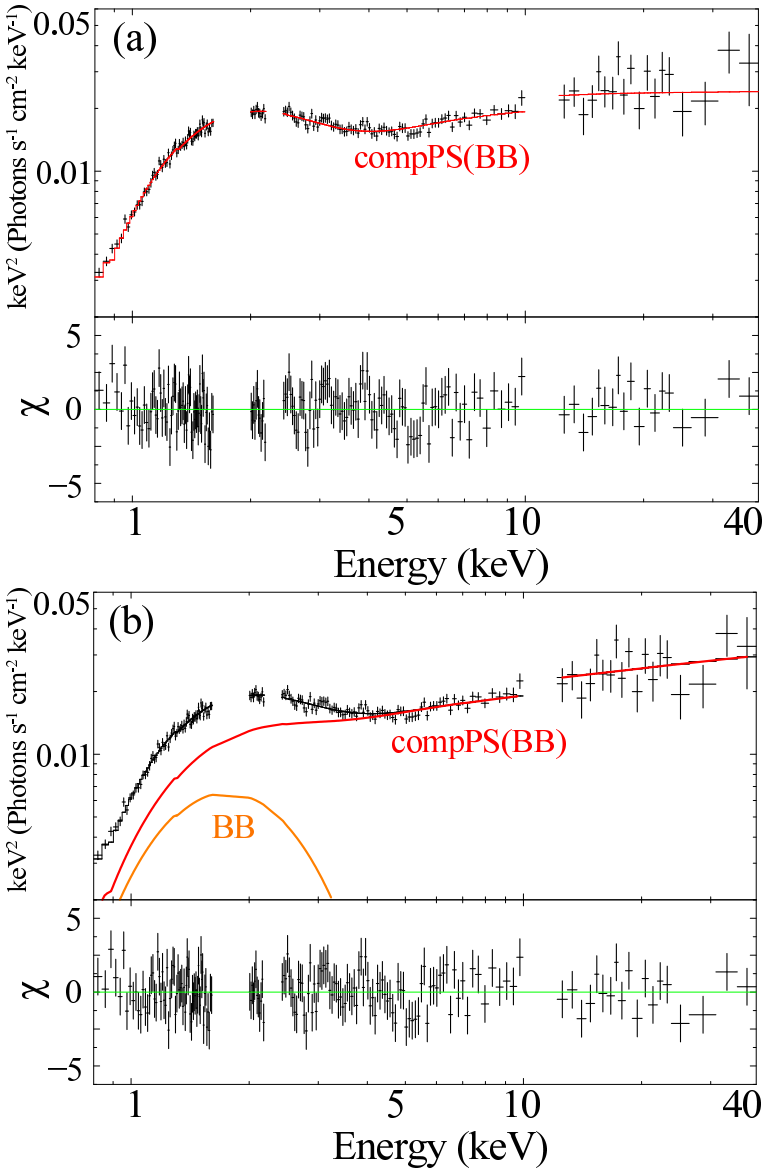

Figure 5.10: Spectral fits to Obs-D5 with models C_b (panel a) and BC_b (panel b).

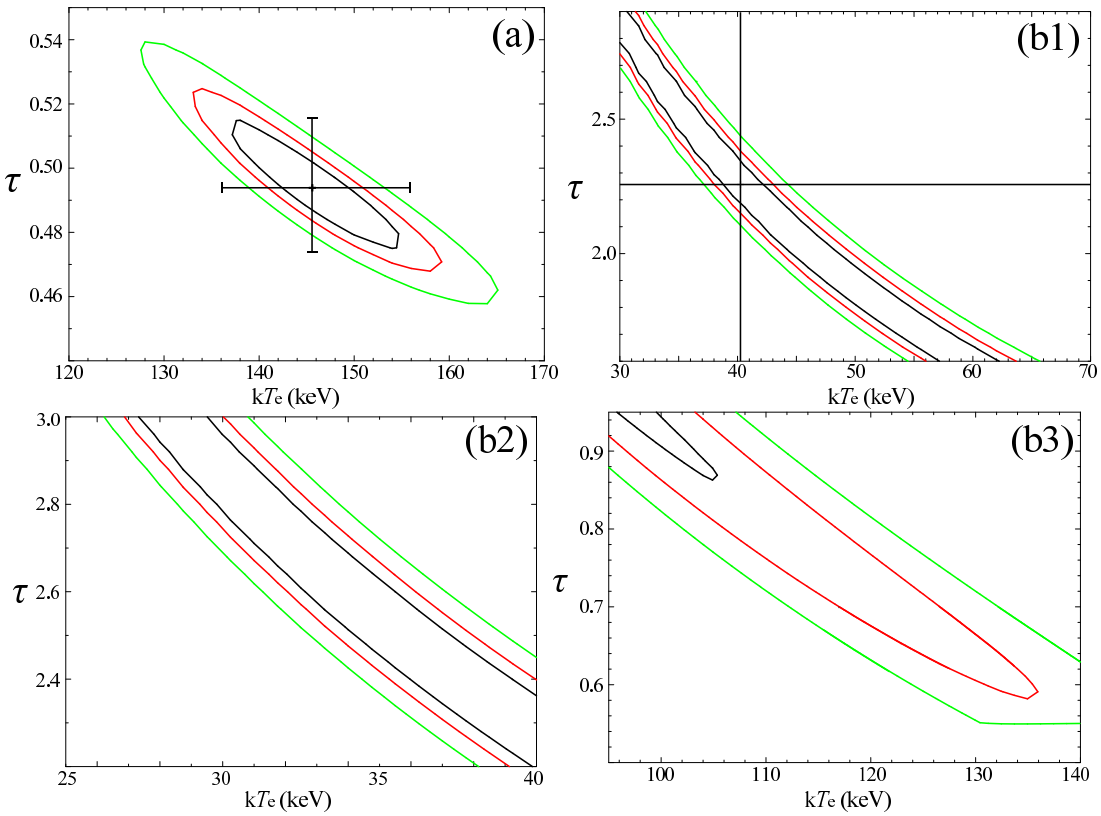

Figure 5.11: Confidence contours of the C_b (panel a) and the BC_b (panels b, c, and d) fits to the Obs-D5 spectrum, expressed on the plane of T_e vs τ. Panels (b1)−(b3) are separated for the same technical reasons as figure 5.6. The best-fit values are listed in table 5.5, and those of (T_e, τ) are shown in a cross (corresponding to $\Delta\chi^2 = 2.7$).

Table 5.5: Model parameters of C_b and BC_b for Obs-D5.

Component	Paramater	C_b	BC_b
`wabs`	N_H (10^{22}cm^{-2})	0.36 (fixed)	
`bbody`	T_{bb} (keV)	-	0.39 ± 0.01
	R_{bb} (km)[a]	-	5^{+1}_{-2}
`compPS(BB)`	T_{bb} (keV)	0.40 ± 0.01	-
	R_{bb} (km)[a]	7 ± 1	5 ± 1
	T_e (keV)	146 ± 10	$\lesssim 110$
	τ	0.49 ± 0.02	$\gtrsim 0.8$
	y	0.56 ± 0.02	0.7 ± 0.1
Fit goodness	$\chi^2_\nu(\nu)$	1.05 (179)	1.03 (178)
Luminosity	L_x (erg s^{-1})	6.48×10^{35}	6.90×10^{35}

[a] Assuming the distance of 5.2 kpc without propagating its error of 0.7 kpc.

5.1.5 The hard state with $L_{abs} \sim 10^{-4} L_{edd}$

As shown in figure 5.1, the spectra in Obs-D6 and Obs-D7 , when the luminosity became still lower as $L_{abs} \sim 10^{-4} L_{edd}$, have similar characteristics to those of Obs-D5 (§5.1.4). The source was too dim on this occasion to detect in the hard band of > 10 keV with the HXD. The concave feature became clearer, and appears to have moved from ~ 4 keV to ~ 3 keV. In addition, the soft-hump peak has shifted from ~ 2 keV to ~ 1.5 keV. These suggest that the spectra are also produced by a Comptonized BB, possibly with lower T_{bb}.

With the above inference in mind, we fitted the dimmest two spectra with the models C_b and BC_b, like in §5.1.4, and obtained the results shown in figure 5.12. In both observations, either model was able to reproduce the spectrum, just the same as the Obs-D5 result. The parameters shown in table 5.6 imply that the BB emission area on the NS further decreased, as either model gave the same $R_{bb} \sim 3$ km in total for both spectra. The optical depth in BC_b was only constrained on the lower side, because τ reached 3.0, the model validity limit, before the 90%-confidence limit was found. The best-fit value, 1.6 (Obs-D6) and 2.6 (Obs-D7) is still within the model limit, and hence can be considered reliable. The slight spectral change from Obs-D6 to Obs-D7, a hardening in > 3 keV range, means an increase of the Compton y-parameter (§2.3). It is reflected in the increase of T_e. In the C_b fit, this is because the more prominent concaveness requires a lower τ, which must be compensated by a higher value of T_e to reproduce the spectral slope in > 4 keV.

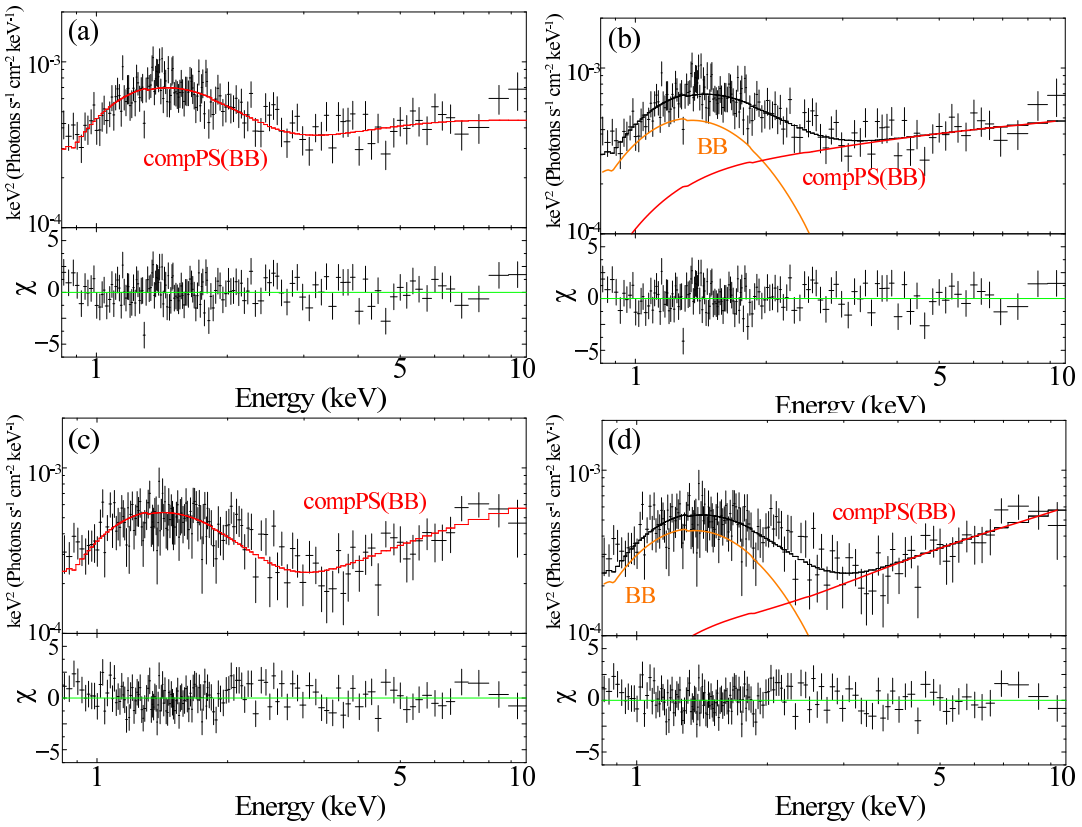

Figure 5.12: Spectral fits of AqlX-1 in the very dim hard state, Obs-D6 (panels a and b) and Obs-D7 (panels c and d), with models C_b (left panels) and BC_b (right panels).

Table 5.6: Best-fit model parameters of C_b and BC_b for Obs-D6 and Obs-D7.

		Obs-D6		Obs-D7	
Component	Paramater	C_b	BC_b	C_b	BC_b
`wabs`	N_H (10^{22}cm^{-2})	0.36 (fixed)			
`bbody`	T_{bb} (keV)	-	0.27 ± 0.01	-	0.27 ± 0.02
	R_{bb} (km)[a]	-	< 3	-	< 3
`compPS(BB)`	T_{bb} (keV)	0.27 ± 0.01	-	0.27 ± 0.01	-
	R_{bb} (km)[a]	3 ± 1	2 ± 1	3 ± 1	2 ± 1
	T_e (keV)	170^{+50}_{-40}	$60(\lesssim 220)$	400^{+250}_{-130}	$110(\lesssim 600)$
	τ	$0.19^{+0.04}_{-0.03}$	$1.6(> 0.2)$	$0.16^{+0.03}_{-0.02}$	$2.6(> 0.2)$
	y	$0.29^{+0.05}_{-0.03}$	$0.8^{+0.3}_{-0.5}$	$0.5^{+0.5}_{-0.2}$	$\gtrsim 0.5$
Fit goodness	$\chi^2_\nu(\nu)$	0.94 (134)	0.94 (133)	0.81 (134)	0.81 (133)
Luminosity	L_x (erg s^{-1})	1.63×10^{34}	1.62×10^{34}	3.34×10^{34}	1.61×10^{34}

[a]Assuming the distance of 5.2 kpc without propagating its error of 0.7 kpc.

5.2 Hard-State Sources with $L_{\rm abs} \lesssim 0.01 L_{\rm edd}$

In §5.1, we have found a spectral model which can explain the Aql X-1 spectra in the hard state with $L_{\rm abs} \leq 0.01 L_{\rm edd}$. The next task is to examine whether the same model can explain other LMXB spectra at similar luminosities. For that purpose, 5 data sets were chosen from our sample.

5.2.1 4U 1608-52

As described in §4.4.1, spectral variations were observed from 4U1608-52 (404044030). We therefore divide the data into the three intervals, I_1, I_2, and I_3, as in figure 4.7, and analyze them separately. The derived spectra are shown in figure 5.13. As expected from the light curves in figure 4.7, the three spectra reveal a slope change with a pivot at $10 - 15$ keV. Compared to the Aql X-1 spectra in Obs-D2 to D4, the spectra exhibit cutoff at lower energies as $\lesssim 20$ keV, and hence look somewhat close to those of the soft state.

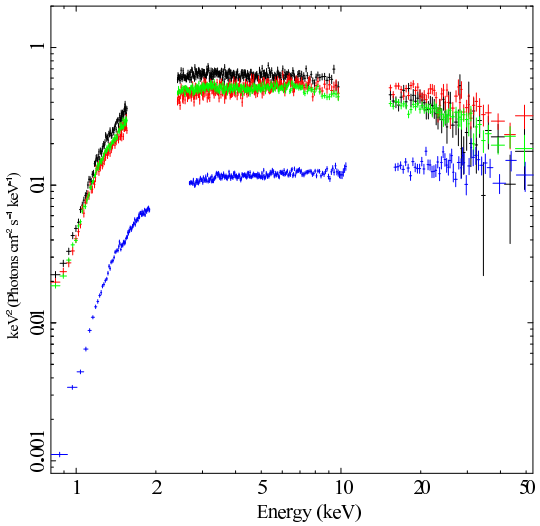

Figure 5.13: The $\nu F\nu$ spectra of 4U1608-52 (404044030 and 404044040), I_1 (black), I_2 (red), I_3 (green), and 404044040 (blue), where the former three intervals are defined in figure 4.7 (§4.4.1).

Since the $0.8 - 100$ keV absorbed luminosity $L_{\rm abs} \sim 0.02 L_{\rm edd}$ is similar to those of Aql X-1 in §5.1.3, we expect that the spectra of I_1, I_2, and I_3 are also composed of the directly-visible disk and the Comptonized BB emission. In fact, as shown in figure 5.14, all the spectra were successfully reproduced by the DC_b model, and yielded the parameters as listed in table 5.7. Since the derived $T_e \gtrsim 20$ keV is higher than that of the soft state (§5.1.2) by an order of magnitude, this source is confirmed to be still in the hard state according to the classification in §4.1.2.

The spectral changes among I_1, I_2, and I_3 are mainly carried by Γ. Since the other parameters including T_e are consistent with being the same within errors, the difference is possibly due to the change of coronal optical depth, namely, a decrease of τ (equation 5.4) in I_2. Associated with this decrease of τ, T_{bb} and R_{bb} slightly became lower and larger, respectively. These suggest a temporal spread of the flow onto the NS.

While the coronal parameters indicate that the source was still in the hard state, the temperatures of the optically-thick components ($T_{in} \sim 0.6$ keV and $T_{bb} \sim 1.0$) are closer to those of the soft-state Aql X-1 ($T_{in} \sim 0.7$ and $T_{bb} \sim 1.2$) than its hard state ($T_{in} \sim 0.3$ and $T_{bb} \sim 0.5$). Therefore, the behavior of the optically-thick components may be rather continuous across the state boundary.

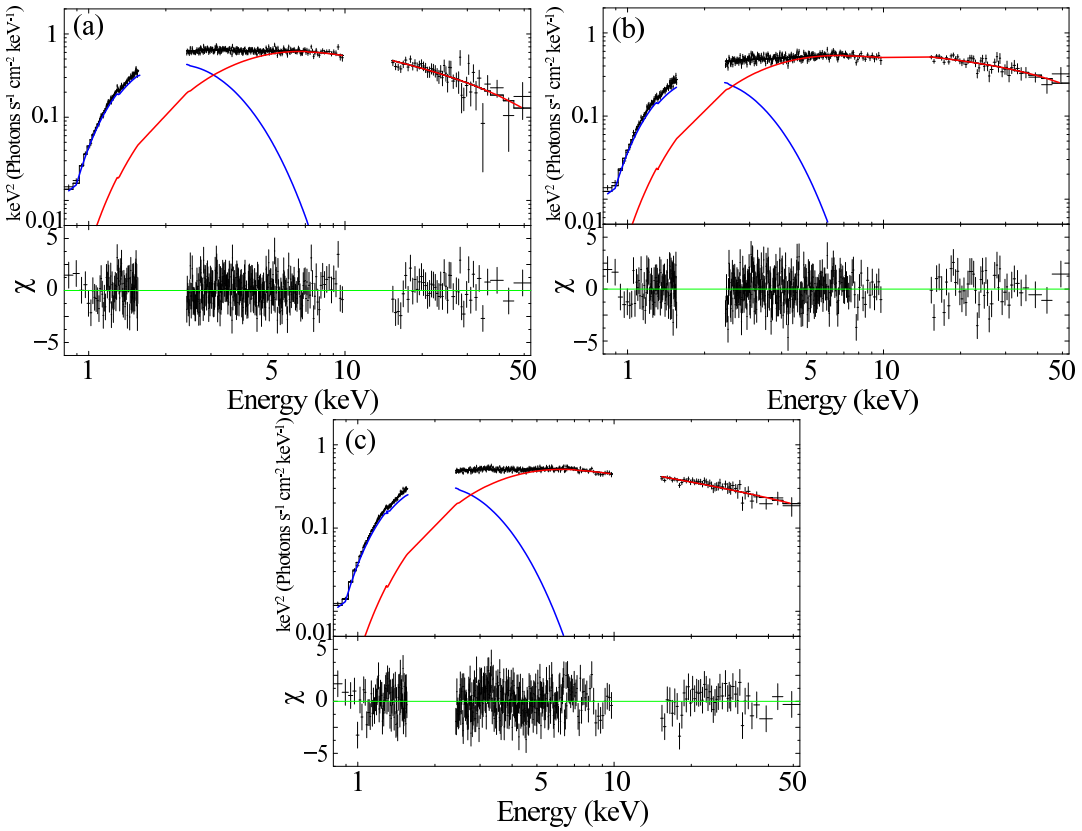

Figure 5.14: Spectral fits to 4U1608-52 (404044030) with DC_b, in I_1 (panel a), I_2 (panel b), and I_3 (panel c).

Table 5.7: Best-fit DC_b parameters of 4U1608-52 (404044030) in the three intervals with DC_b.

Component	Paramater	I_1	I_2	I_3
`wabs`	N_H (10^{22}cm^{-2})	1.14 ± 0.03	1.10 ± 0.04	1.14 ± 0.02
`diskBB`	T_{in} (keV)	0.62 ± 0.03	$0.55^{+0.03}_{-0.04}$	0.57 ± 0.02
	R_{in} (km)[ab]	14 ± 1	16 ± 1	16 ± 1
`nthcomp(BB)`	T_{bb} (keV)	1.1 ± 0.1	0.9 ± 0.1	$1.00^{+0.04}_{-0.05}$
	R_{bb} (km)[a]	3 ± 1	4 ± 1	4 ± 1
	T_e (keV)	$19(>10)$	22^{+78}_{-8}	>40
	Γ	2.5 ± 0.2	$2.22^{+0.08}_{-0.06}$	$2.49^{+0.03}_{-0.07}$
	τ	$2.3(<3.1)$	$2.5^{+0.8}_{-1.7}$	<1.3
Fit goodness	$\chi^2_\nu(\nu)$	1.01 (376)	1.24 (376)	1.17 (376)
Luminosity[d]	L_x (erg s^{-1})	7.33×10^{36}	6.47×10^{36}	6.54×10^{36}

[a]Assuming the distance of 3.6 kpc without propagating its uncertainty.
[b]Assuming the source inclination of 45 degree.

The other hard-state spectrum of 4U1608-52 (404044040), taken 4 days after those above (404044030), is shown in figure 5.13 (in blue). From the previous ones, it became $\sim$ 1 order of magnitude fainter, and has a very flat shape with $\Gamma \sim 2$. As shown in figure 5.15, the spectrum on this occasion was also successfully reproduced by DC_b . The best-fit parameters listed in table 5.8 are quite similar to those of Obs-D2 to D4 of Aql X-1, and are actually consistent within errors.

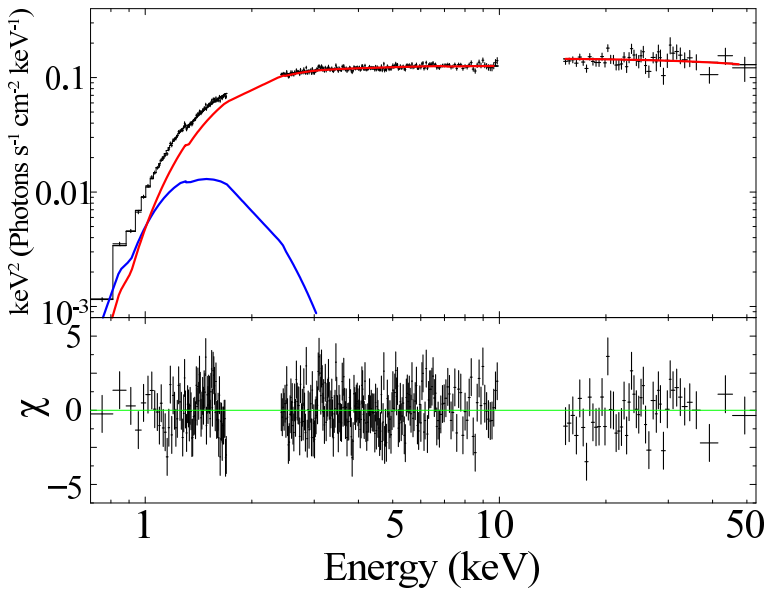

Figure 5.15: A spectral fit of 4U1608-52 (404044040) with model DC_b.

Table 5.8: The best-fit parameters of 4U1608-52 (404044040) spectrum with model DC_b.

Component	Paramater	Value
wabs	N_H ($10^{22}cm^{-2}$)	1.1 ± 0.1
diskBB	T_{in} (keV)	$0.32^{+0.1}_{-0.06}$
	R_{in} (km)[ab]	17^{+13}_{-7}
`compPS(BB)`	T_{bb} (keV)	$0.47^{+0.07}_{-0.04}$
	R_{bb} (km)[a]	8^{+1}_{-2}
	T_e (keV)	54^{+8}_{13}
	τ	$1.0^{+0.3}_{-0.1}$
Fit goodness	$\chi^2_\nu(\nu)$	1.20 (331)
Luminosity	L_x (erg s^{-1})	1.84×10^{36}

[a]Assuming the distance of 3.6 kpc without propagating its uncertainty.
[b]Assuming the source inclination of 45 degree.

5.2.2 4U1636-536

Following the successful application of DC_b to 4U1608-52, we next examined 4U1636-536, of which one observation among the five caught its hard state (§4.1.2). Assuming a distance of 5.9 kpc, The luminosity on this occasion was $L_{abs} \sim 0.04 L_{edd}$ which is between $0.01 L_{edd}$ and $0.1 L_{edd}$.

The spectrum in figure 5.16 can make it easy to constrain `diskBB` component (if present), because the interstellar absorption of this source is relatively small as $N_H \lesssim 0.3 \times 10^{22}$ cm^{-2} (Fiocchi et al. 2006; Lyu et al. 2014). We examined whether the spectrum is also reproduced by DC_b. As shown there, our expectation was realized indeed, with parameters listed in table 5.9. The result agrees with that of 4U 1608-52 in the brighter phase (404044030: §5.2.1), because the parameters are almost consistent within errors except for the slightly larger $R_{bb} \sim 6$ km.

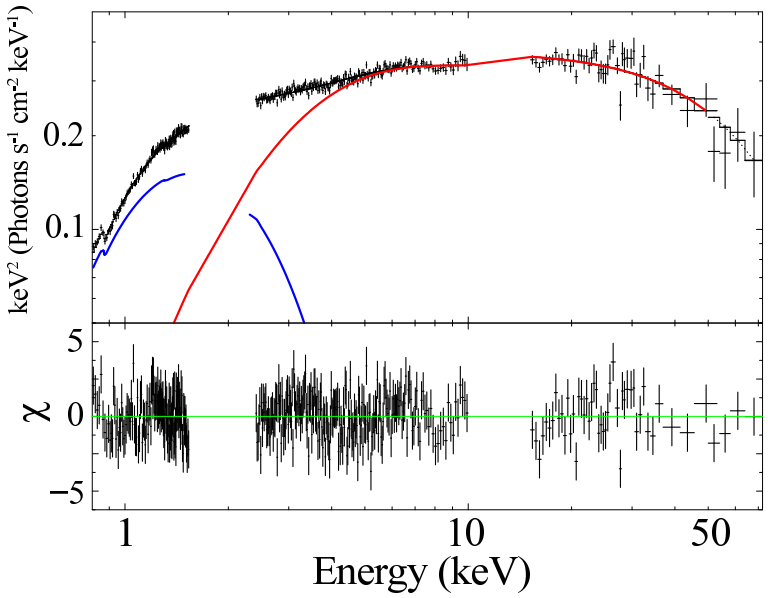

Figure 5.16: A spectral fit to 4U1636-536 (401050010) with DC_b.

Table 5.9: The best-fit parameters of 4U1636-536 (401050010) spectrum with DC_b.

Component	Paramater	Value
wabs	N_H (10^{22}cm^{-2})	0.19 ± 0.01
diskBB	T_{in} (keV)	0.55 ± 0.02
	R_{in} (km)[ab]	14 ± 1
`nthcomp`(BB)	T_{bb} (keV)	0.86 ± 0.05
	R_{bb} (km)[a]	6 ± 1
	T_e (keV)	20^{+5}_{-3}
	Γ	2.00 ± 0.02
	τ	$3.2^{+0.4}_{-0.3}$
Fit goodness	$\chi^2_\nu(\nu)$	1.15 (380)
Luminosity	L_x (erg s^{-1})	9.71×10^{36}

[a]Assuming the distance of 3.6 kpc without propagating its uncertainty.
[b]Assuming the source inclination of 45 degree.

5.2.3 4U 1812-12

The persistent source 4U1812-12 yielded the spectrum shown in figure 5.17, when its $0.8-100$ keV absorbed luminosity was 1.4×10^{36} erg s^{-1} $\sim 0.01 L_{edd}$. The hard spectrum extending above $\gtrsim 50$ keV is consistent with those previously observed from this soruce with other instruments (Barret et al. 2003b; Tarana et al. 2006).

Given the successful reproduction of the spectra of Aql X-1 and 4U1608-52, and 4U1636-536, we expect that the DC_b model also applies to this source. As shown in

figure 5.17, the fit with DC_b was indeed successful with $\chi^2/\nu = 1.13(331)$, and gave the parameters as listed in table 5.10. The unabsorbed luminosity $L_x = 2.9 \times 10^{36}$ erg s^{-1} is almost the same as that of Aql X-1 in Obs-D3 (§5.1.3). Moreover, like the previous 4U1608-52 (404044040), the parameters of the optically-thick components, T_{in}, R_{in}, T_{bb}, and R_{bb}, are all consistent within errors between this source and Obs-D3. The slightly larger R_{in} could be attributed to uncertainties in i. The difference is present in the Comptonization parameters. The electron temperature $T_e = 83^{+8}_{-9}$ keV is significantly higher than that of Obs-D3 ($T_e \sim 50$ keV), while $\tau = 0.80^{+0.1}_{-0.08}$ is smaller by $\sim 20\%$, resulting in the same $y \propto T_e\tau^2 \sim 1.6 \times 0.8^2 \sim 1$. This result, together with those of 4U1608-52 (§5.2.1) and 4U1636-536 (§5.2.2), strengthens the general applicability of DC_b to the spectra of hard-state LMXBs at $L_{abs} \sim 0.01 L_{edd}$.

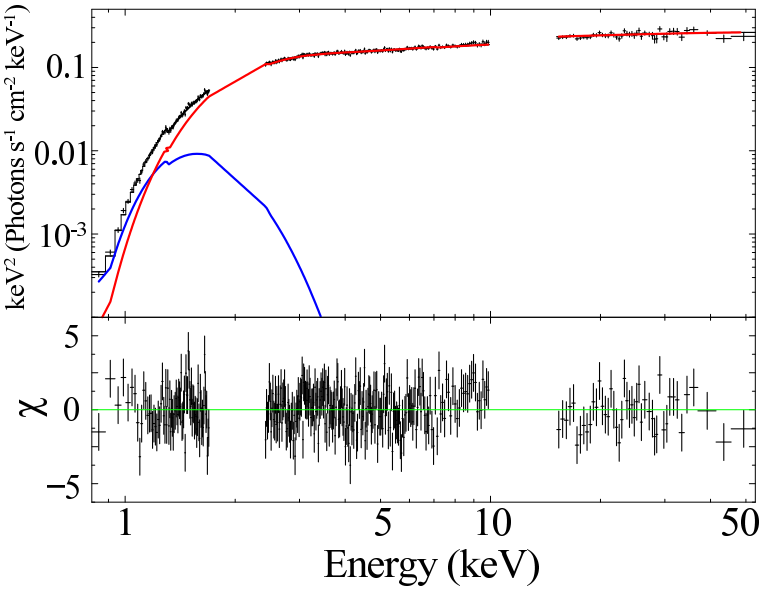

Figure 5.17: The $\nu F\nu$ spectrum of 4U1812-12 (406008010), fitted with DC_b .

Table 5.10: Best-fit parameters of DC_b for 4U 1812-12 (406008010).

Component	Paramater	
`wabs`	N_H (10^{22}cm^{-2})	2.0 ± 0.2
`diskBB`	T_{in} (keV)	$0.24^{+0.05}_{-0.03}$
	R_{in} (km)[ab]	50^{+40}_{-30}
`compPS(BB)`	T_{bb} (keV)	0.51 ± 0.02
	R_{bb} (km)[a]	10 ± 1
	T_e (keV)	83^{+8}_{-9}
	τ	$0.80^{+0.1}_{-0.08}$
Fit goodness	$\chi^2_\nu(\nu)$	1.13 (331)
Luminosity	L_x (erg s^{-1})	4.63×10^{36}

[a]Assuming the distance of 4 kpc.
[b]Assuming the source inclination of 45 degree.

5.2.4 SLX 1737-282

The three sources analyzed above, 4U1608-52, 4U1636-536 and 4U1812-12, had a luminosity of $L_{\rm abs} = (0.01 - 0.04)L_{\rm edd}$, which is close to or slightly higher than those of Obs-D2, Obs-D3, and Obs-D4 of Aql X-1. This source SLX 1737-282, in turn, had $L_{\rm abs} = 0.003L_{\rm edd}$ which is similar to that of Obs-D5 of Aql X-1. Following the remark made in §4.4.7, below we analyze its spectrum in the calm phase, excluding the flares.

Since the spectral shape in figure 5.18 is not as concave as those of Obs-D5, we first tried $\rm DC_b$ model which was successful in the $L_{\rm abs} \sim 0.01L_{\rm edd}$ sources. Although the spectrum was well reproduced with $\chi^2/\nu = 1.05(351)$, the model gave unreasonable disk inner radius as $R_{\rm in} \sim 2$ km. We hence removed the disk component, and tried $\rm C_b$ and $\rm BC_b$ models as we did in §5.1.4 and §5.1.5. As shown in figure 5.18, either modeling was able to reproduce the spectrum, with the parameters listed in table 5.11. The result is qualitatively consistent with that of Obs-D5 of Aql X-1, that is, the total $R_{\rm bb} \sim 4$ km is significantly smaller than 10 km and the Comptonizing corona has a high temperature as $T_{\rm e} > 30$ keV. Quantitatively, the obtained $T_{\rm bb} \sim 0.5$ keV is higher and $R_{\rm bb}$ is smaller than those of Obs-D5 (~ 0.4 keV and ~ 7 km, respectively). The less prominent concaveness of this source is reflected in a somewhat larger τ.

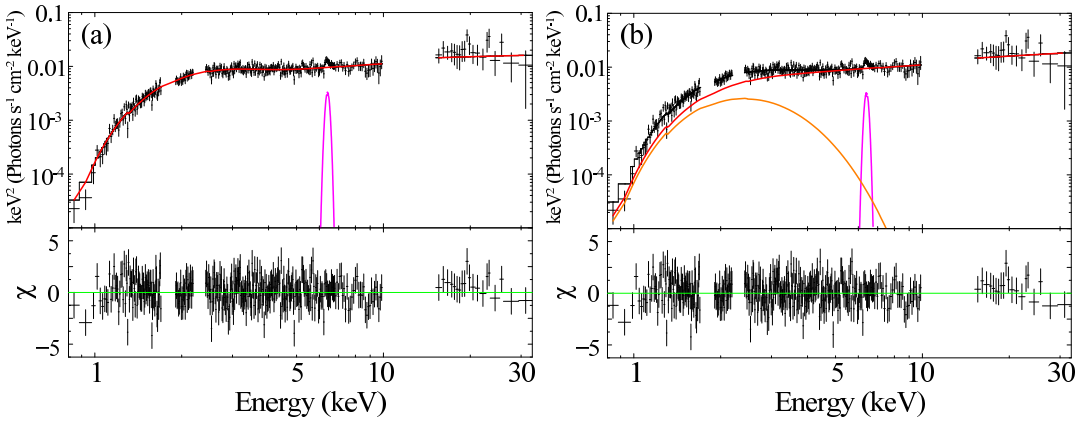

Figure 5.18: Spectral fits to SLX1737-282 (503103010) with model $\rm C_b$ (panel a) and $\rm BC_b$ (panel b). The directly-visible and Comptonized BB are shown in red and orange, respectively.

Table 5.11: Model parameters of C_b and BC_b for SLX 1737-282 (503103010).

Component	Paramater	C_b	BC_b
`wabs`	N_H (10^{22}cm^{-2})	1.4 ± 0.1	1.4 ± 0.1
`bbody`	T_{bb} (keV)	-	0.49 ± 0.04
	R_{bb} (km)[a]	-	< 3
`compPS(BB)`	T_{bb} (keV)	0.50 ± 0.04	-
	R_{bb} (km)[a]	4 ± 1	3 ± 1
	T_e (keV)	140 ± 30	60^{+90}_{-30}
	τ	$0.52^{+0.07}_{-0.05}$	$1.6(> 0.6)$
`Gaussian`[b]	EW (eV)[c]	90^{+60}_{-40}	90^{+430}_{-30}
Fit goodness	$\chi^2_\nu(\nu)$	1.02 (352)	1.02 (351)
Luminosity	L_x (erg s^{-1})	6.14×10^{35}	6.32×10^{35}

[a] Assuming the distance of 6.5 kpc without propagating its error of 1.5 kpc.

[b] The centroid energy and width are fixed to 6.4 keV and 0.1 keV, respectively.

[c] Equivalent width.

5.2.5 Cen X-4

As described in §4.4.5, the luminosity of Cen X-4 (403057010) was extremely low as $L_{abs} = 5.1 \times 10^{31}$ erg s^{-1} , which is by far the lowest among our all LMXB sample data sets, and ~ 2 orders of magnitude lower than the second-dimmest one, Obs-D6 of Aql X-1. The concave spectrum shown in figure 5.19 reminds us of those of Obs-D6 and Obs-D7 (§5.1.5).

From the spectral shape, it is expected to be the same case as §5.1.5. We hence consider that the soft hump is from a low-temperature BB emission, either seen through a relatively thin corona (modeled with C_b), or uncovered by a thicker corona (BC_b). Indeed, as shown in figure 5.19, the spectrum was reproduced by either modeling. The value of N_H of the interstellar absorption was fixed to 0.05×10^{22} cm^{-2} obtained by Cackett et al. (2010). Although the coronal parameters (especially T_e) were poorly constrained, it is extremely high, and τ in the C_b modeling is even smaller than those of the dimmest Aql X-1 data. Furthermore, we again notice that the total BB radius, $R_{bb} \sim 0.5$ km, is significantly smaller than 10 km.

Thus. we have confirmed that the spectra of the sources with $L_{abs} \lesssim 0.001 L_{edd}$ are successfully reproduced in a unified way by a Comptonized BB emission with $R_{bb} < 10$ km, although the ambiguity of coronal covering fraction remains.

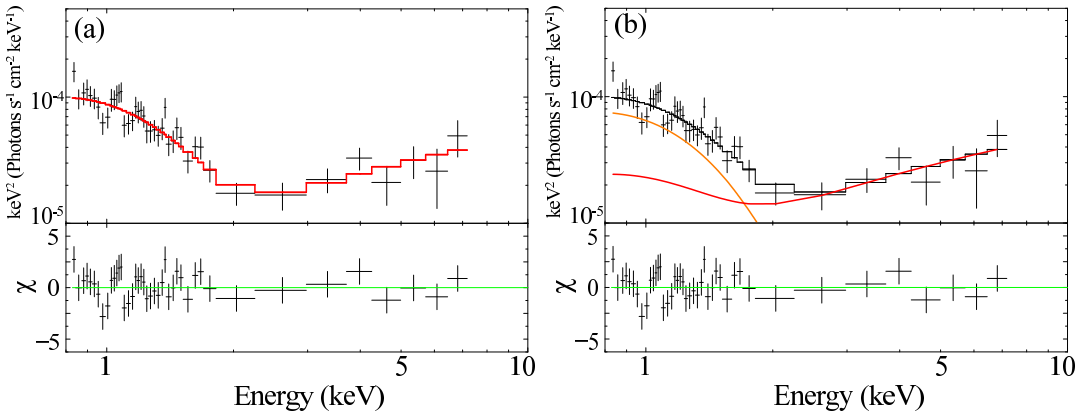

Figure 5.19: Fits to the Cen X-4 (403057010) spectrum with model C_b (panel a) and BC_b (panel b).

Table 5.12: The best-fit C_b and BC_b parameters for CenX-4 (403057010).

Component	Paramater	C_b	BC_b
`wabs`	N_H (10^{22}cm^{-2})	0.05 (fixed)	
`bbody`	T_{bb} (keV)	-	$0.19^{+0.01}_{-0.02}$
	R_{bb} (km)[a]	-	< 0.7
`compPS(BB)`	T_{bb} (keV)	0.19 ± 0.01	-
	R_{bb} (km)[a]	0.5 ± 0.2	$0.2 - 0.7$
	T_e (keV)	400^{+700}_{-200}	210^{+750}_{-180}
	τ	$0.11^{+0.07}_{-0.02}$	$1.5(> 0.06)$
Fit goodness	$\chi^2_\nu(\nu)$	1.14 (39)	1.14 (38)
Luminosity	L_x (erg s^{-1})	1.08×10^{32}	6.54×10^{32}

[a]Assuming the distance of 1.2 kpc without propagating its error.

5.3 Aql X-1: Rising Phase

5.3.1 Overview

On the rising phase of the outburst in 2011, Aql X-1 became as luminous as $L_{\rm abs} \gtrsim 0.1 L_{\rm edd}$ while remaining still in the hard state (§4.1.2). In order to have a glance at the spectral change along the luminosity, we draw in figure 5.20 spectra of Obs-R1, Obs-R2, and Obs-R3. Since Obs-R2 is considered to have been in the midst of a transitional phase (§4.3.2), those of the first $\sim$ 5 ks and the last $\sim$ 5 ks are shown in figure 4.6 as representatives. Thus, the luminosity in the rising phase, at least in Obs-R2 and Obs-R3, exceeds that of the soft-state Obs-D1 in the decaying phase. This is a manifestation of the hysteresis effect mentioned in §4.1.1 and §4.3.2. The cutoff energy clearly decreases as $L_{\rm abs}$ increases, from Obs-R1 ($\sim$ 30 keV: close to that of Obs-D3) to Obs-R3 ($\lesssim$ 10 keV). At the same time, the soft-band flux in $0.8 - 10$ keV increases by $\sim$ 1 order of magnitude. Below, we analyze these spectra in the rising order of $L_{\rm abs}$, namely from Obs-R1 to Obs-R3.

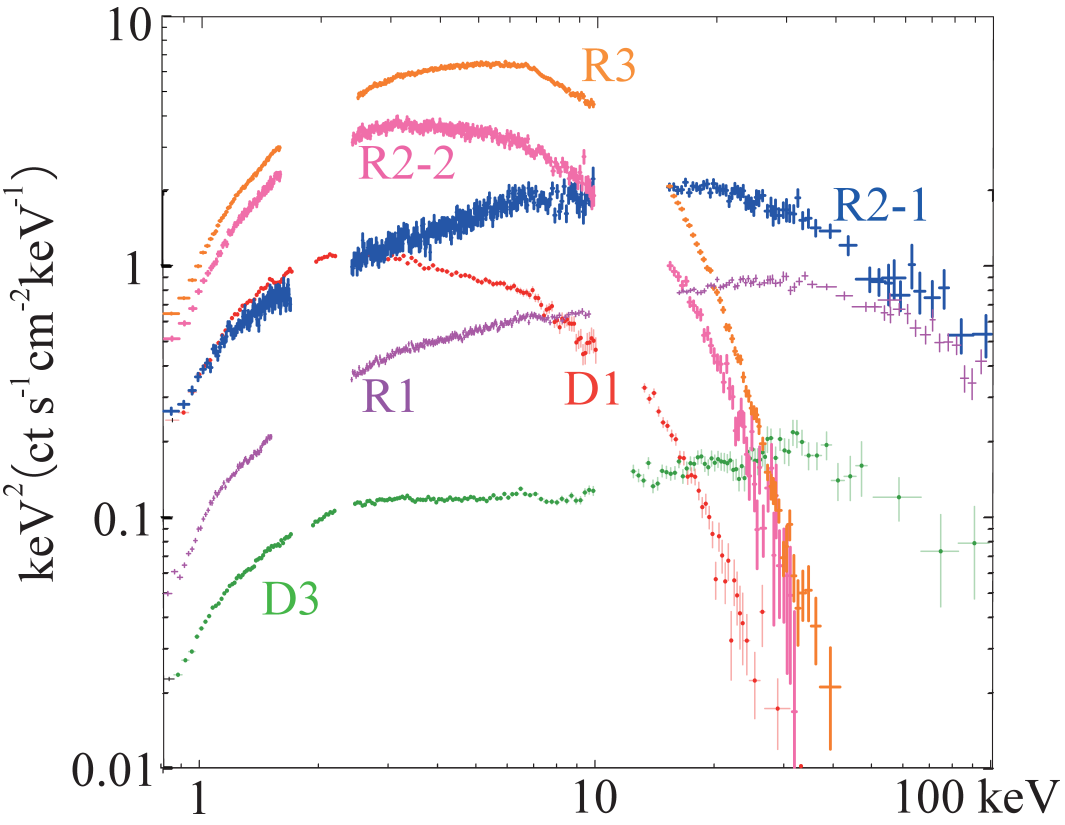

Figure 5.20: Background-subtracted *Suzaku* $\nu F\nu$ spectra of Aql X-1, obtained during a rising phase of the outburst in 2011 (§4.3.2). The purple, dark blue, magenta, and orange denote the spectra of Obs-R1, first 5 ks of Obs-R2, last 5 ks of Obs-R2, and Obs-R3, respectively. The other two correspond to those of Obs-D1 (red) and Obs-D3 (green) in figure 5.1.

5.3.2 The hard state with $L_{\rm abs} \sim 0.1 L_{\rm edd}$

Among the three observations, we begin with a time-averaged spectrum of Obs-R1 when the time variation was not significant (§4.3.2). The Obs-R1 spectrum in figure 5.20 is so similar to the Obs-D3 spectrum that we may first examine whether it has.the same shape with a higher flux (i.e. scalable). Figure 5.21 shows ratios of the Obs-R1 spectrum to the best-fit $\rm DC_b$ model of Obs-D3 (§5.1.3) without reflection component. We can extract three qualitative characteristics from the ratios. One is that the flux has increased, over the whole $0.8 - 100$ keV band, by a factor of > 2. Second, the ratio increases with energy in $3 - 30$ keV, which suggests a decrease (hardening) of Γ, namely an increase of the y-parameter. The third is that the ratio decreases in > 30 keV, indicating that the cut-off $T_{\rm e}$ is lower than that in Obs-D3 (35 ± 5 keV). Combining the latter two, namely the larger y and the lower $T_{\rm e}$, the optical depth τ should be larger than the Obs-D3 value (~ 3).

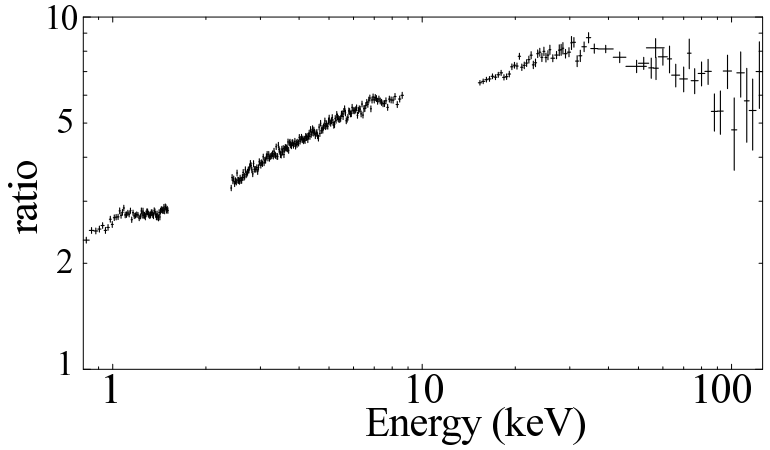

Figure 5.21: Ratios of the Obs-R1 spectrum to the best-fit $\rm DC_b$ model of Obs-D3 without reflection component.

From the hard-state results in the outburst decaying phase (§5.1) and above inferences, we try, as our first-cut attempt, the $\rm DC_b$ model on the bright hard state data of Obs-R1with $L_{\rm abs} \sim 0.1 L_{\rm edd}$. Since $L_{\rm abs}$ is high and the exposure is so long as > 30 ks (table 4.1), a systematic error of 1% is incorporated in the spectral fits hereafter. As shown in figure 5.22 (a), the model has roughly reproduced the spectrum, but gave unacceptable fit goodness of $\chi^2/\nu = 1.58(332)$. This is mainly caused by two positive residuals at ~ 1 keV and $6 - 7$ keV. These are considered to be $\rm K_\alpha$ lines from ionized and/or neutral ionic species; the former corresponds to Ne (0.85 keV), Ne IX (0.9 keV), and Ne X (1.02 keV), and the latter Fe (6.4 keV), Fe XXV (6.65 keV), and Fe XXVI (6.95 keV). We hence incorporated two gaussian lines into the model, of which the centroid energies are fixed to 1.0 keV and 6.6 keV, respectively, and the widths are allowed to vary so as to represent the sum of the multiple ionized states. As shown in 5.22 (b),

this modification improved the fit to an acceptable level with $\chi^2/\nu = 1.04(328)$. However, among the obtained parameters in table 5.14, $R_{\rm bb} = 16 \pm 1$ km is not reasonable, significantly exceeding the NS radius (~ 10 km).

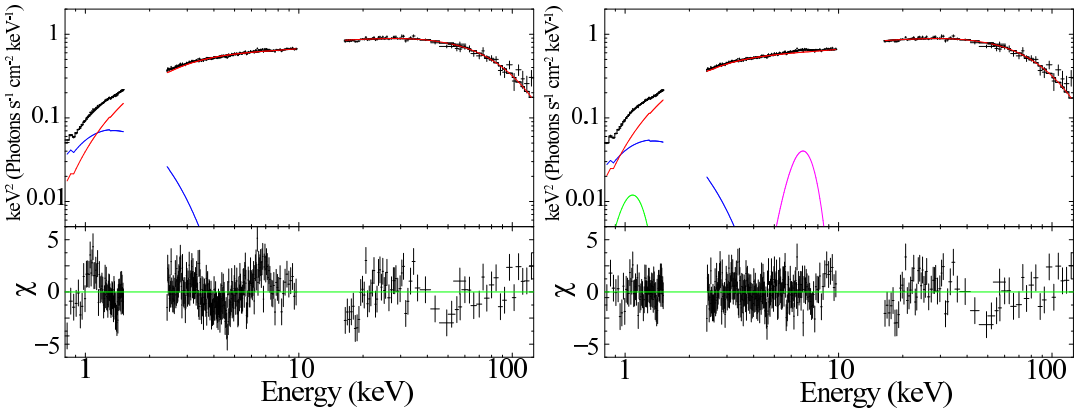

Figure 5.22: Spectral fits to AqlX-1 in the brightening hard state (Obs-R1) with models DC_b (left panel), and with DC_b plus two broad `Gaussian`s (right panel). The green and purple represent the sum of (ionized) Ne and Fe K_α lines, respectively.

Table 5.13: Best-fit DC_b parameters of Obs-R1.

Component	Paramater	Value[a]
wabs	$N_{\rm H}$ (10^{22}cm^{-2})	0.36 (fixed)
diskBB	$T_{\rm in}$ (keV)	0.36 ± 0.04
	$R_{\rm in}$ (km)[bc]	22 ± 4
nthcomp	$T_{\rm bb}$ (keV)	0.56 ± 0.03
(BB seed)	$R_{\rm bb}$ (km)[b]	16 ± 1
	$T_{\rm e}$ (keV)	20 ± 1
	Γ	1.82 ± 0.01
	τ	3.67 ± 0.02
`Gaussian1`[d]	σ (keV)	$0.16^{+0.03}_{-0.02}$
	EW (eV)[e]	40 ± 10
`Gaussian2`[f]	σ (keV)	$1.0^{+0.3}_{-0.2}$
	EW (eV)[e]	160^{+40}_{-20}
Fit goodness[g]	$\chi^2_\nu(\nu)$	1.02 (330)
Luminosity[h]	$L_{\rm x}$ (erg s^{-1})	1.48×10^{37}

[a] Errors represent 90% confidence limits.
[b] Assuming the distance of 5.2 kpc without propagating its error of 0.7 kpc.
[c] Assuming the source inclination of 45 degree, and corrected according to equation 2.7.
[d] The centroid energy is fixed to 1.0 keV.
[e] Equivalent width.
[f] The centroid energy is fixed to 6.6 keV.
[g] A systematic error of 1% is included.
[h] Unabsorbed luminosity in 0.8–100 keV.

The successful reproduction of the Obs-R1 spectrum by DC_b, but with unreasonably largeBB radius as $R_{bb} = 16 \pm 1$ km, means that the data require more seed photons than can be supplied from the entire NS surface: this is already suggested by the first feature in figure 5.22, because the DC_b model employed there assumes that the whole NS surface is emitting the seed BB photons. The seed photons could be increased in number by raising T_{bb} as $\propto T_{bb}^3 R_{bb}^2$, but then, the Rayleigh-Jeans region (which scales as $\propto E^4$ in an $\nu F\nu$ form) would show up in the spectrum at energies of $\lesssim T_{bb}$, and would disagree with the data. This suggests a need for an additional seed-photon source, for which the optically-thick disk is the most natural, and an almost unique, candidate. Actually, such a "double-seed" modeling was employed successfully by Sugizaki et al. (2013) to explain *RXTE* spectra of the transient LMXB MAXI J0556-332.

Based on the above consideration, we constructed a new model, denoted C_dC_b, wherein not only BB but also `diskBB` is Comptonized by the same corona. As shown in figure 5.23, this model successfully reproduced the spectrum. As expected, R_{bb} has decreased to a reasonable value of 11 ± 1 km. Thus the fit has become acceptable, both statistically and physically, without any additional parameters, i.e. with the same degree of freedom as DC_b.

When T_e is allowed to vary between `nthcomp` (disk) and `nthcomp` (BB), namely a two-temperature corona, the values become distinct as 14^{+4}_{-2} keV for the disk emission and 26^{+3}_{-4} keV for BB, while the other parameters stay within errors. Although this modification does not improve the fit as χ^2/ν remains at 1.02(327), it suggests that T_e is not necessarily be common in the two seed emission.

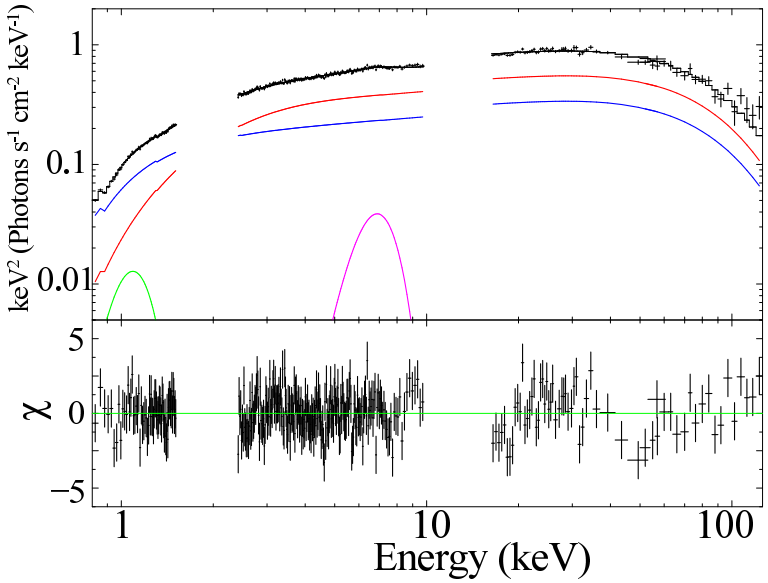

Figure 5.23: The same Obs-R1 spectrum as figure 5.22, but fitted with C_dC_b.

Table 5.14: Best-fit C_dC_b parameters of Obs-R1.

Component	Paramater	Value
wabs	N_H (10^{22}cm^{-2})	0.36 (fixed)
nthcomp (disk)	T_{in} (keV)	$0.27^{+0.07}_{-0.06}$
	R_{in} (km)[ab]	40^{+24}_{-14}
	T_e (keV)	-
	Γ	-
nthcomp (BB)	T_{bb} (keV)	0.62 ± 0.03
	R_{bb} (km)[a]	11 ± 1
	T_e (keV)	21 ± 1
	Γ	1.82 ± 0.01
	τ	3.60 ± 0.07
`Gaussian1`[c]	EW (eV)[d]	50 ± 10
`Gaussian2`[e]	EW (eV)[d]	17 ± 2
Fit goodness[f]	$\chi^2_\nu(\nu)$	1.02 (330)
Luminosity	L_x (erg s^{-1})	1.49×10^{37}

[a]Assuming the distance of 5.2 kpc without propagating its error of 0.7 kpc.

[b]Assuming the source inclination of 45 degree, and corrected according to equation 2.7.

[c]The centroid energy and width are fixed to 1.0 keV and 0.16 keV, respectively.

[d]Equivalent width.

[e]The centroid energy and width are fixed to 6.6 keV and 1.0 keV, respectively.

[f]A systematic error of 1% is included.

5.3.3 A short summary

From our spectral analysis of Aql X-1 conducted so far, we have arrived at a working hypothesis that the hard-state spectra are dominated by the BB Comptonization, while the disk emission is either too soft to detect (at $L_{abs} < 0.01 L_{edd}$; e.g. §5.1.4) or visible at the softest end of the spectrum (§5.1). The disk photons are also Comptonized at least when $L_{abs} \sim 0.1 L_{edd}$ (§5.3.2). As we obtained several physical parameters through the analysis, let us see their behavior here.

As a preparation, we investigated a relation of the optical depth between the two Compton codes, `nthcomp` and `compPS` which are utilized in the present thesis. To avoid confusing, optical depth for `nthcomp` and `compPS` are denoted here as τ_n and τ_{cps}, respectively. Using `nthcomp`, a series of spectra were simulated in $0.1 - 100$ keV for several values of T_e $(20, 30, 40$ keV) and various Γ values s.t. τ_n is within the application range of $\tau_n > 2$ (Zdziarski et al. 1996), and fit them with `compPS` to get corresponding optical depth τ_{cps}. The range of τ_{cps} is also limited, to $\tau_{cps} \leq 3$ because of an application limit of `compPS` (Poutanen & Svensson 1996). Blackbody with $T_{bb} = 0.5$ keV is employed

for the seed photons, and for simplicity, $T_{\rm e}$ in `compPS` is fixed to that of `nthcomp` for fittings. As exemplified in figure 5.24 (a), the overall spectral shape between the two codes approximately correspond, at worst within 10% in the soft band of < 10 keV and $< 20\%$ above $\gtrsim 20$ keV, for all values of $\tau_{\rm n}$ and $T_{\rm e}$. The difference is within a tolerance, as is smaller or comparable than the typical statistical errors in our data sets. Obtained best-fit $\tau_{\rm cps}$ values are plotted in panel (b) against $\tau_{\rm n}$. Since the scatters around the line of $\tau_{\rm cps} = \tau_{\rm n}$ are within $\sim 10\%$ at least in $2 < \tau_{\rm n} \lesssim 3$, we may regard `nthcomp` and `compPS` as to give optical depth consistent within $\sim 10\%$. Therefore, $\tau_{\rm cps}$ and $\tau_{\rm n}$ are treated evenly hereafter, although the possible difference of $\sim 10\%$ should be kept in mind.

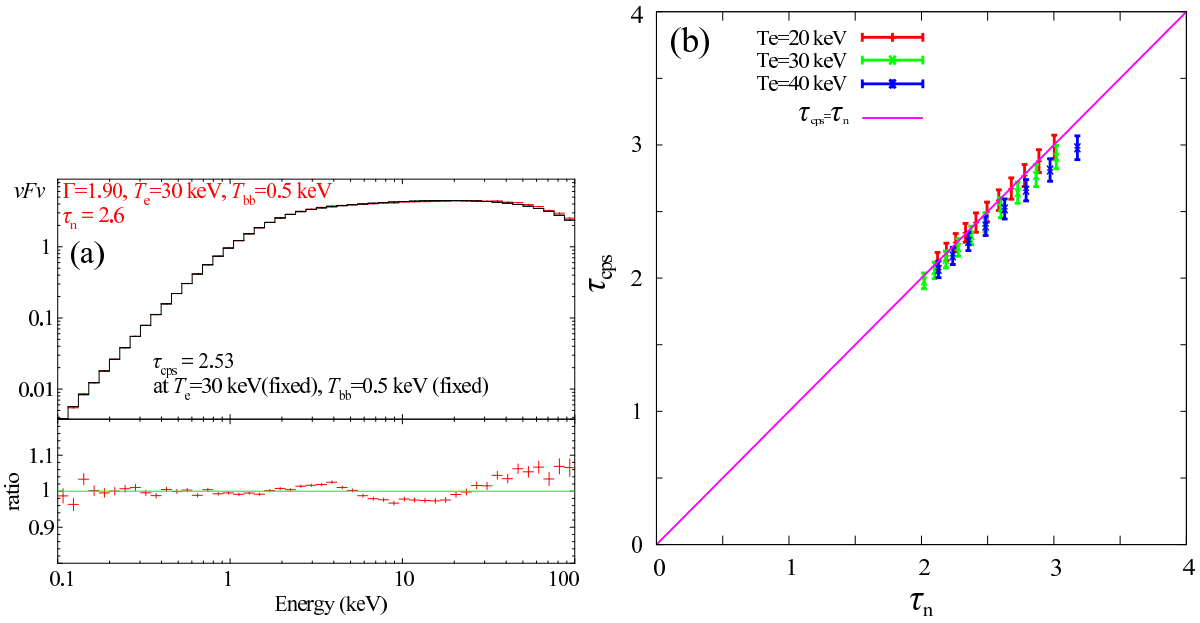

Figure 5.24: An example of fit with `compPS` to a simulated spectrum by `nthcomp` (panel a) and relation between $\tau_{\rm cps}$ and $\tau_{\rm n}$ at $T_{\rm e} = 20, 30$, and 40 keV (panel b). The errors of $\tau_{\rm cps}$ are taken as 3%, for reference.

Figure 5.25 plots, as a function of $L_{\rm x}$ (as defined in §5.1.2), the parameters obtained in §5.1 and §5.3.2. namely $T_{\rm bb}$, $R_{\rm bb}$, $T_{\rm e}$, and τ. As $T_{\rm e}$ and τ for Obs-D5−7, those of $\rm C_b$ are employed here. Thus, the hard-state parameters evolve systematically and monotonically each as a single-valued function of $L_{\rm x}$, including both the decaying and rising phases, while the soft-state ones are largely deviated from that trend. The value of $T_{\rm bb}$ in the hard state increases with luminosity as $\propto L_{\rm x}^{0.121\pm0.007}$, and $R_{\rm bb}$ also does approximately as $\propto L_{\rm x}^{0.2}$, but is saturated at ~ 10 km in $L_{\rm x} \gtrsim 10^{36}$ erg s^{-1} . The coronal temperature $T_{\rm e}$ decreases with $L_{\rm x}$, and has ~ 1 order of magnitude difference between the soft state and the hard state. The behavior of τ vs. $L_{\rm x}$ is approximated as $\propto L_{\rm x}^{0.5}$ at $L_{\rm x} > 10^{35}$ erg s^{-1} , but below $L_{\rm x} \sim 10^{35}$ erg s^{-1} , the value of τ appears to reach a floor at ~ 0.2 (Obs-D6 and Obs-D7). In §6.1, these properties are examined in further details, where results on the other sources are also considered.

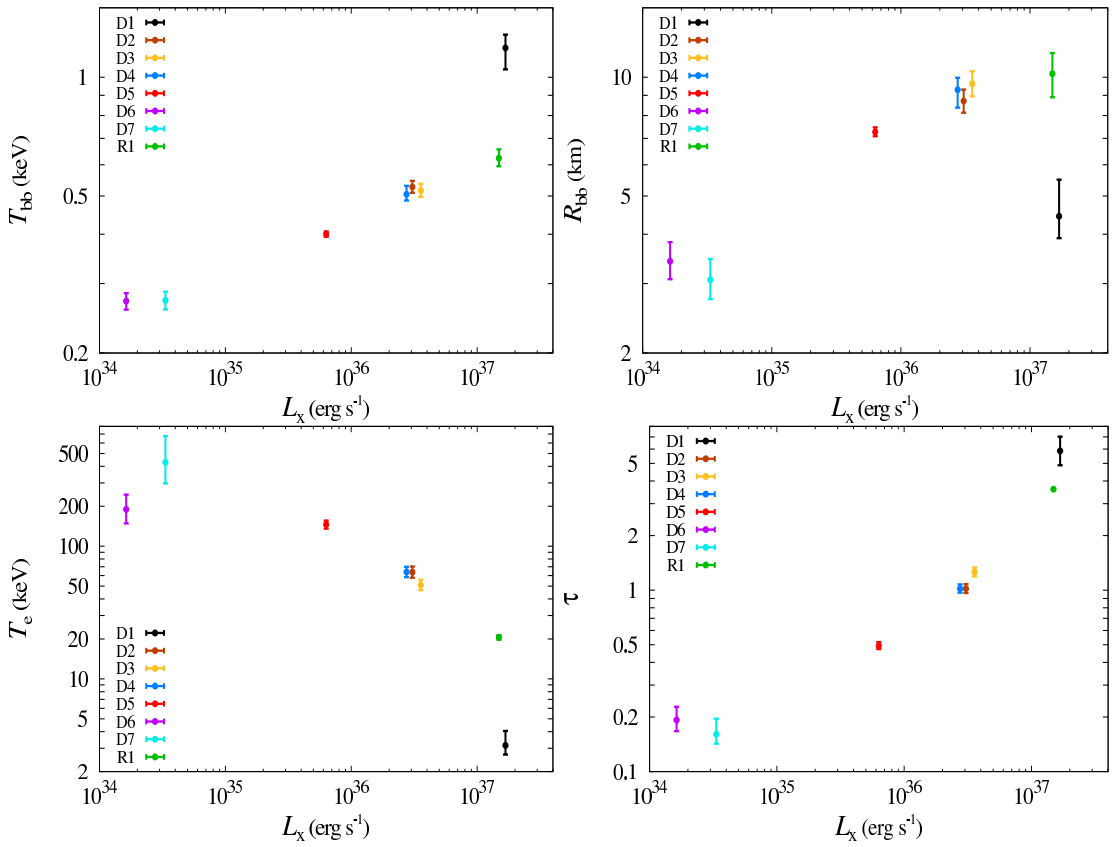

Figure 5.25: The spectral parameters of Aql X-1 in Obs-D1−D7 and Obs-R1 plotted against L_x. Panels (a) through (d) show T_{bb}, R_{bb}, T_e, and τ, respectively. Colors specify the different observations. Black (Obs-D1) is the soft state, while all the others are the hard state.

5.4 Aql X-1: Hard-to-Soft State Transition

5.4.1 Overview

After three days from the bright hard state in Obs-R1, Aql X-1 made the hard-to-soft state transition (§4.3.2). The light curves in figure 4.6 are further divided into finer energy bands, and shown in figure 5.26. Clearly, the intensity below ~ 10 keV decreased across the transition, while that above 12 keV increased instead, with a pivot at ~ 10 keV. Considering this, we divided the entire observation into ten periods P_i ($i = 0...9$), as indicated in figure 5.26. The spectra of all the periods are shown in figure 5.27. The beginning hard state is even brighter than Obs-R1 by a factor of ~ 2. Importantly, we may see a slight concave feature, virtually an inflection point, around $3 - 4$ keV. The last soft-state spectrum is similar to that of Obs-D1 with the the bright soft emission and a low cutoff of < 10 keV, and hence considered to give an analogous result. In addition, a consistent analysis of the 10 spectra is expected to provide, for the first time, valuable knowledge on how the state transition actually proceed, and how the hard-state description is connected to that of the soft state.

5.4.2 Spectral analysis

Combining the glimpse of the spectra in §5.4.1 and the results on the soft state revealed §5.1.2, the emission in the last stage may be composed of a strong disk emission and a Comptonized BB with a low T_e. Moreover, the concave feature around $3 - 4$ keV in the beginning suggests presence of a soft excess and a hard Comptonization component. Therefore, we suppose that the spectral transition, when the hardness H changed by > 1 order of magnitude, is expressed by a consistent modeling, i.e. the combination of `diskBB` and a Comptonized BB, while their parameters change considerably.

As shown in figure 5.28, our attempt with $\mathrm{DC_b}$ has resulted in success. All the spectra from P_0 to P_9 are well reproduced by the model, and the obtained best-fit parameters for each period are listed in table 5.15. As shown in figure 5.29, the drastic evolution of the spectra is expressed by a coutinuous change of the parameters of the disk emission and the Comptonized BB. The rapid spectral growth in the soft band (< 5 keV) is carried by the disk emission: the disk inner radius shrank from ~ 30 km to $\lesssim 20$ km as T_in increased from 0.5 keV to 0.9 keV, so that its luminosity $\propto T_\mathrm{in}^4 R_\mathrm{in}^2$ increased by a factor of ~ 5. At the same time, the source faded in the hard band above ~ 20 keV. This is mainly due to the T_e change, from 14 keV to ~ 3 keV, the cutoff at a very low energy. Associated with this decrease of T_e, τ slightly increased from ~ 4 to ~ 5, and R_bb decreased from ~ 10 km to 5 km. These prove the coronal shape change,

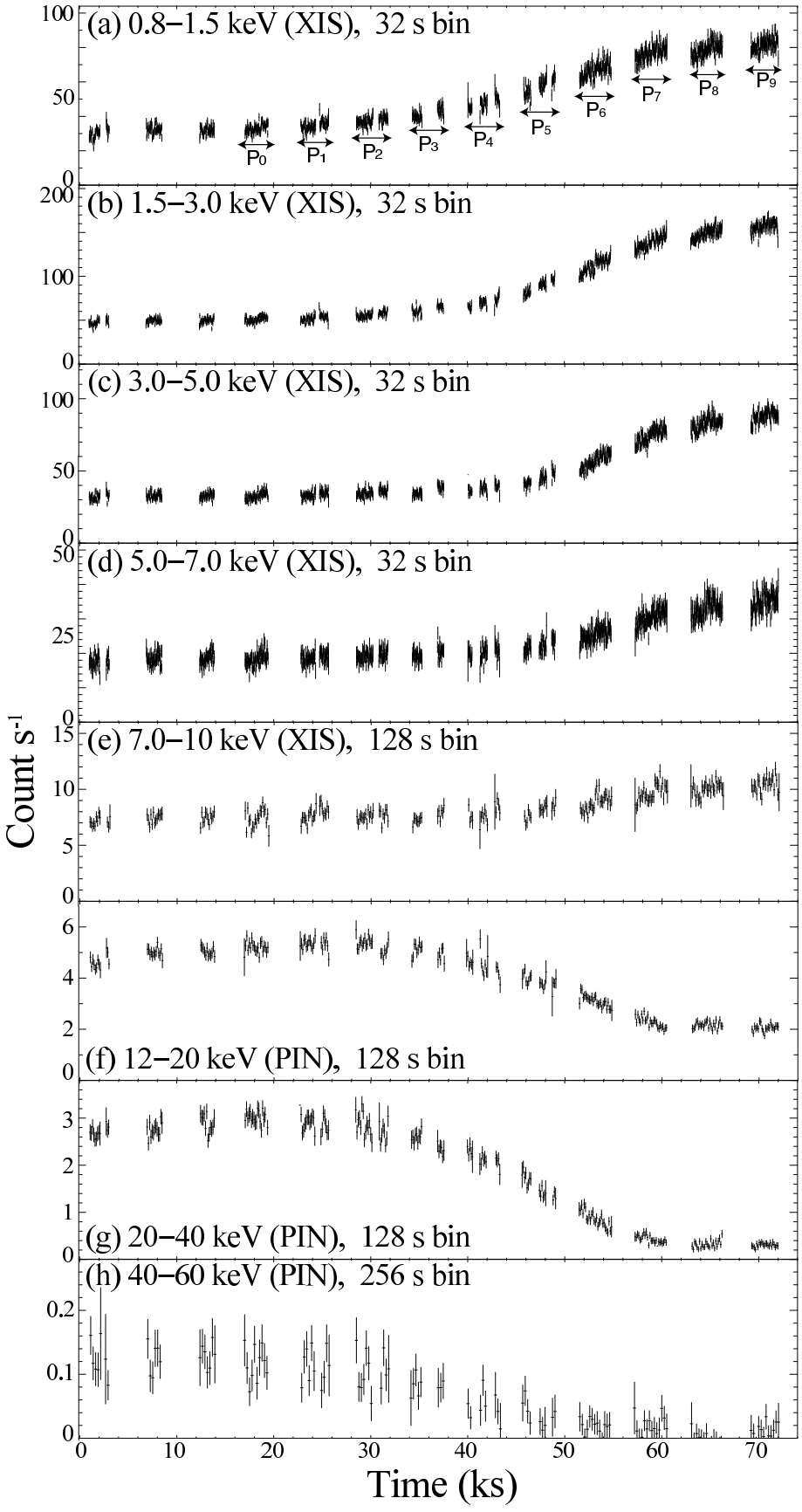

Figure 5.26: *Suzaku* light curves of of Aql X-1 during a state transition (Obs-R2) divided into eight energy bands.

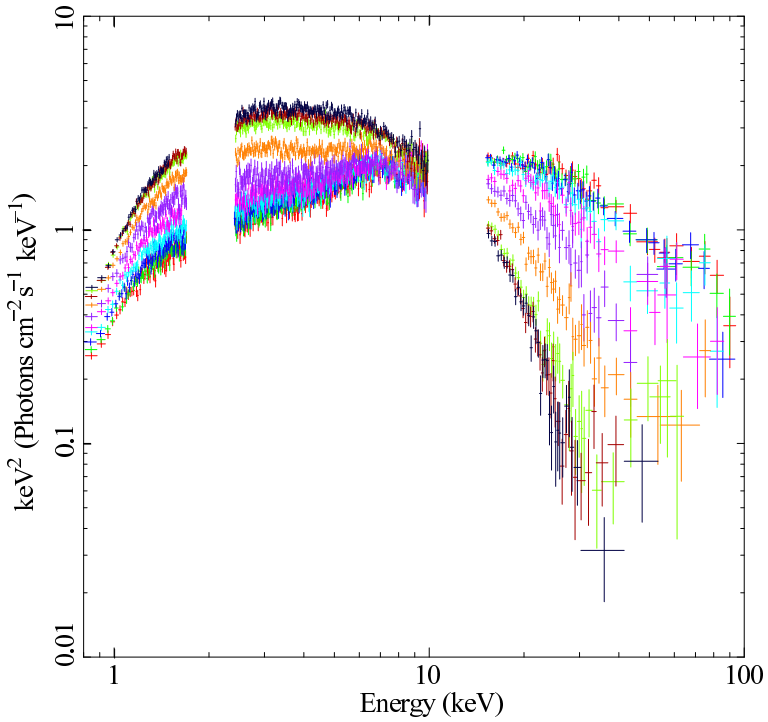

Figure 5.27: *Suzaku* spectra of Aql X-1 during the hard-to-soft state transition in Obs-R2. The red, green, blue, light blue, magenta, purple, light brown, light green, brown, and black represent the spectrum of P_i ($i = 0...9$), respectively.

namely, that the spherical flow around the NS turned into the belt-shaped one in the soft state. Thus, the hard-to-soft state transition in Aql X-1 Obs-D2 can be understood as the transformation of the optically-thin flow (corona) to the optically-thick disk (the standard accretion disk), because the DC_b modeling is statistically acceptable and the derived parameters are physically reasonable.

In some of the spectra, hard-tail-like features are seen at > 30 keV. The tail is most prominent in P_7, lying in the midst to the end of the transition. A similar feature has been reported by Raichur et al. (2011) in the Obs-D1 occasion. Although Sakurai et al. (2012) concluded that the tail in Obs-D1 is not significant considering the systematic errors of the HXD background (Fukazawa et al. 2009), the feature seen in the P_7 spectrum should be examined in the same way. In the $40 - 70$ keV energy range, the background modeling of HXD-PIN has a 1-σ systematic error of 2.8% for an exposure of 10 ks, and 1.8% for 20 ks (Fukazawa et al. 2009). Since the exposure of P_7 is 3 ks, the systematic error is estimated as $\sim 6\%$, by extrapolating the above values in a logarithmic scale ($\sim$ geometric mean). As shown in figure 5.30, the hard-tail signals are confirmed to be significantly higher than the systematic-error level estimated in this way. For reference, an additional power law was able to compensate for the tail with the photon index of $\Gamma = -0.56$. Although this phenomenon is very interesting, examination of its nature is beyond the scope of the present thesis.

Table 5.15: Best-fit DC_b parameters of Obs-R2 spectra across the transition.

	Component					Parameter				
	`wabs`	`diskBB`		`nthcomp`(BB)						
	N_H (10^{22} cm^{-2})	T_{in} (keV)	R_{in} (km)	T_{bb} (keV)	R_{bb} (km)	T_e (keV)	Γ	τ	$\chi^2_\nu(v)$	L_X (erg s^{-1})
P_0	0.36 (fixed)	0.52 $\pm$0.03	30 $\pm$3	1.02 $\pm$0.07	9 $\pm$1	13 $\pm$1	2.00 $\pm$0.03	4.11 $\pm$0.07	1.18 (340)	3.6 $\times 10^{37}$
P_1	0.36 (fixed)	0.50 $\pm$0.03	32 $\pm$3	1.01 $^{+0.06}_{-0.07}$	9 $\pm$1	12 $^{+1}_{-2}$	2.00 $^{+0.03}_{-0.04}$	4.24 $\pm$0.07	1.15 (338)	3.7 $\times 10^{37}$
P_2	0.36 (fixed)	0.50 $\pm$0.03	34 $^{+3}_{-4}$	0.99 $^{+0.06}_{-0.07}$	10 $\pm$1	12 $\pm$1	2.02 $^{+0.03}_{-0.04}$	4.23 $\pm$0.07	1.12 (340)	3.7 $\times 10^{37}$
P_3	0.36 (fixed)	0.54 $\pm$0.02	32 $\pm$2	1.08 $^{+0.06}_{-0.07}$	8 $\pm$1	11 $^{+1}_{-2}$	2.12 $\pm$0.05	4.19 $^{+0.10}_{-0.08}$	1.14 (339)	3.7 $\times 10^{37}$
P_4	0.36 (fixed)	0.59 $\pm$0.02	29 $\pm$2	1.21 $\pm$0.07	7 $\pm$1	13 $^{+2}_{-4}$	2.31 $^{+0.07}_{-0.08}$	3.2 $\pm$0.1	1.13 (332)	3.8 $\times 10^{37}$
P_5	0.36 (fixed)	0.62 $\pm$0.03	29 $\pm$2	1.19 $^{+0.09}_{-0.10}$	7 $\pm$1	8 $^{+1}_{-2}$	2.4 $\pm$0.1	4.1 $\pm$0.2	1.11 (333)	3.8 $\times 10^{37}$
P_6	0.36 (fixed)	0.77 $\pm$0.02	22 $\pm$1	1.50 $^{+0.09}_{-0.10}$	5 $\pm$1	16 $\pm$1	3.44 $\pm$0.01	1.5 $\pm$0.2	1.14 (336)	4.2 $\times 10^{37}$
P_7	0.36 (fixed)	0.87 $\pm$0.03	19 $\pm$1	1.50 $^{+0.08}_{-0.10}$	5 $\pm$1	14 $\pm$1	4.35 $\pm$0.01	1.2 $^{+0.2}_{-0.3}$	1.17 (335)	4.7 $\times 10^{37}$
P_8	0.36 (fixed)	0.94 $\pm$0.02	17 $\pm$1	1.46 $^{+0.06}_{-0.08}$	5 $\pm$1	3.5 $^{+1}_{-0.5}$	3.0 $^{+0.6}_{-0.5}$	5.2 $^{+1.1}_{-0.8}$	1.20 (329)	4.9 $\times 10^{37}$
P_9	0.36 (fixed)	0.91 $\pm$0.02	18 $\pm$1	1.28 $^{+0.06}_{-0.07}$	7 $\pm$1	3.2 $^{+0.5}_{-0.3}$	2.8 $^{+0.4}_{-0.3}$	6.4 $^{+1.0}_{-0.7}$	1.18 (303)	5.1 $\times 10^{37}$

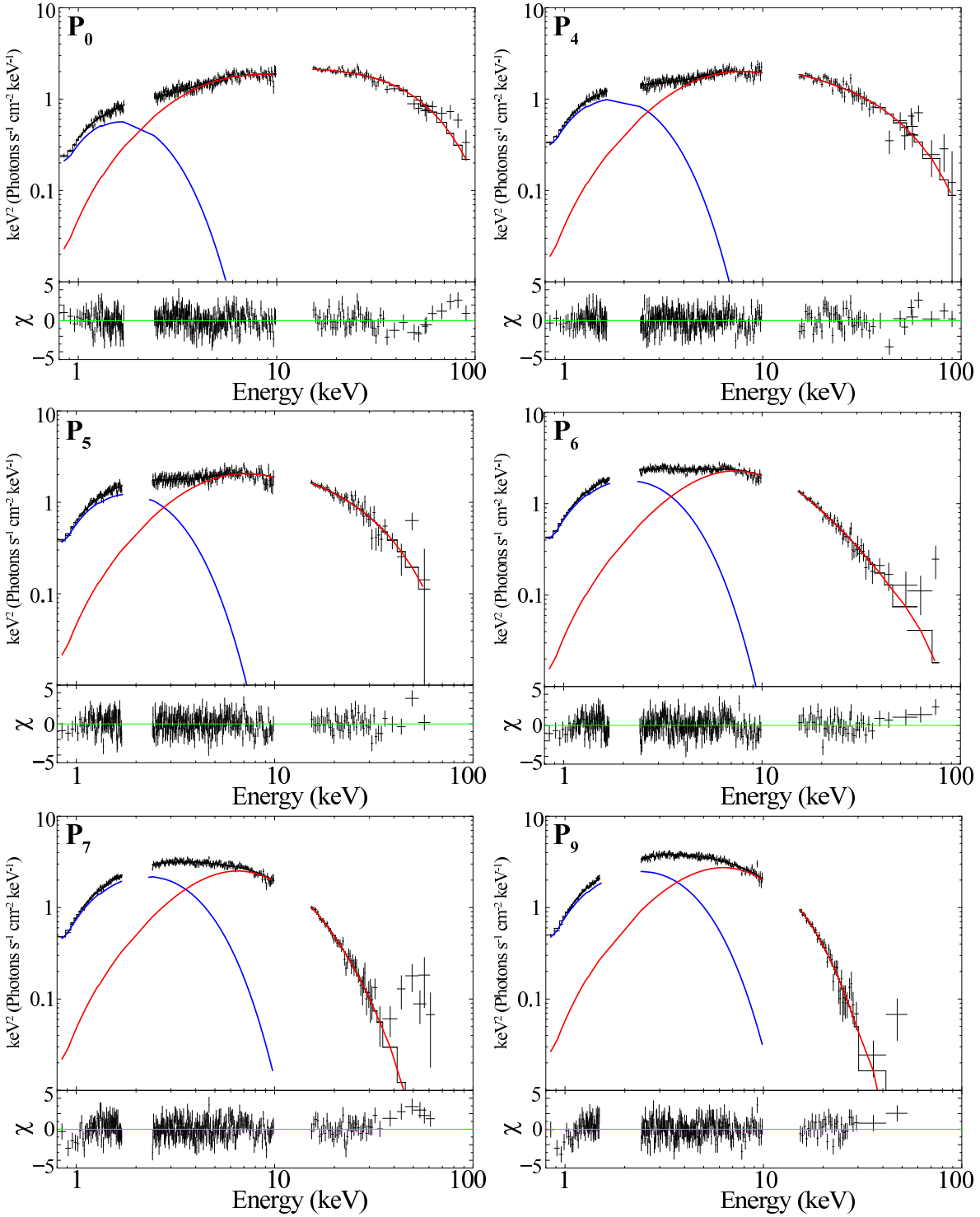

Figure 5.28: Spectral fits of Obs-R2 with DC_b divided into the ten periods. Only 6 out of the 10 fits are presented.

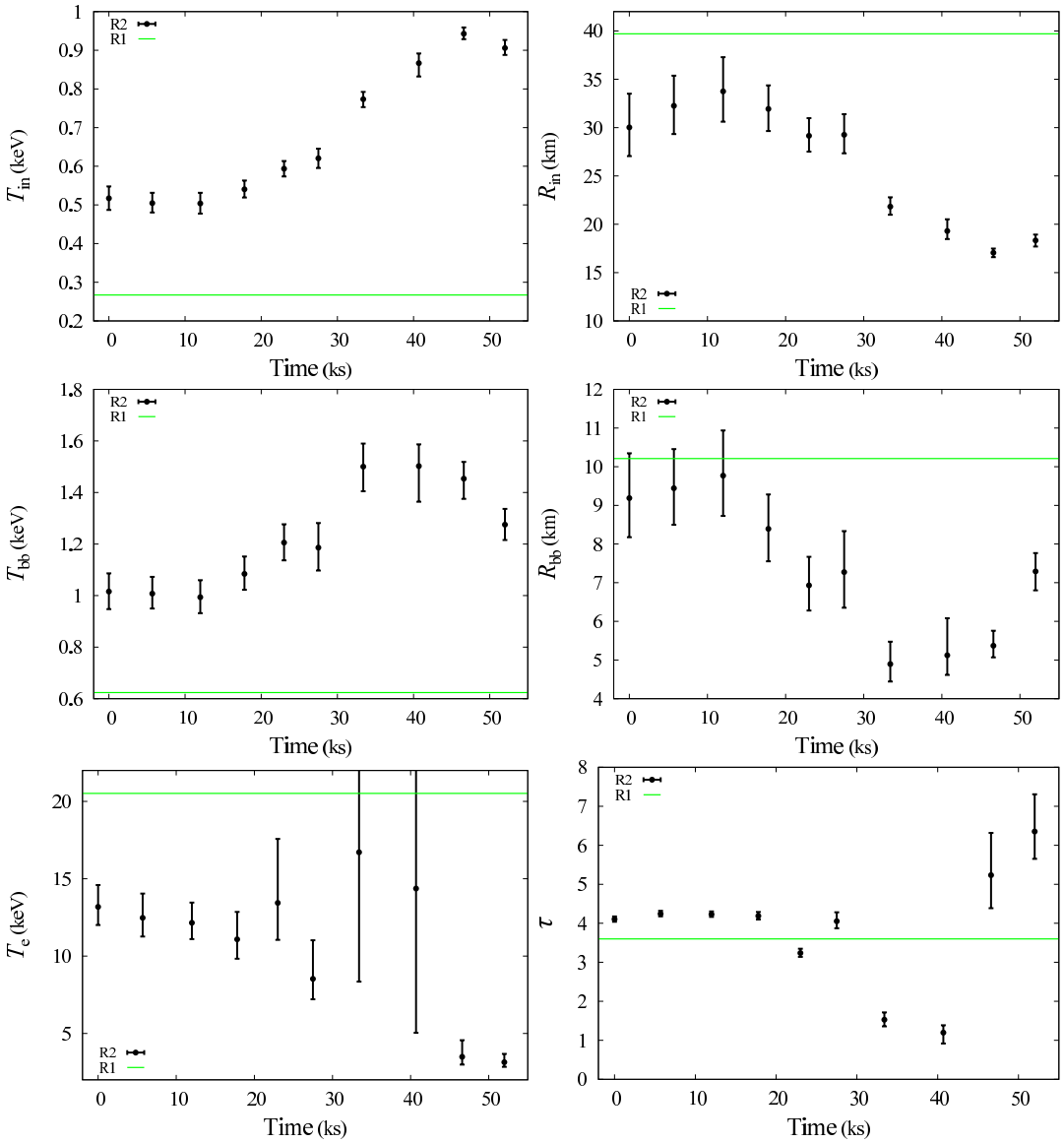

Figure 5.29: The spectral parameters in Aql X-1 Obs-R2 plotted against time. The time origin is that of P_0.

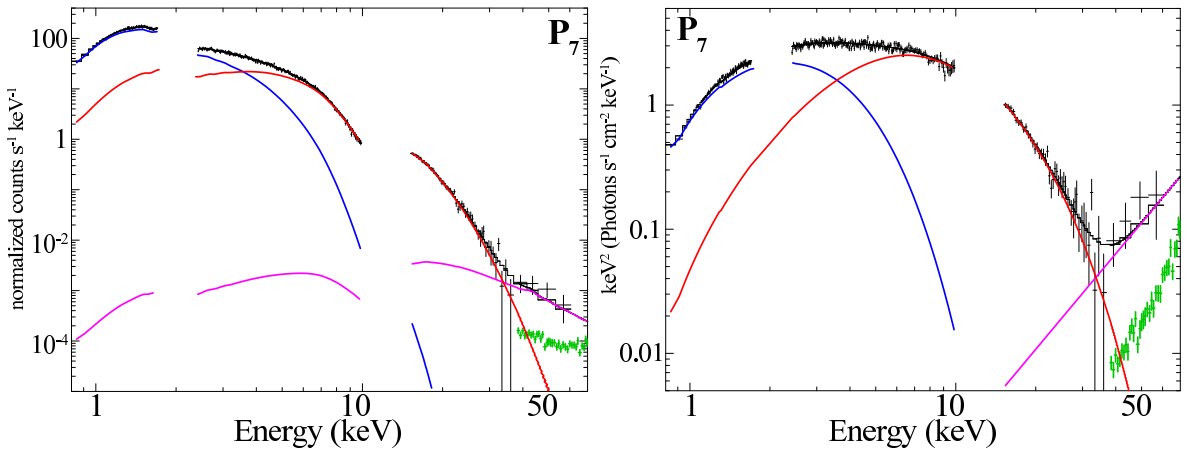

Figure 5.30: The same P_7 spectrum as figure 5.28, with an additional power law component (magenta). The HXD-PIN systematic error level (1σ) is shown in green. The left and right panels are in the count rates and in $\nu F\nu$ form, respectively.

5.5 Hard-State Sources with $L_{\rm abs} \gtrsim 0.01 L_{\rm edd}$

In §5.3, we have obtained the working hypothesis for the luminous hard state with $L_{\rm abs} \gtrsim 0.01 L_{\rm edd}$, which is valid at least for Aql X-1. It should next be examined against other sources having similar luminosities. Below, we hence analyze the remaining data sets in our sample that have $L_{\rm abs} \gtrsim 0.01 L_{\rm edd}$.

5.5.1 4U1705-44

Of the two observations of 4U 1705-44 (§4.4.3), we begin with the slightly brighter one, conducted on 2006/8/26 (401046010) at $L_{\rm abs} = 8.1 \times 10^{36}$ erg s^{-1} . Like in §5.3.2, we applied $\rm DC_b$ to the spectrum. A broad iron line at 6.4 keV, reported previously (Fiocchi et al. 2007; Lin et al. 2010; Egron et al. 2011), was included here in the model with its width fixed to 0.5 keV. The model reproduced the spectrum with $\chi^2/\nu = 1.09(326)$, but gave unreasonably small innermost disk radius as $R_{\rm in} = 3$ km $< R_{\rm NS}$ and high temperature as $T_{\rm in} = 0.9$ keV $> T_{\rm bb} = 0.7$ keV.

The high $T_{\rm in}$ in the $\rm DC_b$ model is possibly due to a color hardening by Comptonization. Therefore, like in §5.3.2, we next tried $\rm C_dC_b$ for the same spectrum. As shown in figure 5.16 (a), the model succeeded in reproducing the spectrum with $\chi^2/\nu = 1.10(326)$. With the help of Comptonization, the disk inner temperature was allowed to become as low as $\lesssim 0.36$ keV, with a reasonable radius of $R_{\rm in} \sim 60$ km. Comparing with Aql X-1 Obs-R1 results, the parameters are quite similar, and indeed all consistent within errors. Thus the spectrum of 4U 1705-44 (401046010) was reproduced by the $\rm C_dC_b$ model like in Aql X-1 Obs-R1, giving the consistent result.

When Γ (τ) is allowed to vary between those on the disk emission and the BB, the fit was improved to $\chi^2/\nu = 1.03(325)$. However, as shown in table 5.16, obtained BB radius was too large as $R_{\rm bb} \sim 26$ km. Figure 5.31 (b) indicates that this is because the contribution of `nthcomp`(disk) in the hard band decreased by a smaller optical depth for the disk emission of $\tau < 2$. Leaving both Γ and $T_{\rm e}$ free did not further improve the fit as $\chi^2/\nu = 1.04(324)$. Therefore, the common corona for the disk and BB is preferred in 4U1705-44 (401046010) occasion.

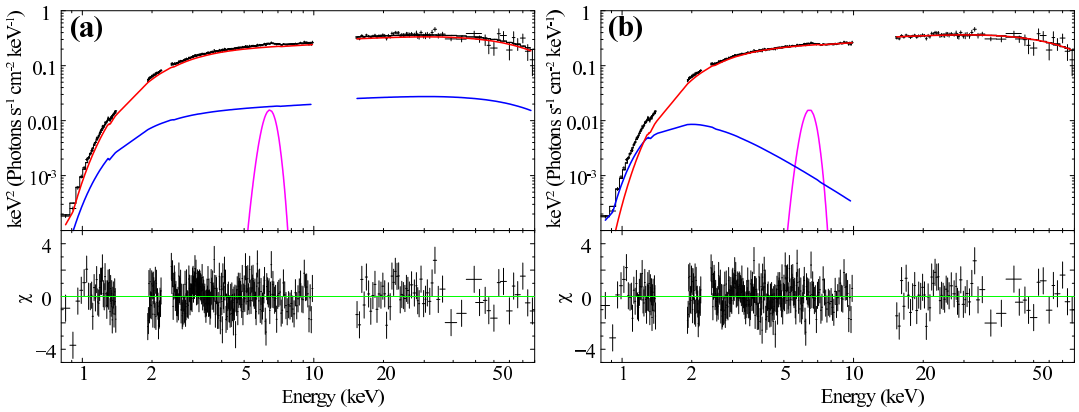

Figure 5.31: Spectral fits to 4U1705-44 (401046010) with C_dC_b. In panel a, Γ and T_e are common in the disk emission and BB, while Γ is allowed to vary between them in panel b.

Table 5.16: The best-fit parameters to the spectra of 4U1705-44 (401046010 and 406076010) with C_dC_b.

Data		401046010		406076010
Model		C_dC_b	C_dC_b[a]	C_dC_b
`wabs`	N_H (10^{22}cm^{-2})	1.6 ± 0.1	$2.54^{+0.01}_{-0.2}$	1.6 (fixed)
`nthcomp`	T_{in} (keV)	$0.13(< 0.36)$	< 0.2	0.13 (fixed)
(disk)	R_{in} (km)[bc]	$68(> 5)$	> 10	$80 - 90$
	T_e (keV)	(common)	(common)	(common)
	Γ	(common)	> 5	(common)
	τ	(common)	< 2	(common)
`nthcomp`	T_{bb} (keV)	0.62 ± 0.01	0.4 ± 0.1	0.59 ± 0.01
(BB)	R_{bb} (km)[b]	11 ± 1	26^{+13}_{-6}	10 ± 1
	T_e (keV)	23^{+4}_{-3}	22^{+4}_{-3}	19^{+4}_{-2}
	Γ	1.82 ± 0.01	1.82 ± 0.01	1.87 ± 0.01
	τ	$3.4^{+0.3}_{-0.2}$	$3.4^{+0.3}_{-0.2}$	$3.7^{+0.4}_{-0.2}$
`Gaussian`[d]	EW (eV)[e]	70^{+20}_{-10}	60^{+10}_{-20}	90 ± 10
`edge`[f]	max τ	-	-	0.05 ± 0.01
Fit goodness	$\chi^2_\nu(\nu)$	1.10 (326)	1.03 (325)	1.06 (314)
Luminosity	L_x (erg s^{-1})	1.13×10^{37}	4.22×10^{37}	6.84×10^{36}

[a]The values Γ and T_e are allowed to vary between the disk emission and the BB seed.
[b]Assuming the distance of 7.4 kpc without propagating its uncertainty.
[c]Assuming the source inclination of 45 degree.
[d]The centroid energy and width are fixed to 6.4 keV and 0.5 keV, respectively.
[e]Equivalen width.
[f]The energy is fixed to 7.1 keV.

The other spectrum of 4U1705-44, obtained on 2012/3/27 (ObsID: 406076010), has a similar shape to the above one. Figure 5.32 shows their ratios using the C_b model in

table 5.16. The difference is mainly in the photon index, namely larger Γ, because the ratios appear straight in log-log plot. In addition, T_e may have possibly decreased. A systematic error of 1% was included here, considering the long exposure (> 80 ks) and rich statistics in the XIS band.

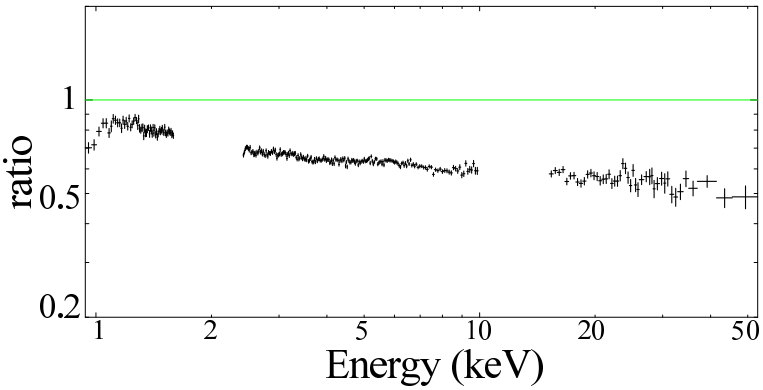

Figure 5.32: Ratios of the fainter spectrum of 4U1705-44 (406076010) to the best-fit C_b model to its brighter data (401046010).

From the straight ratios of the spectra examined above, C_dC_b is expected to be also a solution for this spectrum. As shown in figure 5.33, this model indeed reproduced the spectrum successfully with $\chi^2/\nu = 1.06(314)$. Since the `diskBB` parameters remained poorly constrained due to relatively high N_H, T_{in} and N_H were fixed to those of 401046010 in table 5.16. The parameters of Comptonized BB are almost consistent with those of brighter ones, with slightly lower temperature of $T_{bb} = 0.59 \pm 0.01$. We thus conclude that C_dC_b is the best model for 4U1705-44 spectra, and these result are consistent with that in Aql X-1 Obs-R1, even giving the parameters agree within errors.

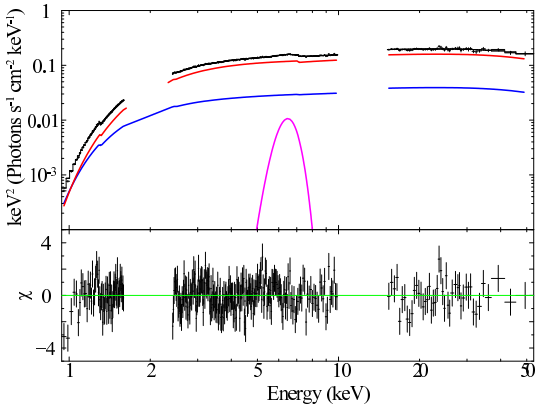

Figure 5.33: A fit to 4U1705-44 (406076010) spectrum with C_dC_b.

5.5.2 GS 1826-238

During the very long ($\sim$ 200 ks in gross time lapse), GS 1826-238 (404007010) showed quasi-periodic type-1 bursts and bright persistent emission (§4.4.6). The source luminosity was $L_{\rm abs} \sim 1.1 \times 10^{37}$ erg s^{-1} $\sim 0.06 L_{\rm edd}$, which is close to those of the previous 4U1705-44 (§5.5.1) and Aql X-1 in Obs-R1 (§5.3.2). A burst-removed and time-averaged spectrum is shown in figure 5.34. In addition to $L_{\rm abs}$, the overall spectral shape is similar to those of the previous ones, with the hard slope of $\Gamma < 2$ which is somewhat harder, and a cutoff around $\sim$ 20 keV. We included a systematic error of 1% due to the rich statistics.

With the same manner as §5.3.2 and §5.5.1, we made a first attempt with $\rm DC_b$. The model reproduced the spectrum with $\chi^2/\nu = 1.24(326)$, but gave unreasonable inner disk radius as $R_{\rm in} = 6 \pm 1$ km < 10 km, with high a temperature of $T_{\rm in} \sim 0.6$ keV. This is because the spectrum at $\lesssim 2$ keV is so accurately determined that there is no tolerance for a cool and large disk to contribute. By an analogy to the results of Aql X-1 Obs-R1, we expect that $\rm C_dC_b$ may solve the problem and give reasonable parameters. The model, as shown in figure 5.34, indeed reproduced the spectrum with $\chi^2/\nu = 1.26(327)$. The best-fit parameters are listed in table 5.17. By Comptonizing the disk emission, the color temperature was successfully lowered to $T_{\rm in} < 0.2$ keV and $R_{\rm in} > 48$ km has became a reasonable value. The derived value of $T_{\rm e} = 16 \pm 1$ keV is comparable to those of Aql X-1 in Obs-R1 and 4U1705-44 (401046010 and 406076010). This is considered to be a common feature of sources at $L_{\rm abs} \sim 0.1 L_{\rm edd}$. Furthermore, the relatively higher $\tau \sim 4.7 > 3$ also applies to these (cf. $\tau > 3.2$ in 4U1705-44 and $\tau = 3.60 \pm 0.07$ in Aql X-1 Obs-R1).

Allowing Γ (τ) to vary between `nthcomp` (disk) and `nthcomp` (BB) did not change the parameters, as all of them stay within errors. When both Γ and $T_{\rm e}$ are released, as shown in figure 5.17 (right panel), the fit was significantly improved to $\chi^2/\nu = 1.06(324)$. The parameters are again listed in table 5.17. In this case, the disk emission is Comptonized by a low-temperature ($T_{\rm e} = 6 \pm 1$ keV) and very optically-thick ($\tau = 10 \pm 1$) corona. The coronal parameters for the BB roughly stayed within errors. The BB radius increased to a large value of $\sim$ 14 km, which can reduced to $\sim$ 10 km by assuming the distance of $\sim$ 5 kpc (within 7^{+1}_{-3} kpc: §4.1.2). Thus, the fit with two different corona is preferred in terms of fit goodness, and might be allowed by accepting $R_{\rm bb} \sim 14$ km or assuming the smaller distance.

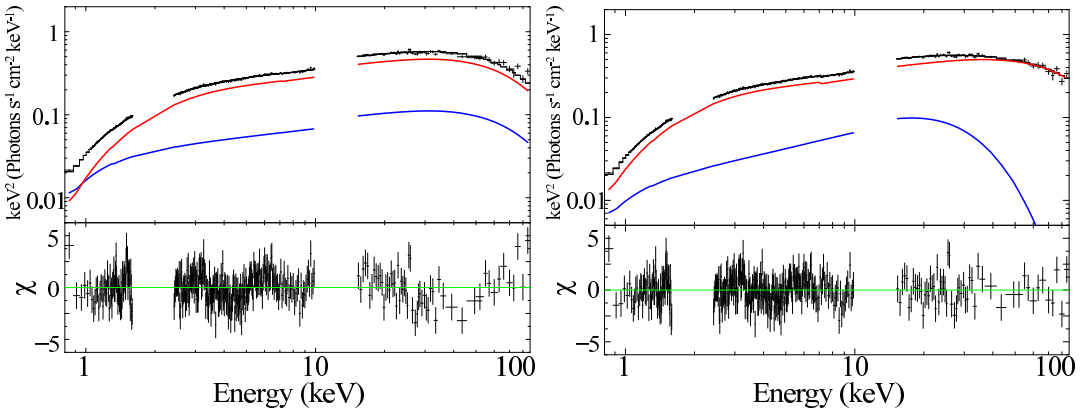

Figure 5.34: A spectral fit of GS1826-238 (404007010) with C_dC_b, when the values of Γ and T_e are common in the disk emission and the BB (left panel) and both allowed to vary (right panel).

Table 5.17: Best-fit C_dC_b parameters of GS 1826-238 (404007010).

Model		DC_b	C_dC_b	C_dC_b[a]
wabs	N_H (10^{22}cm^{-2})	0.26 ± 0.02	0.30 ± 0.01	0.24 ± 0.04
`diskBB`	T_{in} (keV)	$0.61^{+0.09}_{-0.08}$	-	-
	R_{in} (km)[bc]	6 ± 1	-	-
nthcomp	T_{in} (keV)	-	< 0.19	< 4.5
(disk)	R_{in} (km)[bc]	-	> 48	$\gtrsim 1$
	T_e (keV)	-	(common)	6 ± 1
	Γ	-	(common)	$1.54^{+0.09}_{-0.06}$
	τ	-	(common)	10 ± 1
nthcomp	T_{bb} (keV)	$0.69^{+0.08}_{-0.05}$	0.61 ± 0.01	$0.57^{+0.02}_{-0.01}$
(BB)	R_{bb} (km)[a]	11 ± 1	11 ± 1	14 ± 2
	T_e (keV)	16 ± 1	16 ± 1	20^{+4}_{-2}
	Γ	$1.74^{+0.02}_{-0.01}$	1.72 ± 0.01	$1.72^{+0.09}_{-0.06}$
	τ	4.5 ± 0.2	4.7 ± 0.2	$4.1^{+0.4}_{-0.2}$
Fit goodness[c]	$\chi^2_\nu(\nu)$	1.24 (326)	1.26 (326)	1.06 (324)
Luminosity	L_x (erg s^{-1})	1.45×10^{37}	1.46×10^{37}	1.47×10^{37}

[a]The values Γ and T_e are allowed to vary between the disk emission and the BB seed.

[b]Assuming the distance of 7 kpc without propagating its error of -3/+1 kpc.

[c]Assuming the source inclination of 45 degree, and corrected according to equation 2.7.

[d]A systematic error of 1% is included.

Chapter 6

DISCUSSION

6.1 Summary of the Results

In Chapter 5, we have analyzed 17 spectra of 8 LMXBs in their hard state, together with one soft-state data set. The most important finding is that the spectra in either state are expressed in a unified and consistent manner by the three or fewer ingredients; the BB emission from the NS surface, the disk emission, and the Compton corona. In this section, the behavior of the three components is individually summarized, mainly focusing on how they depend on $L_{\rm x}$ (defined in §5.1.2) through the hard state, and how they change across the state transition.

6.1.1 Blackbody on the NS surface

In all the hard-state spectra, the dominant hard component with $\Gamma \sim 2.0$ has been successfully described by thermal Comptonization (`nthcomp` or `compPS`), assuming a seed photon supply from a BB source to be identified with optically-thick emission from the heated NS surface. Thus, we have been able to obtain the two BB parameters, $T_{\rm bb}$ and $R_{\rm bb}$. Of these two, $T_{\rm bb}$ is mainly constrained by the spectral shape in the $1-3$ keV range (Rayleigh-Jeans regime), while $R_{\rm bb}$ by the spectrum normalization (or the number of seed photons). The present results provide a unique opportunity to investigate the BB behavior over a wide range of luminosity from $\sim 10^{32}$ erg s^{-1} to $> 10^{37}$ erg s^{-1} .

Although $T_{\rm bb}$ in panel (a) clearly exhibits a positive correlation with $L_{\rm x}$, its dependence on $L_{\rm x}$ is milder than the case of constant emission area, i.e. $\propto L_{\rm x}^{1/4}$ indicated by a straight line. This suggests that $R_{\rm bb}$ significantly increases with $L_{\rm x}$. In the transition of Aql X-1, $T_{\rm bb}$ increased to ~ 1.5 keV, approaching the local Eddington temperature at the NS surface (~ 2.0 keV).

The BB radius was also successfully obtained in all the sources, and its dependence on $L_{\rm x}$ is shown in figure 6.1 (b). Importantly, in the range of 10^{36} erg s^{-1} $< L_{\rm x} \lesssim 4 \times 10^{36}$ erg s^{-1} , $R_{\rm bb}$ has a value of $\sim$ 10 km, which coincides with the canonical NS radius. At this $L_{\rm x}$, the accretion flow is hence considered to plunge onto nearly the entire NS surface, in an approximately spherical manner. When the accretion rate increases from this regime (arrow $a1$ in the figure), $R_{\rm bb}$ decreases and $T_{\rm bb}$ becomes higher, where the source gets closer to the soft state. On the other hand, when $L_{\rm x}$ decreases (arrow $a2$), $R_{\rm bb}$ again decreases approximately as $\propto L_{\rm x}^{0.24\pm0.03}$, and $T_{\rm bb}$ gets lower.

There is another path from $L_{\rm x} \sim 10^{36}$ erg s^{-1} to higher $L_{\rm x}$, as indicated in the figure by arrow $a3$. In this track, $R_{\rm bb}$ remains at the value of $\sim$ 10 km, and $T_{\rm bb}$ further increases. This may be because the emission area on the NS surface is saturated at $R_{\rm bb} \sim 10$ km, and increased $L_{\rm x} \propto T_{\rm bb}^4 R_{\rm bb}^2$ should be carried by $T_{\rm bb}$. In this regime of $L_{\rm x} \sim 10^{37}$ erg s^{-1}, the flow around the NS is still considered to be spherical like that in $L_{\rm x} \sim 10^{36}$ erg s^{-1}, and the corona somehow starts to accommodate the photons of the disk emission too. The dichotomy in this luminous regime ($L_{\rm x} \gtrsim 10^{37}$ erg s^{-1}) should be due to the hysteresis effect. A source is considered to take the a_3 branch when it brightens up from the hard state to the soft state, while follow the a_1 branch when it gets fainter.

Above discussion is based on an assumption that the emission from the NS is an ideal blackbody described by the Planck's law. However, this is not necessarily obvious, and should be carefully examined. The biggest issue is whether or not the spectral shape, or color temperature, accurately represents the true (or effective) BB temperature. That is, when the electron scattering dominates, or the emission region is covered by a thin and hot scattering atmosphere, the observed color temperature increases ("color hardening"), accompanied by an artificial decrease in the emission area. In the Obs-D1 spectrum of Aql X-1 in the soft state, such an effect was actually observed; $T_{\rm bb}$ was at first 1.9 keV (§5.1.2), while it became $T_{\rm bb} = 1.2$ keV (table 5.2) by correctly considering the Comptonization effect. This was possible because a large fraction of the BB emission is directly visible in the spectrum (figure 5.2) under high statistics.

In the hard state spectra, the BB component is "buried" deep in the Comptonized continuum, so that its true shape is hardly observable (e.g., figure 5.5). In addition, the emission region on the NS surface must be illuminated by the Comptonized hard photons. Therefore, the emission may well be subject to significant color hardening. However, very importantly, we have confirmed that at least 4 sources exhibit $R_{\rm bb} \sim 10$ km over a fairly wide range of $L_{\rm X} = (0.01 - 0.1) L_{\rm edd}$. (Distance uncertainties tend to cancel out among them.) If the color hardening were significant, its correction would make $R_{\rm bb}$ exceed the canonical 10 km, leading to an unphysical picture. Therefore, we conclude that the color hardening is not significant and hence the BB component can be

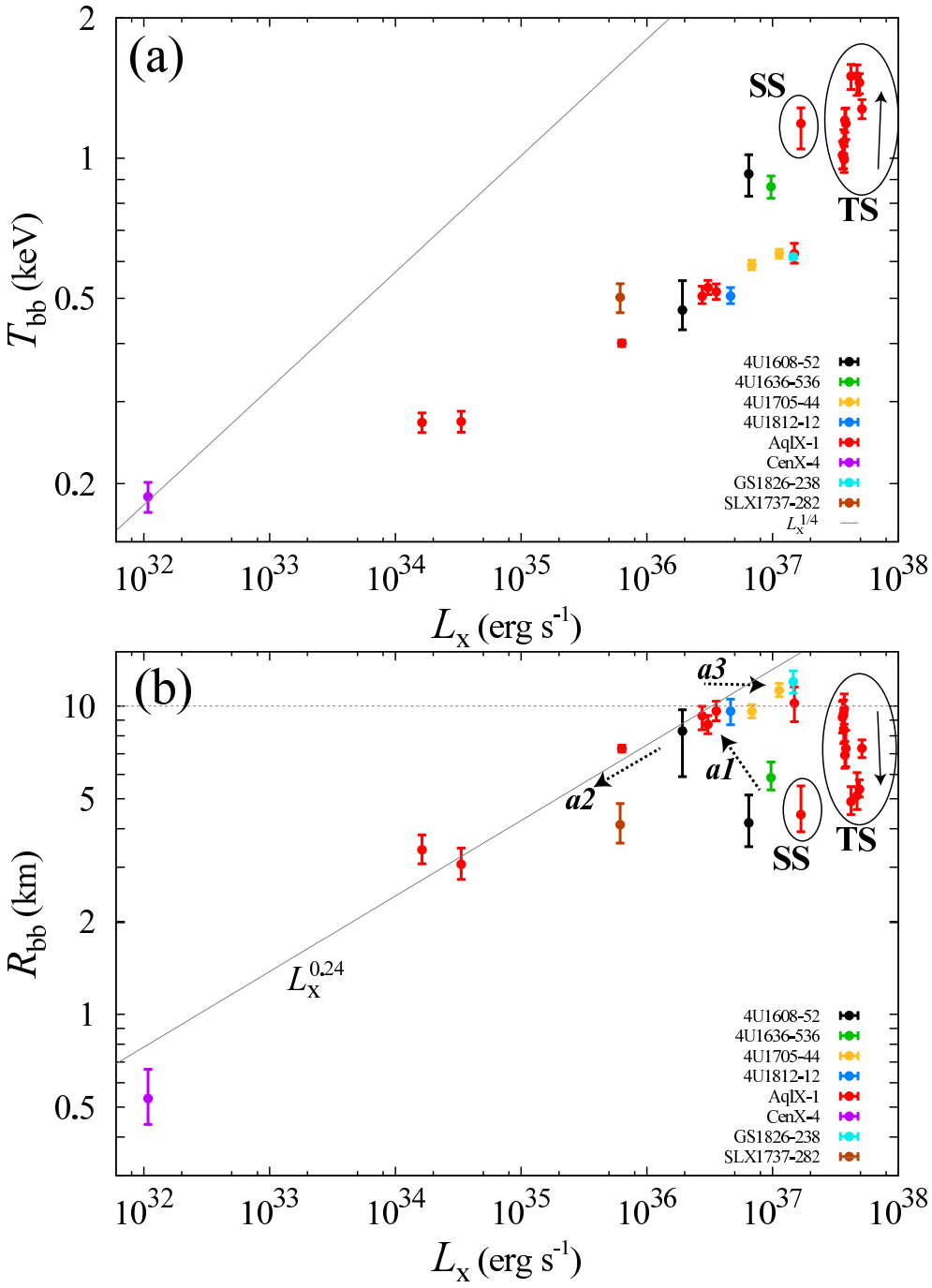

Figure 6.1: A compilation of the BB parameters, derived in Chapter 5 from all LMXB data sets in the sample. Objects are specified by colors. Specifically, the BB temperature ($T_{\rm bb}$: panel a) and the radii ($R_{\rm bb}$: panel b) are plotted against $L_{\rm x}$. The point for 4U1608-52 (404044030) is represented by I_2. The points of Aql X-1 in the soft state (Obs-D1) and in the transition (Obs-R2) are denoted as "SS" and "TS", respectively. The time order in the transition is indicated with an arrow, starting from the hard state to the soft state. The solid straight line in panel (a) represents a relation for a condition of $R_{\rm bb}$ =const. ($T_{\rm bb} \propto L_{\rm x}^{1/4}$).

considered as a true blackbody, at least over this luminosity range. The issue towards lower luminosity is discussed later in §6.2.3.

6.1.2 Disk emission

The disk emission was seen in relatively bright phases in the hard state, and the inner-edge temperature $T_{\rm in}$ and radius therein $R_{\rm in}$ were determined with a reasonable accuracy, except in SLX1737-282 and Cen X-4 having $L_{\rm x} < 10^{36}$ erg s^{-1} . The derived $L_{\rm x}$-dependence of $T_{\rm in}$ is shown in figure 6.2 (a). Except Aql X-1 Obs-R1, 4U1705-44, and GS1826-238, namely the 2-Compton sources, $T_{\rm in}$ thus exhibits a clear positive correlation with $L_{\rm x}$. The relation, though subject to scatters, is generally consistent with the theoretical prediction of $T_{\rm in} \propto L_{\rm x}^{1/4}$ (represented by a straight line) from equation 2.6. It applies to both the hard state and the soft state, over a wide luminosity range of 10^{36} erg s^{-1} $< L_{\rm x} \lesssim 10^{38}$ erg s^{-1} wherein the disk emission is visible. This ensures our interpretation that a standard accretion disk is ubiquitously present in these objects, regardless of the spectral states.

The other parameter, the inner-disk radius $R_{\rm in}$, is plotted in figure 6.2 (b). The value is distributed in a range of $20 - 50$ km, without strong dependence on $L_{\rm x}$. This is just another expression of the relation of $T_{\rm in} \propto L_{\rm x}^{1/4}$ mentioned above. In the soft state and the end of the transition of Aql X-1, $R_{\rm in}$ becomes relatively small as $15 - 20$ km. In all cases, $R_{\rm in}$ is larger than 10 km, which is reasonable and self-consistent because an accretion disk should satisfy $R_{\rm in} > R_{\rm NS}$.

The bolometric luminosity of the disk emission $L_{\rm d}$ is plotted in figure 6.2 (c) as a ratio to $L_{\rm x}$. The values are calculated with $L_{\rm d} = 4\pi D^2 F_{\rm d}$, where D is the distance and $F_{\rm d}$ is the disk-emission flux obtained by integrating the best-fit `diskBB` model numerically from 10 eV to 100 keV. The ratios in the soft state are comparable to 0.5, in agreement with a prediction from virial theorem (§2.2.2) that $L_{\rm d}$ (when $R_{\rm in} \sim R_{\rm NS}$) should carry about half the bolometric luminosity. On the other hand, those in the hard state are all smaller than 0.5. This indicates disk truncation at larger radii, in agreement with the measured values of $R_{\rm in} \sim 20 - 50$ km.

As the disk emission assumed here is after all the sum of many BB emission components (§2.2.1), it may be subject to the same potential problem as the BB as discussed in §6.1.1. In this case, the color hardening becomes even more serious, as argued, e.g., by Shimura & Takahara (1995). They derived a canonical color hardening factor of 1.7, and Makishima et al. (2000) confirmed that this value is appropriate at least in black-hole binaries in the soft state. As described in §2.2.2, we already consider this and another (disk inner-boundary condition) effect when quoting the diskBB parameters. Of course, the color hardening in the present LMXBs can be even higher, because of the coronal

illumination and other effects. Nevertheless, our conclusion will not be affected very much by this uncertainty, because such addition color correction, if any, will make $R_{\rm in}$ larger, and keep valid the basic requirement that $R_{\rm in}$ should be larger than 10 km. In addition, our picture to be presented below is not much dependent on the actual values of $T_{\rm in}$ or $R_{\rm in}$.

6.1.3 Comptonizing corona

The final and key ingredient is the Compton corona, which is characterized by $T_{\rm e}$ and τ. Our extensive studies of the hard-state LMXBs, conducted in Chapter 5, really demonstrate the power of *Suzaku* with its superb broad-band capability, realized by the three instruments; the XIS data very well constrain the seed photon spectrum, those of HXD-PIN measure the Comptonization Γ with high accracy, and the HXD-GSO data provide the valuable information on $T_{\rm e}$. Prior to *Suzaku* , there was no X-ray observatory that can simultaneously provide this complete set of information.

We confirmed in §5.3.3 that the two particular codes we used in the present thesis, `compPS` and `nthcomp`, agree in the overlapping parameter region. In the `compPS` modeling, we have assumed a configuration that a point-like seed photon source (mostly BB) is surrounded by a spherical hot electron cloud, which is relatively close to the supposed geometry: BB from the NS is Comptonized by a corona around. Nevertheless, the effect of geometry should be evaluated, since the actual source configuration may be deviated from this simplified one. For that purpose, we also applied `compPS` with a slab geometry to the spectra of Aql X-1 (Obs-D3 and D5), and found that the spectra are equally reproduced, while τ systematically increases by only $\sim 10\%$, and $T_{\rm e}$ decreases by $\sim 30\%$. The ambiguity of this amount does not affect our following discussion.

Thanks to the trio instruments of *Suzaku*, $T_{\rm e}$ and τ have been successfully constrained, essentially in all the data sets (even including those without GSO detection). They depend on $L_{\rm x}$ just in opposite ways, because $T_{\rm e}$ decreases towards higher $L_{\rm x}$ while τ increases, although we should be careful of possible uncertainty in the absolute values ($\sim 10\%$ in τ and $\sim 30\%$ in $T_{\rm e}$) by geometrical effects discussed above. The decrease of $T_{\rm e}$ can be explained in terms of stronger Compton cooling by the seed photons. Furthermore, the $L_{\rm x}$-$T_{\rm e}$ plot clearly shows the difference between the soft state and the hard state. The values of $T_{\rm e}$ in the hard state, including those of the initial phase of the transition (Obs-R1), are all kept in the range of $\gtrsim 10$ keV, while those of the soft state are much lower as < 4 keV.

Let us next examine $L_{\rm x}$-dependence of the optical depth τ. As the luminosity decreases from $\sim 10^{37}$ erg s^{-1} to $\sim 10^{32}$ by ~ 5 order of magnitude, τ was observed to decrease only by one order of magnitude (figure 6.3). (As discussed above, these re-

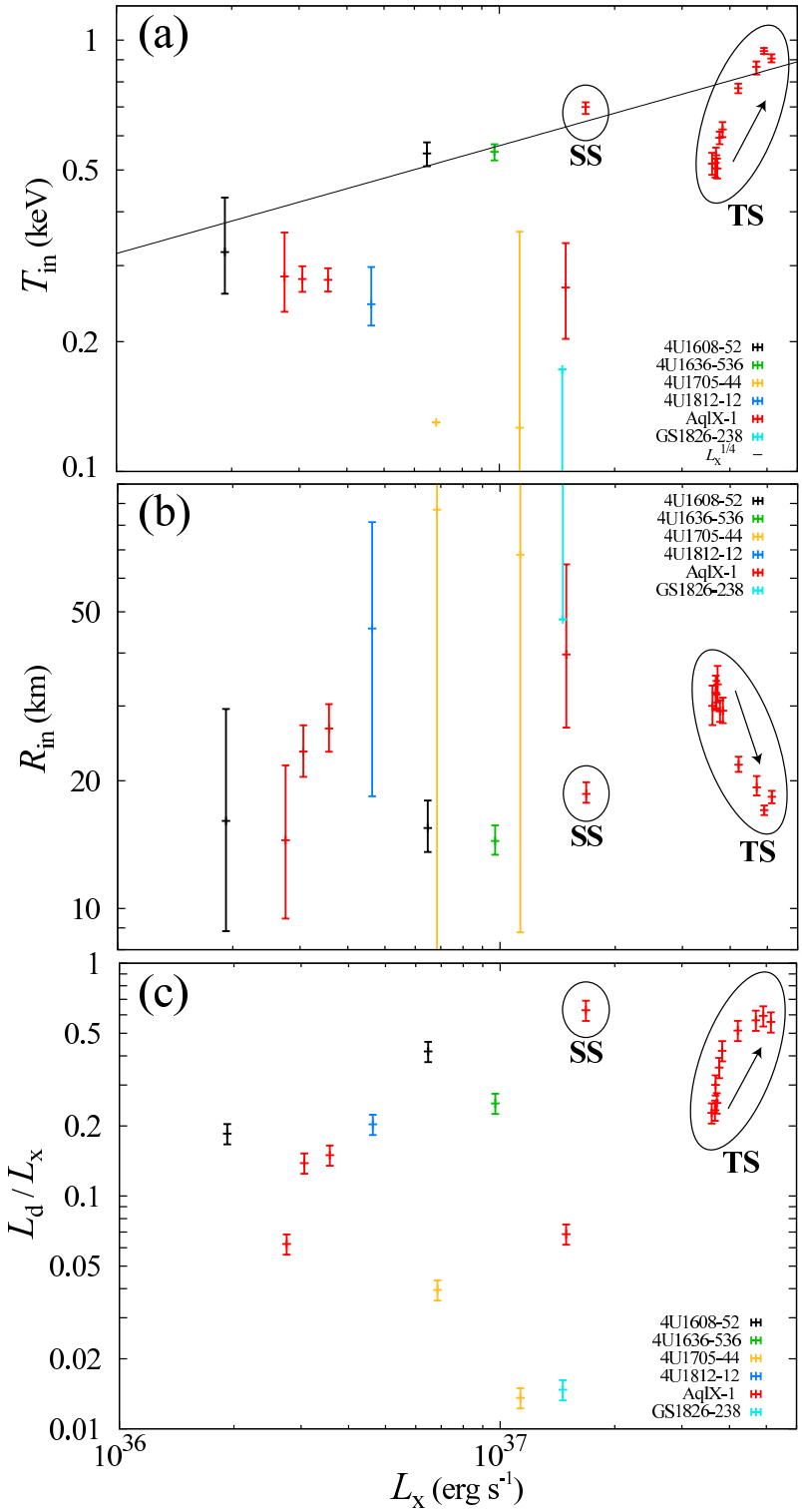

Figure 6.2: The same as figure 6.1, but for the optically-thick disk parameters. The panels show the L_x-dependence of T_{in} (panel a), R_{in} (panel b), and the fractional luminosity (L_d/L_x; panel c). The errors of L_d are taken as 10%, for reference. The straight line in panel (a) represents the prediction for a standard accretion disk with $R_{in} \sim R_{NS}$.

sults are not strongly affected by the Comptonization modeling uncertainties.) This is puzzling, because τ should be directly proportional to the coronal density, and hence to the luminosity (assuming insignificant mass outflows), as long as the flow geometry remains similar. Therefore, we infer that the flow geometry must be changing. More specifically, we are left with three possibilities. One is that the corona develops in radial direction towards lower $L_{\rm x}$, to partially cancel the density decrease. Another is that the flow becomes more Keplerian-like as $\dot{M}$ decreases, so that the corona's radial velocity decreases. The other is that the flow cross-section gets smaller as the source becomes dimmer. Further evaluation of these possibilities are carried out in §6.2.3.

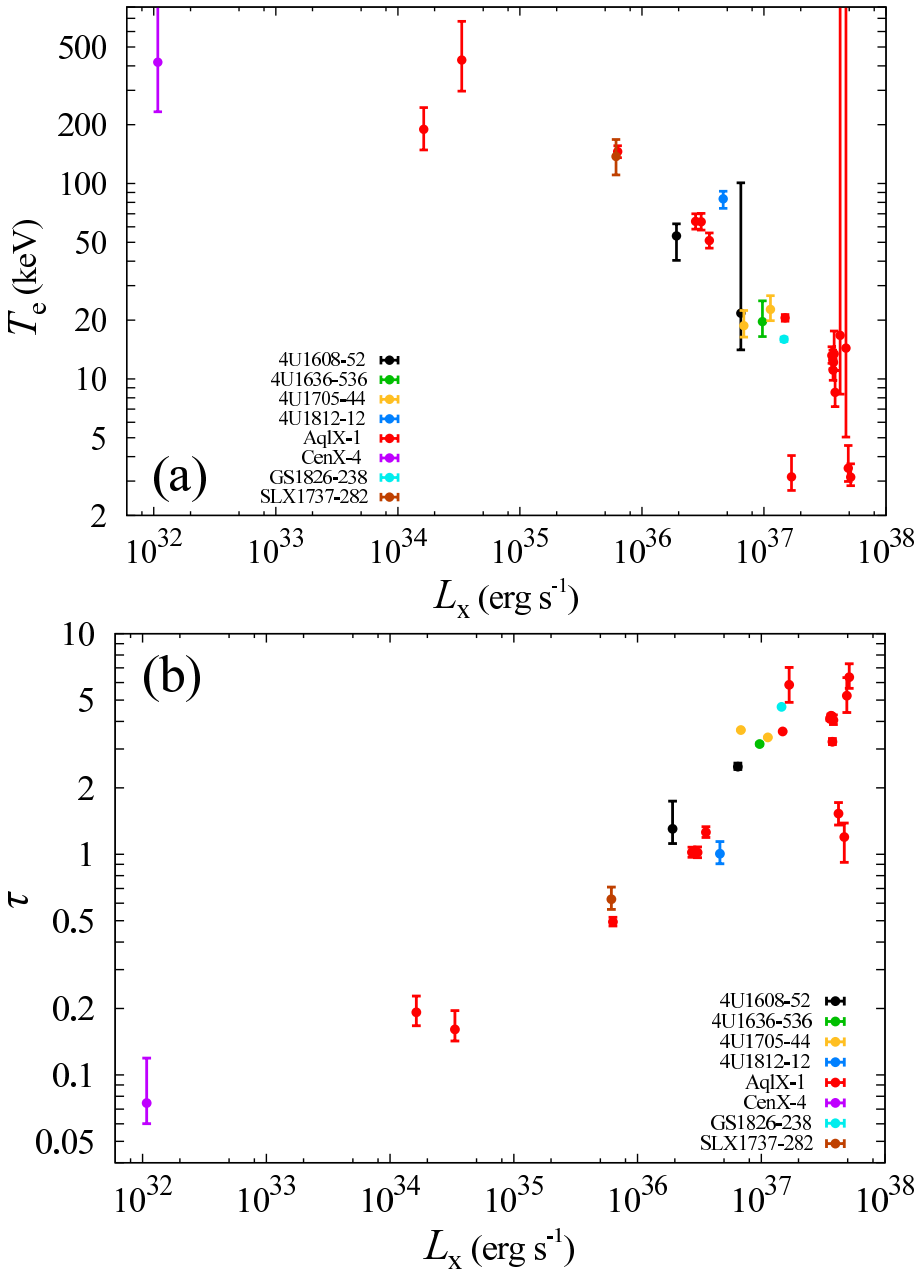

Figure 6.3: The coronal electron temperature (T_e: panel a) and optical depth (τ: panel b), shown as a function of L_x in the same way as figure 6.1 and figure 6.2.

6.1.4 A new parameter $Q = T_e/T_s$

As shown so far, the dependence of the spectral parameters on L_x has one problem that the relation is not one-to-one in many cases. This is because the high-L_x end of the hard state overlaps with low-L_x end of the soft state, as a result of the hysteresis effects. A possible solution to this problem has been proposed by Makishima (2014), hereafter M14.

As revealed so far, the soft-to-hard transition is characterized mainly by a drop in $T_{\rm e}$ and an increase in $T_{\rm bb}$. This has led M14 to propose a new parameter,

$$Q \equiv T_{\rm e}/T_{\rm s} \ , \tag{6.1}$$

where $T_{\rm s}$ is the seed photon temperature which is identical to $T_{\rm bb}$ in most cases. By definition, Q should be larger than 1. As shown in figure 6.4 (a), the values of Q calculated for all our sample objects span a wide range from ~ 1 to $\sim 10^4$, in a strong anti-correlation with $L_{\rm x}$. Furthermore, the soft-state and hard-state data points are separated in a clean way at $Q < 5$ and $Q > 5$, even though they are mixed up in $L_{\rm x}$. In other words, Q can be used as an ideal "state indicator".

Historically, the process of thermal Comptonization has been described mainly in terms of the y-parameter, which is a combination of $T_{\rm e}$ and τ (see below). However, the process also involves $T_{\rm s}$ as the third parameter. Therefore, it must be much better described, if the pair (Q, y) is used instead of y alone. To deal with a case of relatively low Q, let us redefine the y-parameter as

$$y = \frac{4k(T_{\rm e} - T_{\rm s})}{m_{\rm e}c^2}\tau(1 + \tau/3) \ , \tag{6.2}$$

in contrast to the conventional definition in which $T_{\rm e} - T_{\rm s}$ is approximated by $T_{\rm e}$.

With these preparations, we have plotted all the data sets on a "(Q, y) diagram", which is shown in figure 6.4 (b). The plot reveals the following three facts of very high importance.

1. The soft and hard states are again clearly separated at $Q \sim 5$.
2. Essentially all the data points line up on a single locus on this diagram. This demonstrates that LMXBs form a 1-parameter family which is controlled mainly by $\dot{M}$.
3. The state transition involves no discontinuity in the locus. During a transition, a source moves very quickly, but smoothly, along it.

In $1 < Q < 10$, the two quantities vary in an approximate proportionality, as indicated by a dotted line in panel (b). Above $Q = 20$, in turn, y starts to decrease with Q. This is caused by a combination of $T_{\rm bb}$ and τ, both of which decrease with $L_{\rm x}$.

6.1.5 Luminosity balance

We have seen the behavior of the three ingredients: the BB on the NS surface (§6.1.1), the disk emission (§6.1.2), and the Comptonizing corona (§6.1.3). In addition to their

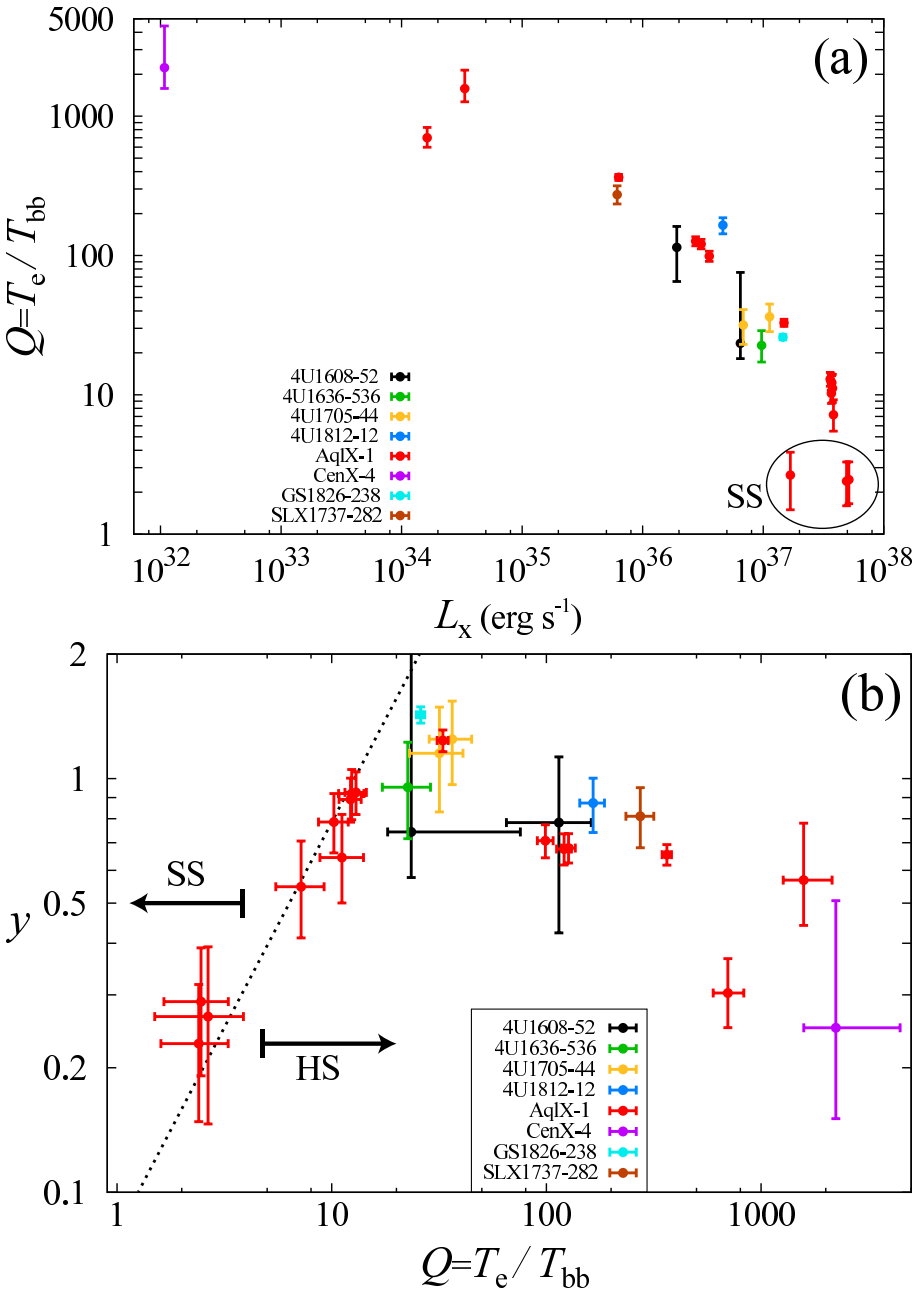

Figure 6.4: (a) The new parameter $Q \equiv T_e/T_{bb}$, shown as a function of L_x. (b) The y-parameter (see text) plotted against Q. The dotted line represents a relation of $y \propto Q$. The SS and HS means the soft state and the hard state, respectively.

individual parameters, their luminosities are also important in terms of energetics. As a representative, figure 6.5 shows a luminosity budget of Aql X-1 in the decaying phase (Obs-D1 to D7). Since these luminosity fractions are independent of the source distance, they are free from its uncertainty and only have a small statistical error of $\lesssim$ a few %. As shown in the figure, the disk ($L_{\rm d}$: blue) is the leading radiator in the soft state ($L_{\rm x} > 10^{37}$ erg s^{-1}), with a $\sim 50\%$ share as expected from the virial therem, while the corona ($L_{\rm c}$: orange) plays a major role in the hard state with $L_{\rm x} < 10^{37}$ erg s^{-1}. Throughout the whole luminosity range of 10^{34} erg s^{-1} $< L_{\rm x} \lesssim 10^{37}$ erg s^{-1} , the fraction of $L_{\rm bb}$ falls behind the other two, taking a value of $\sim 30\%$. This is however puzzling for the following reason: while half the gravitational energy release from infinity to $R_{\rm in}$ is radiated as $L_{\rm d}$, the remaining half, plus all the energy release from $R_{\rm in}$ to $R_{\rm NS}$, should be mostly brought onto the NS surface and radiated therein as $L_{\rm bb}$, because the corona is considered to have low radiation efficiency.

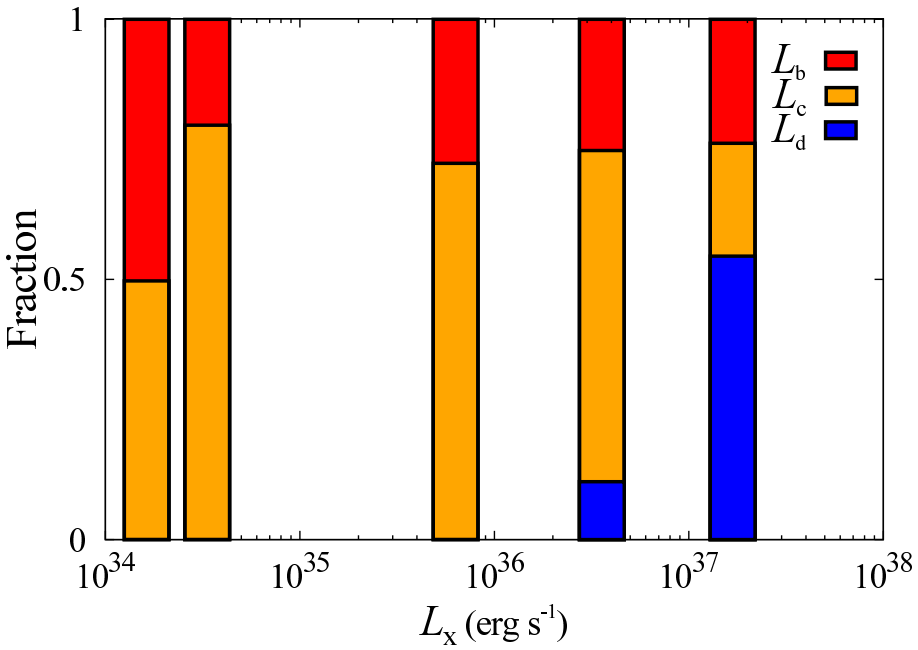

Figure 6.5: A luminosity balance of Aql X-1 during the decaying phase (Obs-D1 to D7) plotted against $L_{\rm x}$. Results of Obs-D2 and Obs-D4 are omitted here, because they are essentially the same as Obs-D3.

6.1.6 Problems to be solved

Above investigations of the $L_{\rm x}$-dependence of the emission components have left us with the following three questions:

1. Is the decrease of $R_{\rm bb}$ towards lower $L_{\rm x}$ (figure 6.1b) real, or an artifact due to color hardening?

2. At $L_{\rm x} < 0.01 L_{\rm edd}$, the value of τ decreases only by ~ 1 order of magnitude even though $L_{\rm x}$ drops by ~ 3 orders. What is the origin of this bahavior of τ?

3. The fraction of $L_{\rm bb}$ in $L_{\rm x}$ is significantly smaller than 50% (figure 6.5). This should be explained in terms of energetics of the basic accretion process.

These problems are addressed in the next section (§6.2).

6.2 Accretion Flows

In this section, let us compile the trilogy in §6.1, in order to further examine a picture of the accretion flows. In particular, we attempt to solve the three remaining issues (§6.1.6).

6.2.1 Overview

Unlike in black hole binaries, matters in an LMXB can release their remaining energy as the BB emission after landing on the NS (assuming negligible kinetic energy losses into outflows or jets, or $\eta \sim 1$ in equation 4.1). Figure 6.6 illustrates the energy budget in an LMXB under that assumption, where one proton falling from infinity to $r = R_{\rm NS}$ should release a gravitational energy of

$$E_0 = \frac{GM_{\rm NS}m_{\rm p}}{R_{\rm NS}} = 200 \text{ MeV}. \tag{6.3}$$

On the way to the NS surface, the proton first passes through the accretion disk. Until the matter reaches the inner disk edge ($r = R_{\rm in}$), it should have lost (radiated) half its gravitational energy $GMm_{\rm p}/2R_{\rm in}$ (§2.2.2), with the help of electrons.

At $r = R_{\rm in}$, the corona inherits from the disk an energy of $\frac{1}{2}\frac{GM_{\rm NS}m_{\rm p}}{R_{\rm in}}$ per proton, and further acquires $GM_{\rm NS}m_{\rm p}\left(\frac{1}{R_{\rm NS}} - \frac{1}{R_{\rm in}}\right)$. This energy is divided into five forms;

(i) Kinetic energy in the azimuthal rotation.

(ii) That in the radial infall motion.

(iii) Thermal (internal) energies of protons and electrons.

(iv) Radiative energy loss mainly from protons to electrons, and finally into photons via Comptonization.

(v) Non-radiative energy channels.

Among them, (i)+(ii)+(iii) are ultimately brought onto the NS surface, and radiated as the BB. In this section, we mainly focus on the Comptonizing corona, and try to understand the energy budget among (i) through (v).

6.2.2 Thermal energy

As described in §6.2.1, some portion of the gravitational energy of the accreting matter can be converted to thermal energies of protons and electrons, namely, (iii) above. In the

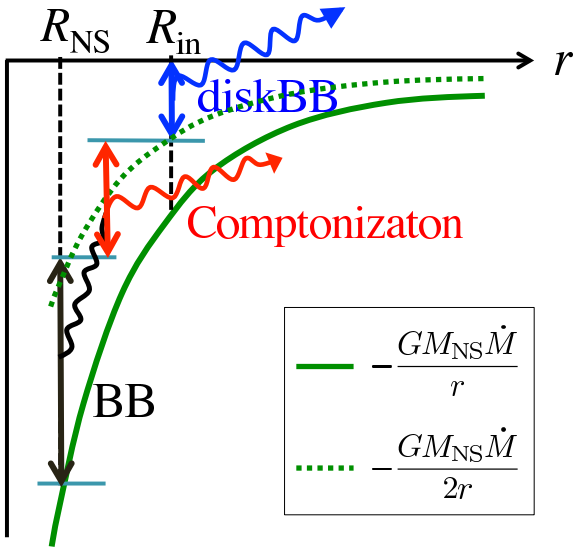

Figure 6.6: A schematic diagram of the energetics in an LMXB.

standard accretion disk, this (iii) can be neglected, because the high radiation efficiency therein converts (iii) to (iv), to achieve $T_{\rm in} \lesssim 1$ keV which is much lower than equation 6.3. In the corona in contrast, the gained thermal energy can be retained until the NS surface due to its low density and inefficient radiation.

Below, let us evaluate (iii) quantitatively, employing the Aql X-1 (Obs-D3) result as a representative. In terms of electron energetics in the Comptonizing corona, the heating is caused by Coulomb collisions with protons and cooling by Compton scatterings with BB photons. Assuming that the corona is isothermal, the former is written as

$$\begin{aligned} Q^+ &= 3\nu_{\rm E} k (T_{\rm p} - T_{\rm e}) \\ &= 2.8 \times 10^{36} \left(\frac{\tau}{1.0}\right)^2 \left(\frac{R_{\rm c}}{30\ {\rm km}}\right) \left(\frac{T_{\rm e}}{50\ {\rm keV}}\right)^{-3/2} \left(\frac{T_{\rm p}}{150\ {\rm MeV}}\right)\ {\rm erg\ s^{-1}}, \end{aligned} \quad (6.4)$$

where $\nu_{\rm E} \propto n_{\rm e} T_{\rm e}^{-3/2}$ is the Coulomb coupling, $T_{\rm p}$ is the proton temperature, and $R_{\rm c}$ is the coronal radius which is assumed to be $\sim R_{\rm in} \sim 30$ km. The cooling is expressed as

$$Q^- = L_{\rm bb} y = L_{\rm bb} \frac{4kT_{\rm e}}{m_{\rm e}c^2} \tau \quad ({\rm for}\ \tau \leq 1). \quad (6.5)$$

By equating them ($Q^+ = Q^-$), we obtain

$$T_{\rm p} = 21 \left(\frac{\tau}{1.0}\right)^{-1} \left(\frac{R_{\rm c}}{30\ {\rm km}}\right)^{-1} \left(\frac{T_{\rm e}}{50\ {\rm keV}}\right)^{5/2}\ {\rm MeV}. \quad (6.6)$$

Using equation 6.6 and the values in table 5.3, the proton temperature is estimated as $T_{\rm p} \sim 20$ MeV. Thus, the protons are strongly cooled by photons, with the electrons as

a catalyst. Although the above calculation approximates the corona as a uniform single zone, the result does not change very much even if more properly considering the radial density gradient.

The estimate of $T_{\rm p}$ allows us to quantify the vertical coronal thickness. Assuming $T_{\rm p}$ to be constant in the coronal z-direction (perpendicular to the disk plane), the force balance in the z-direction is expressed as

$$\frac{dp_{\rm g}}{dz} \simeq -\frac{GM_{\rm NS}\rho}{r^2}\frac{z}{r}, \tag{6.7}$$

where ρ is the density therein. Eliminating ρ with the help of $p_{\rm g} = (\rho/m_{\rm p})kT_{\rm p}$, we obtain

$$p_{\rm g}(r,z) = p_{\rm g}(r,0)\exp\left(-\frac{z^2}{2H^2}\right), \tag{6.8}$$

where

$$\frac{H(r)}{R_{\rm NS}} = \sqrt{\frac{kT_{\rm p}}{E_0}}\left(\frac{r}{R_{\rm NS}}\right)^{3/2} \tag{6.9}$$

is the vertical scale height of the corona. Using $kT_{\rm p} \sim 20$ MeV, the scale height at $r = R_{\rm NS}$ is estimated as $H/R_{\rm NS} \sim 0.3$. Thus, the gas pressure can inflate the disk relatively thick, at least in the sense of order-of-magnitude estimate.

6.2.3 Kinetic energy

Now that the thermal energy was found relatively small, the flow velocity becomes very important when trying to understand the energetics, and in particular, to solve the 2nd problem (the non proportionality between τ and $L_{\rm x}$) listed in §6.1.6. In contrast to the case of a standard accretion disk, we need to consider both the radial velocity v_r and the rotational velocity v_ϕ ($\lesssim \sqrt{GM_{\rm NS}m_{\rm p}/r} \equiv$ Keplerian).

As already described in Sakurai et al. (2014), the mass continuity of the corona requires

$$\dot{M} \;=\; S(r)v(r)\rho(r) = S(r)v(r)\mu m_{\rm p} n_{\rm e}(r), \tag{6.10}$$

where r is the distance from the NS center, S is a cross-section of the flow ($= 4\pi r^2$ if spherical), v is the radial velocity, $\mu \sim 1.2$ is the mean molecular weight of ions, and $n_{\rm e}$ is the electron number density. Assume that the flow has a self-similar shape and the

radial velocity is a certain fraction of the free-fall value as

$$S(r) = S_0 \left(\frac{r}{R_{\rm NS}}\right)^2 \quad \text{and} \quad v(r) = g v_{\rm ff} \left(\frac{r}{R_{\rm NS}}\right)^{-1/2}, \tag{6.11}$$

where $v_{\rm ff} = \sqrt{2GM_{\rm NS}/R_{\rm NS}}$ is the free-fall velocity and $g < 1$ is a dimensionless constant which becomes $\ll 1$ when the flow is Keplerian-like. Then, equation 6.10 yields

$$n_{\rm e}(r) \;=\; \frac{\dot{M}}{\mu m_{\rm p} g S_0 v_{\rm ff}} \left(\frac{r}{R_{\rm NS}}\right)^{-3/2}. \tag{6.12}$$

The optical depth is obtained by integrating equation 6.12 from $r = R_{\rm NS}$ to the outer coronal radius $R_{\rm c}$ as

$$\tau \;=\; \frac{2\sigma_{\rm T}\dot{M}R_{\rm NS}}{\mu m_{\rm p} g S_0 v_{\rm ff}} \left(1 - \sqrt{\frac{R_{\rm NS}}{R_{\rm c}}}\right), \tag{6.13}$$

where $\sigma_{\rm T}$ is the Thomson cross-section. This provides the quantitative description of the discussion made in §6.1.3. In equation 6.13, the last factor can be approximated as unity by assuming $R_{\rm c} \gg R_{\rm NS}$. Thus, we can rule out the 1st possibility (i.e. radial expansion of the corona) invoked in §6.1.3 to explain the puzzling behavior of τ.

As $\dot{M}$ is replaced with $L_{\rm x}$ using equation 4.1, finally S_0 is written as

$$g\eta S_0 \;=\; \left(\frac{4\sigma_{\rm T}R_{\rm NS}}{\mu m_{\rm p} v_{\rm ff}^3}\right)\frac{L_{\rm x}}{\tau} = 18.5 \left(\frac{L_{\rm x}}{10^{36}\ {\rm ergs^{-1}}}\right)\tau^{-1}\ {\rm km}^2 \tag{6.14}$$

or in terms of radius R_0 of the flow impact region on the NS surface as

$$\sqrt{g\eta}R_0 \;=\; \sqrt{\frac{g\eta S_0}{4\pi}} = 1.2\sqrt{\left(\frac{L_{\rm x}}{10^{36}\ {\rm ergs^{-1}}}\right)\tau^{-1}}\ \ {\rm km} \tag{6.15}$$

where η is the conversion efficiency from the gravitational energy to radiation ($0 < \eta \leq 1$; equation 4.1). Thus, the observed non-proportionality between τ and $\dot{M}$ indicates that either η, g, or R_0 should decrease as the source gets fainter. This provides a quantitative expression to the ideas mentioned in §6.1.3.

Returning to the actual data, the quantity $\sqrt{g\eta}R_0 = 1.2\sqrt{L_{\rm x}/\tau}$ is plotted in figure 6.7 against $L_{\rm x}$. First, let us focus on the region of 10^{36} erg s^{-1} $< L_{\rm x} \lesssim 10^{37}$ erg s^{-1} , where the quantity is saturated at ~ 2 km. These data points just correspond to those which have $R_{\rm bb} \sim 10$ km in figure 6.1 (b). Hence, assuming a natural identification of $R_0 = R_{\rm bb}$, the coefficient should be $g\eta \sim 0.04$. Further assuming that most of the gravitational energy is totally radiated ($\eta \sim 1$), the flow radial velocity should be so small as $v_r \sim 0.04 v_{\rm ff}$. Since $\frac{1}{2}m_{\rm p}v_r^2 \sim 0.3$ MeV, the total kinetic energy, estimated as

~ 100 MeV $-kT_{\rm p} \sim 80$ MeV, is mainly carried by rotation ($v_r \ll v_\phi$). In other words, the data indicates that the corona is still rapidly rotating, and the gravity is mostly counter-balanced by the centrifugal force.

Next, looking at the regime of $L_{\rm x} < 10^{36}$ erg s^{-1} in figure 6.7, as expected, the quantity $\sqrt{g\eta}R_0$ clearly decreases as $L_{\rm x}$ does. Then, is this decrease carried by the flow radius R_0, or the normalized radial velocity g? Importantly, the dependence, approximated as $L_{\rm x}^{0.24}$, coincides well with that of $R_{\rm bb}$ in figure 6.1 (b). Therefore, the decrease of R_0 is more likely, because this single assumption can simultaneously explain the two phenomena, the decrease of $R_{\rm bb}$ and the behavior of $L_{\rm x}/\tau$. In other words, it would be too artificial to assume that a BB color hardening and a decrease in g happened to make the apparent value of $R_{\rm bb}$ and the quantity $\sqrt{g\eta}R_0$ depend in the same way on $L_{\rm x}$. We have thus obtained an answer to the 1st problem identified in §6.1.6.

At $L_{\rm x} < 10^{35}$ erg s^{-1}, the values of $\sqrt{g\eta}R_0$ becomes smaller than those expected from the relation $\propto L_{\rm x}^{0.24}$, by $\sim 30\%$ in Aql X-1 Obs-D6−7 and $\sim 70\%$ in Cen X-4. This can be, for example, explained by a change of the flow shape. We assumed in equation 6.11 that $S(r)$ scales as $\propto r^2$, which corresponds to a conical shape. If the flow is more strongly spread as $S \propto r^p$ with $p > 2$, equation 6.15 would overestimate the true radius by a factor of $\sqrt{2p-3}$. For instance, $S(r) \propto r^{2.5}$ can decrease R_0 by $\sim 30\%$, explaining the discrepancy in those of Aql X-1 Obs-D6−7.

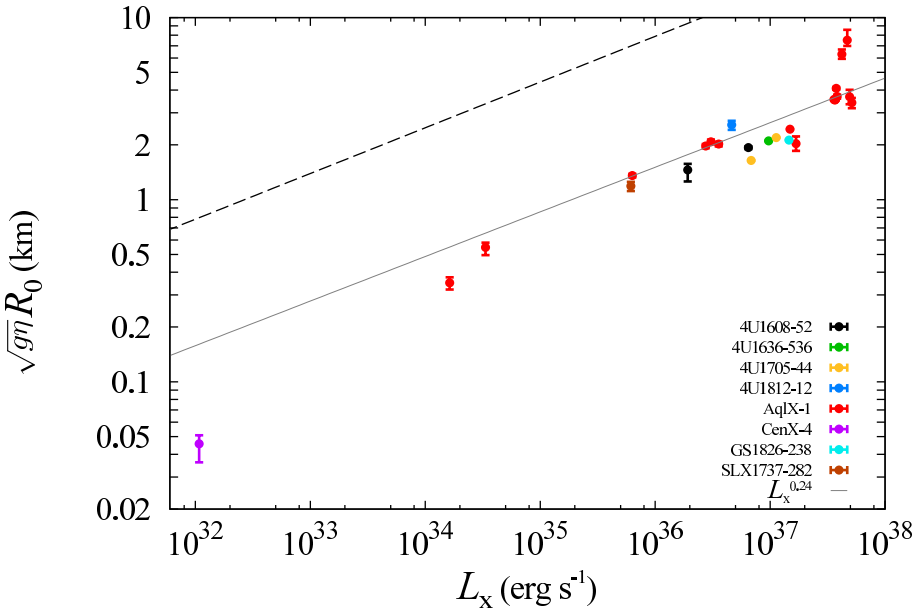

Figure 6.7: The estimated coronal flow radius ($\sqrt{g\eta}R_0 \sim \sqrt{L_{\rm x}/\tau}$) versus $L_{\rm x}$, calculated via equation 6.15 for all the sources analyzed. The solid line represents a relation $\propto L_{\rm x}^{0.24}$ with an arbitrary normalization, while the dashed line is the best fit to figure 6.1(b).

6.2.4 Possible emergence of a magnetosphere

Given that the decrease of $\sqrt{g\eta}R_0$ is due to that of R_0 (and of $R_{\rm bb}$ too), the flow should be somehow funneled when $L_{\rm x}$ decreases. In order to explain this, the emergence of a magnetosphere is one of the possible solutions. The effects of magnetic fields, which we have so far neglected, can be signicant under such a low mass accretion rate. The effects can be represented by the Alfven radius, namely, the gravity vs magnetic pressure balance point, defined as

$$R_{\rm A} = 6.8\times10^3\left(\frac{\dot{M}}{10^{-10}\ M_\odot/{\rm yr}}\right)^{-2/7}\left(\frac{B}{10^{12}\ {\rm G}}\right)^{4/7}\ {\rm km} \tag{6.16}$$

$$\sim 7\times10^3\left(\frac{L_{\rm x}}{10^{36}\ {\rm ergs}^{-1}}\right)^{-2/7}\left(\frac{B}{10^{12}\ {\rm G}}\right)^{4/7}\ {\rm km}, \tag{6.17}$$

where $\eta = 1$ is again used. Assuming a magnetic field of $B \sim 10^7$ G, for instance, we obtain $R_{\rm A} \lesssim 10$ km at $L_{\rm x} > 10^{36}$ erg s^{-1} . In such cases, the magnetic fields would have no influence on the accreting matter.

At lower luminosities of $L_{\rm x} < 10^{36}$ erg s^{-1} in contrast, the magnetic pressure, which does not depend on $\dot{M}$, can thus overwhelm the gravitational gas pressure which scales approximately as $\propto \dot{M}$. Then the matters should fall along $\vec{B}$, and the flow is funneled onto the NS magnetic poles. This hypothesis of the magnetosphere emergence is independently pointed out by Matsuoka & Asai (2013), which is described later in §6.4.3. Moreover, as $L_{\rm x}$ further decreases, the flow may spread at larger r, and shrink toward $r \to R_{\rm NS}$, as pointed out in the last paragraph of §6.2.4. This may reflect the shape of the (dipole) magnetic field around the NS.

Equation 6.16 gives only a course criterion to judge the relative dominance of the gravity and the magnetic pressure. Thus, even at $L_{\rm x} \gtrsim 0.01L_{\rm edd}$, the magnetic field can have some effects on the accretion flow. For example, the field possibly works to support the coronal geometrically thick, although the effect should be local (only around the NS) because the magnetic pressure rapidly decreases with radius as $\propto r^{-6}$.

6.2.5 Total energetics

Based on the arguments in §6.2.2 and §6.2.3, we may now discuss the entire energetics of the accretion flow in the hard state. In the corona, the flow was found to have a relatively small thermal energy as ~ 20 MeV, and the radial infall velocity is also small as $v_r \sim 0.04v_{\rm ff}$. Therefore, as described in §6.2.3, most of the energy is carried by v_ϕ; namely, the motion should be close to the Keplerian. This implies that the gravitational energy which the flow gained in $r < R_{\rm in}$ (i.e. in the corona), plus half the energy from

infinity to $R_{\rm in}$, is equally distributed to the Comptonization, and that brought onto the NS surface. The latter will be thermalized to power $L_{\rm bb}$, but this contradicts to the observed luminosity balance in figure 6.5 which dictates $L_{\rm bb} < L_{\rm c}$ and $L_{\rm bb} < 0.5L_{\rm x}$. Therefore, we should examine mainly two possibilities. One is that more than half the gravitational energy is actually fed to the NS, but is not fully radiated as BB, with the rest escaping into some other channels. The other is that the protons can somehow lose more energy until it reach the NS, so that the condition $L_{\rm bb} > 0.5L_{\rm x}$ is not always necessary.

6.2.6 Escape into other channels

As the first class of scenarios, we here examine three candidates. One is that the some hidden emission from the NS surface carries away a considerable fraction of the thermalized energy. For instance, in Aql X-1 Obs-D5, the BB emission area is only half the NS surface as $4\pi R_{\rm bb}^2 = 4\pi(7\ {\rm km})^2 \sim 0.5 \times 4\pi(10\ {\rm km})^2$, so that another low-temperature BB is possibly present there. However, when another BB is added in the $\rm C_b$ fit (figure 5.10) with $T_{\rm bb}$ left free and $R_{\rm bb} = 7$ km fixed, $T_{\rm bb}$ has an upper limit of 0.2 keV. Hence, $L_{\rm bb}$ can be increased only by $\sim 6\%$, which is insufficient to solve the discrepancy.

Another candidate is that some portion of the proton energies after their landing adds to the rotational energy of the NS. Since the NSs in LMXBs are known to spin rapidly with a frequency of $f \sim$ several hundred Hz, a fraction of the final energy of a proton,

$$\frac{1}{2} m_{\rm p} (R_{\rm NS}\omega)^2 = 5.2 \left(\frac{f}{500\ {\rm Hz}} \right)^2\ {\rm MeV}, \tag{6.18}$$

can be kept as a rotational energy. This is however not sufficient to reduce the apparent $L_{\rm bb}$ significantly, because Aql X-1 is considered to have $f = 550.27$ Hz (Casella et al. 2008). Although we assumed above that f is kept constant under the accretion, in reality f may increase (i.e., the NS will spin up) if the protons can transfer their angular momentum to the NS. For example, the coronal flow may be caught by the magnetic field lines (§6.2.4) at a certain distance from the NS. Then, their rotational motion, which was nearly Keplerian, may be suddenly decelerated, so that they will make a quasi-soft-landing on the NS surface. Assuming that this angular-momentum transfer occurs at $\sim R_{\rm NS}$, and that the BB luminosity is just $L_{\rm bb} = GM_{\rm NS}\dot{M}/2R_{\rm NS}$ (i.e., 50% of equation §6.3). the torque exerted to the NS becomes

$$T = \dot{M}\sqrt{GM_{\rm NS}R_{\rm NS}} = 2L_{\rm bb}R_{\rm NS}^{3/2}/\sqrt{GM_{\rm NS}}\ . \tag{6.19}$$

Equating this with $2\pi I \dot{f}$ with $I = 10^{45}$ g cm^2 the canonical moment of inertia of an NS,

we obtain the expected spin-up rate as

$$\dot{f} = 2.2 \times 10^{-14} \left(\frac{L_{\rm bb}}{10^{36}\ {\rm ergs}^{-1}} \right) \ \ {\rm Hz\ s}^{-1} \simeq 6.7 \times 10^{-10} \ \ {\rm kHz\ yr}^{-1}\ . \tag{6.20}$$

This means that the NS can be spun up significantly in about 1/10 of the Hubble time, in agreement with general evolutionary story of LMXBs. Observationally, the LMXB IGR J00291+5934 (known as AMXP; see §6.4.3) has a spin frequency of ~ 600 Hz and a period change rate of $\sim 10^{-13}$ Hz s^{-1} (Burderi et al. 2007), which is of the same order as equation 6.20. Thus, the missing energy can possibly be consumed to spin up the NS.

6.2.7 $L_{\rm bb} < 0.5 L_{\rm x}$ in reality

The other class of scenarios that the protons in the corona lose more than half the gravitational energy, might be realized in some ways as follows. Since the electron as well as proton rotates rapidly as $\sqrt{GM/R_{\rm NS}} \sim 0.5$c, not only thermal but also bulk Comptonization can be contributing the hard spectrum (Farinelli et al. 2008; Mainardi et al. 2010). Then, the electron and the proton can further transfer their energy to the input BB photons, so that the final angular velocity may be sub-Keplerian and can result in $L_{\rm bb} < 0.5 L_{\rm x}$.

The above scenario corresponds to the idea of radiation drag (e.g. Fukue & Umemura 1994; Umemura & Fukue 1994; Mineshige et al. 1998), which considers that the photon field acts as a dissipative media, so that the protons can lose their angular momentum (via electrons) and fall inward rather efficiently. By modeling the drag force as $-\beta\vec{v}$ where β is a constant, the radial and azimuthal velocities at small r are approximately given as

$$v_{\rm r} \ = \ -2\beta r - 4\beta c_{\rm s}^2 \frac{r^2}{GM_{\rm NS}} \tag{6.21}$$

and

$$v_\phi \ = \ \sqrt{\frac{GM_{\rm NS}}{r}} - c_{\rm s}^2 \sqrt{\frac{r}{GM_{\rm NS}}}, \tag{6.22}$$

respectively (Fukue & Umemura 1994), where $c_{\rm s}$ is the sound speed. Using $c_{\rm s}^2 = \frac{5}{3} k T_{\rm p}/m_{\rm p}$, the latter is estimated to be $v_\phi \sim 0.8 v_{\rm kep}$ where $v_{\rm kep} = \sqrt{\frac{GM_{\rm NS}}{r}}$. Thus the motion can be actually sub-Keplerian, which reduces the kinetic energy to $60 - 70\%$ from the Keplerian case, and may somehow explain the small $L_{\rm bb}$. Even in this case, the condition $v_r \ll v_\phi$ is satisfied, as long as $\beta \ll 1$. The proton drag effect may be playing an important role in the LMXB corona. In fact, the matter may not be able to reach

the center, unless its energy and angular momentum are taken up by the seed photons. In other words, there is an intrinsic reason for the Compton luminosity to occupy a considerable fraction of $L_{\rm x}$.

This effect, together with the drag by the magnetic field, may take the angular momentum away from the protons. It would make the flow transonic (although dependent on β), which can create rather hot and slow (small v_r) region at smaller radii. Since true β should be strongly radius-dependent, we need more detailed calculation specific to this case to estimate accurately $v_{\rm r}$ and v_ϕ; this is beyond the scope of this thesis.

The idea of radiation drag leads us to an interesting speculation. The drag force from the seed photons is exerted to rotating electrons, and then to protons via Coulomb coupling. We hence expect electrons to become rotating slightly slower than protons. This relative motion between the two particle species will produce ring-like current in the corona, and hence magnetic fields which vertically thread the corona. As the corona rotates, the magnetic field lines must also rotate and become twisted, to launch twisted Alfven waves into the two polar directions. Some of the materials may be thus ejected in the form of jets or outflows, which may act as another mechanism of angular momentum transport from the corona. As a reaction to this process, the electric current will apply $\vec{j} \times \vec{B}$ force to the corona, in the direction opposite to the gravity, to slow down the radial infall. Further examination of this scenario is however beyond the scope of the present thesis.

6.2.8 Geometry

As a summary of the discussion conducted thus far, let us consider the flow geometry using the hints obtained. Figure 6.8 shows a schematic view of the geometry along various $L_{\rm x}$. In the soft state, the disk inner edge comes close to the NS surface and the NS equatorial zone emits the BB photons (panel a). In the hard state with $L_{\rm x} > 0.01 L_{\rm edd}$, the disk is truncated at larger radii of ~ 30 km, where the flow is transformed into the hot ($kT_{\rm p} \sim 20$ MeV) and geometriclly-thick shape (panel b). Since the BB radius of this regime equally exhibits $R_{\rm bb} \sim 10$ km, the flow is inferred to swell up so as to cover the entire NS surface. The disk thickness may be sustained by the gas pressure (§6.2.2) and possibly the magnetic pressure (§6.2.4). Due to the hysteresis effect, the luminosity can be so high as $\gtrsim 0.1 L_{\rm edd}$ when $\dot{M}$ is increasing, as confirmed in several sources (§5.3 and §5.5). In this highest-luminosoty end of the hard state, the inner part of the disk may intrude into the corona, to realize the double-seed configuration. In contrast, at the faint regime of $L_{\rm x} < 0.01 L_{\rm edd}$, the flow might be funneled by the magnetosphere (panel c), as discussed in §6.2.3 and §6.2.4. As the luminosity further decreases to $L_{\rm x} \sim 10^{-4} L_{\rm edd}$, the flow is narrowed at smaller radii (panel c'), which may reflect the field shape.

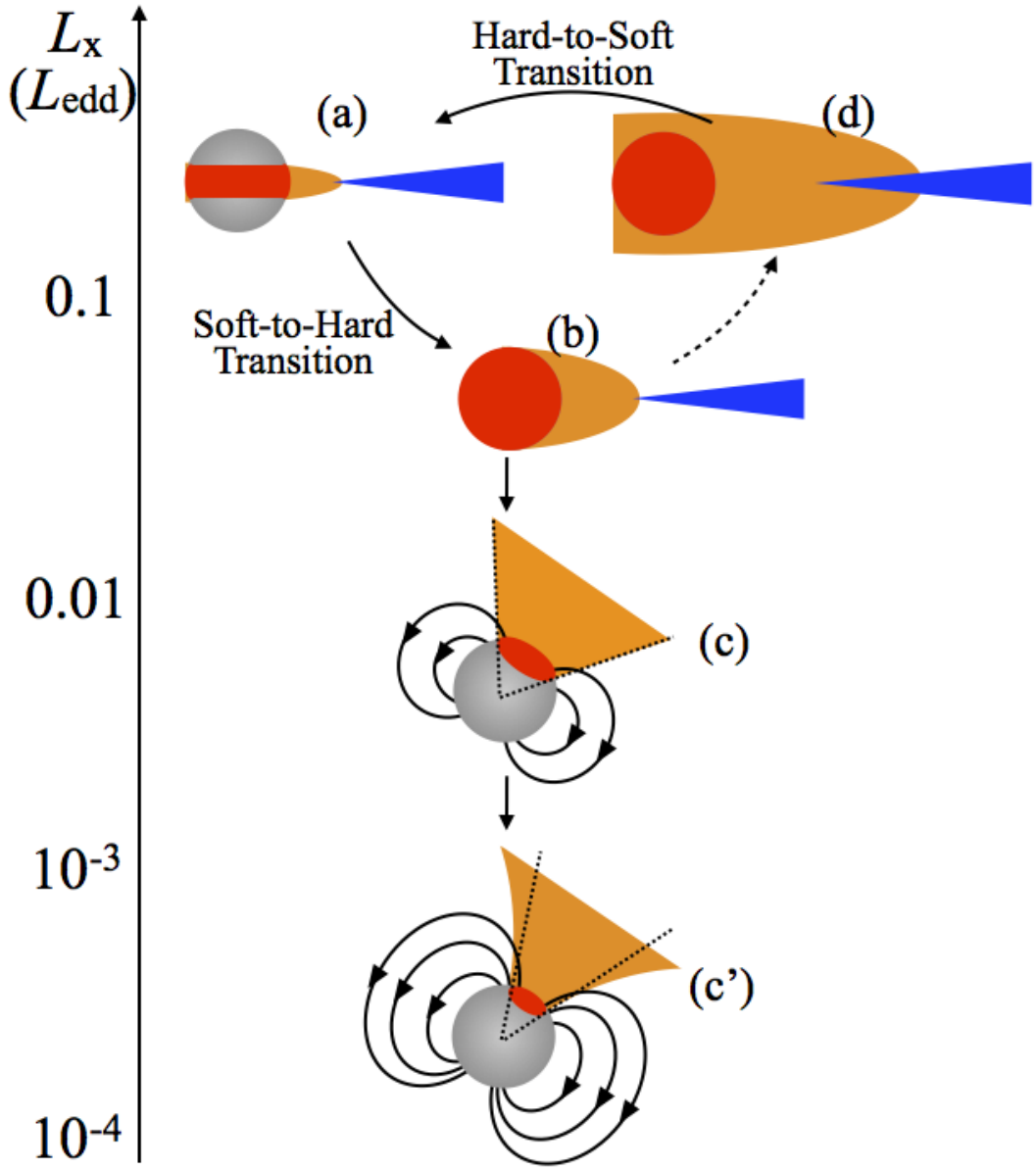

Figure 6.8: A possible sequence of $\dot{M}$-dependent changes in the accretion-flow geometry. Blue, red, and orange indicate the disk, the BB source, and the Comptonizing corona, respectively, while gray shows the NS.

6.3 Hard-to-soft state transition

The hard-to-soft state transition was seen in Aql X-1 Obs-R2 (§5.4). From the series of snap shot spectra during that precious occasion, we have confirmed that the change is continuous: $T_{\rm in}$ and $T_{\rm bb}$ increase, while $R_{\rm in}$, $R_{\rm bb}$, and $T_{\rm e}$ decrease. In reference to table 5.15 and figure 5.29, the details can be described as follows:

- $T_{\rm in}$ increased from 0.5 keV to 0.9 keV, while $R_{\rm in}$ decreased from $\sim$ 30 km to $\sim$ 18

km. Hence the disk luminosity $L_{\rm d} \propto T_{\rm in}^4 R_{\rm in}^2$ increased by a factor of ~ 4.

- The BB temperature also increased as $T_{\rm bb} = 1.0$ keV $\rightarrow 1.5$ keV, and $R_{\rm bb}$ reduced from 10 km to 5 km. Consequently $L_{\rm bb} \propto T_{\rm bb}^4 R_{\rm bb}^2$ slightly increased by $\sim 20\%$.
- In the corona, $T_{\rm e}$ significantly decreased from 13 keV to ~ 3 keV, and τ increased from ~ 4 to ~ 6. As a result, the degree of Comptonization ($y \sim T_{\rm e}\tau^2$), which is proportional to coronal luminosity $L_{\rm c}$, decreased by $\sim 50\%$.

Compiling these three results, a breakdown of the energy budget across the transition is plotted in figure 6.9 in the same format as figure 6.5. Associated with $R_{\rm in}$ decrease, the fraction of $L_{\rm d}$ approaches ~ 0.5, as predicted by the virial theorem and confirmed so far repeatedly (e.g. §6.1.2). Since that of the BB exhibits always $L_{\rm bb} < 0.5 L_{\rm x}$, the same discussion made in §6.2 can be applied to this case.

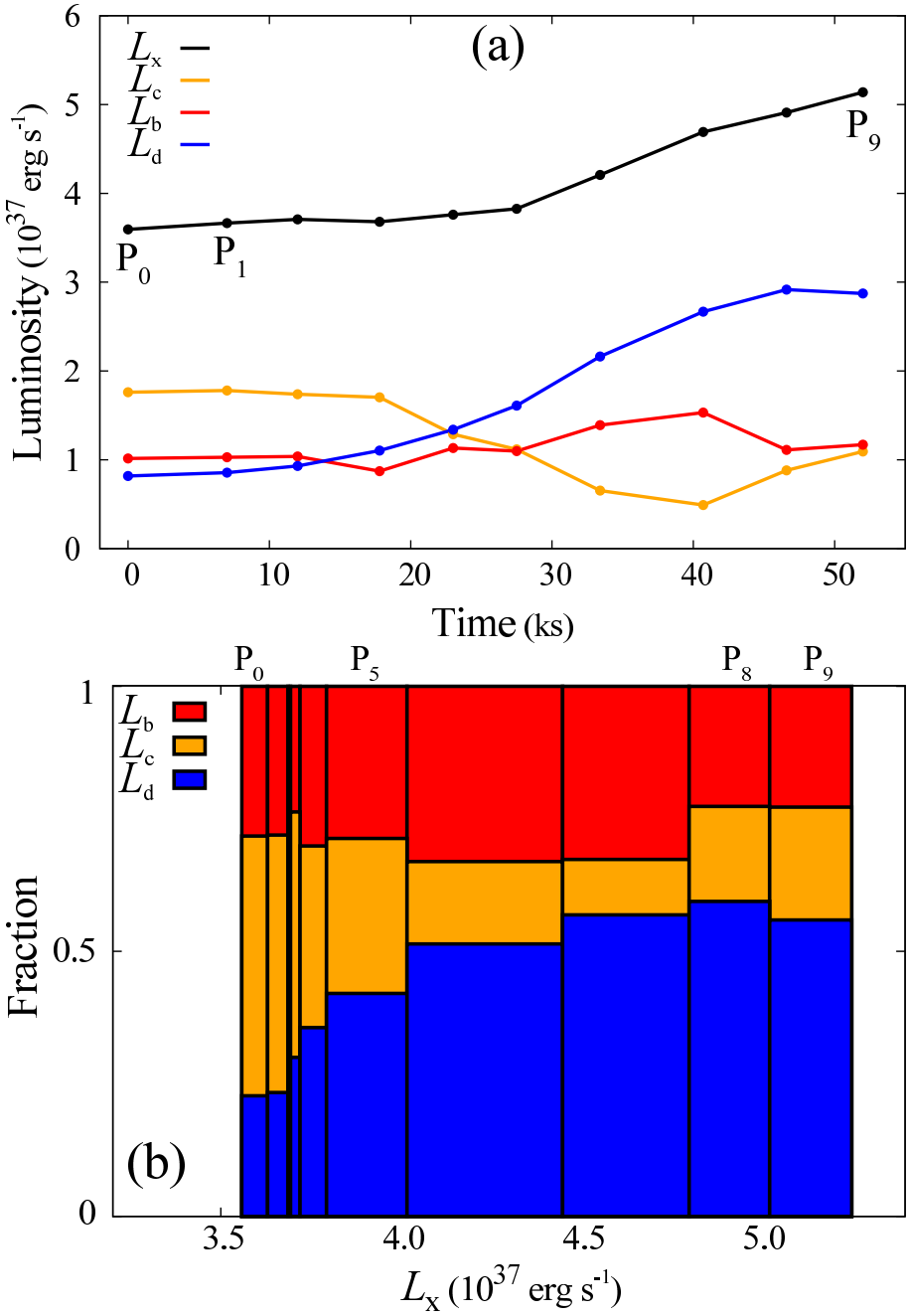

Figure 6.9: The luminosity budget during the hard-to-soft state transition in Aql X-1 Obs-R2, plotted against time (panel a) and L_x (panel b). The time origin in panel (a) is that of P_0.

6.4 Other Effects

6.4.1 Inclination

Although we have assumed for simplicity that the sample LMXBs all have the same inclination of $i = 45°$, this assumption is obviously unwarranted, and i should scatter among them. Then, how are our results affected by this scatter?

The apparent effect of i is those on the disk emission. As shown in equation 2.8, apparent flux of the disk emission depends on i as $F_{\rm d} \propto \cos i$. Since $R_{\rm in}$ is proportional to a square root of $F_{\rm d}$, its dependence on i is $\propto \sqrt{\cos i}$. Although i is usually difficult to determine, we may assume $i \lesssim 60°$ for our sample sources, because they do not usually exhibit periodic "dips" synchronized with the orbital period (cf, "dipping" sources typically have high inclination of $i \gtrsim 70°$). Hence the uncertainty in $R_{\rm in}$ is at most a factor of $\sqrt{\cos(0°)/\cos(45°)} = \sqrt{\cos(45°)/\cos(60°)} \sim 1.4$. Even considering this, the $R_{\rm in}$ values shown in figure 6.2 stay in the reasonable range of ≥ 10 km. Therefore, the uncertainty of i does not affect our overall results.

In addition to the disk emission, the Comptonized BB can be affected by i. As Makishima et al. (2008) discussed on their study of black hole binaries, sources with different i would exhibit different behavior. If the corona has a shape deviated from a sphere, the effects of Comptonization will depend on i. For instance, when we see a very oblate corona with moderate τ (e.g. ~ 1) from a high inclination ($i \sim 90°$), the optical depth will effectively get larger. Actually, it is proved by Zhang et al. (2014) that the high-inclination source 4U1915-05 exhibits a larger y-parameter ($0.50^{+0.05}_{-0.03}$) than the normal-inclination object 4U1820-30 ($y = 0.27^{+0.16}_{-0.15}$). Although the effect is difficult to estimate quantitatively, our results may be intact, because the values of τ among the multiple sources indeed do not exhibit large scatter. More exact evaluations of this geometrical effect would need detailed simulations (e.g. Odaka et al. 2011).

6.4.2 Thermo-nuclear bursts

Type-1 bursts, nemaly, thermo-nuclear flashes on the NS surface is one of the common features of LMXB, while they are in a certain luminosity range. Looking over the spectral analysis results in Chapter 5 and their light curves in Chapter 4, we can find a condition for the type-1 bursts to occur. Figure 6.10 shows burst rate of each source, where a threshold is seen around $L_{\rm x} \sim 5 \times 10^{36}$ erg s^{-1}. All the hard-state sources with $L_{\rm x} \gtrsim 5 \times 10^{36}$ erg s^{-1}, namely those introduced in §**??**, exhibited at least 1 burst during the observations, whereas none was detected from those with $L_{\rm x}$ below the threshold. Similarly, the soft-state Aql X-1 (Obs-D1) showed no burst-like features even though it

has $L_{\rm x} > 1 \times 10^{37}$ erg s^{-1}, in agreement with the general understandings (e.g. Cornelisse et al. 2003; Cumming 2004; Galloway et al. 2008). The nuclear fuel (H and He) supplied by the accreting matter will "burn" continuously without producing bursts if $L_{\rm x}$ is very high, whereas the burst rate would decrease towards lower $L_{\rm x}$ because the burst intervals (in which the matter should accumulate to exceed a certain threshold of ignition) must get longer and longer.

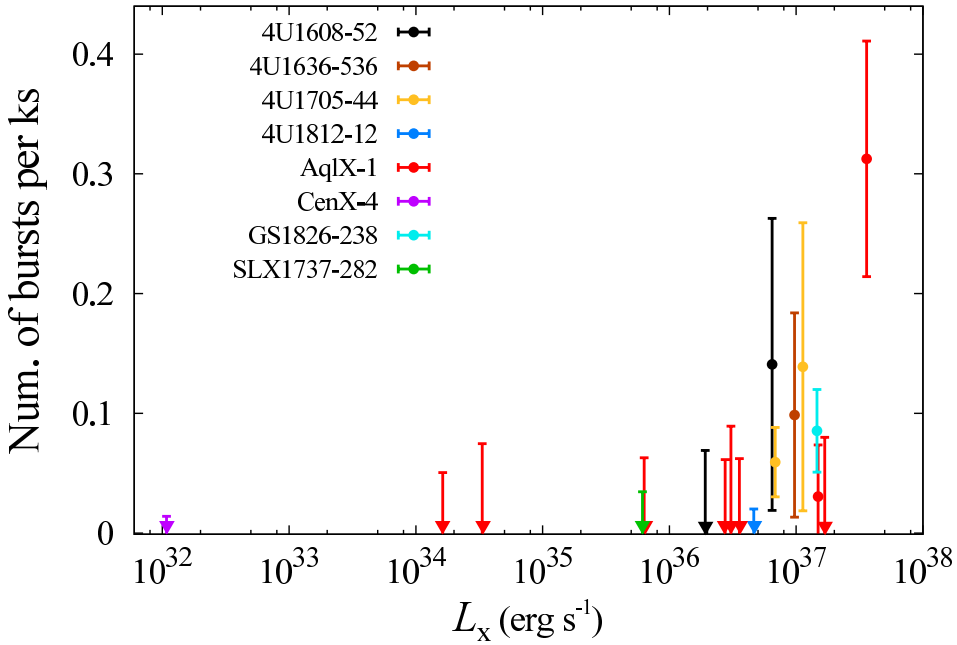

Figure 6.10: The number of bursts of the sample data sets, divided by each exposure (table 4.1). The errors are taken as $\sqrt{\text{number} + 1}$, approximated as Poisonnian at smaller rates.

6.4.3 Magnetic field strength

In the low luminosity regime of $L_{\rm x} < 0.01 L_{\rm edd}$, we obtained the small values of $R_{\rm bb}$ (< 10 km) and $\sqrt{g\eta}R_0$ (§6.2.3). As an interpretation of these, the emergence of a magnetosphere is preferred since it can explain both (§6.2.4). This important influence must be examined carefully.

An independent examination was given by Matsuoka & Asai (2013). Figure 6.11 shows light curves of three recent outbursts of Aql X-1 taken with *MAXI*. displaying recent three outbursts. Thus, the flux-decrease time always gets progressively shorter and shorter in its decay phase, in a sharp contrast to black-hole transients which are usually characterized by exponential decays (e.g. Kitamoto et al. 1992). Matsuoka and Asai investigated these luminosity distributions together with those of 4U1608-52, and concluded that the drop is due to the propeller effect (Lamb et al. 1973): the Alfven radius of equation 6.16 will become larger than the "co-roration radius" (where the

Keplerian angular frequency of the accreting matter become equal to that of the NS rotation), and hence $\dot{M}$ is strongly suppressed by the magnetic pressure and the cetrifugal force. Assuming $R_{\rm A} \gg 10$ km at $L_{\rm x} < 10^{36}$ erg s $^{-1}$, they estimated the magnetic field strength of $B \sim 10^8$ G, which is a gross agreement with our estimate.

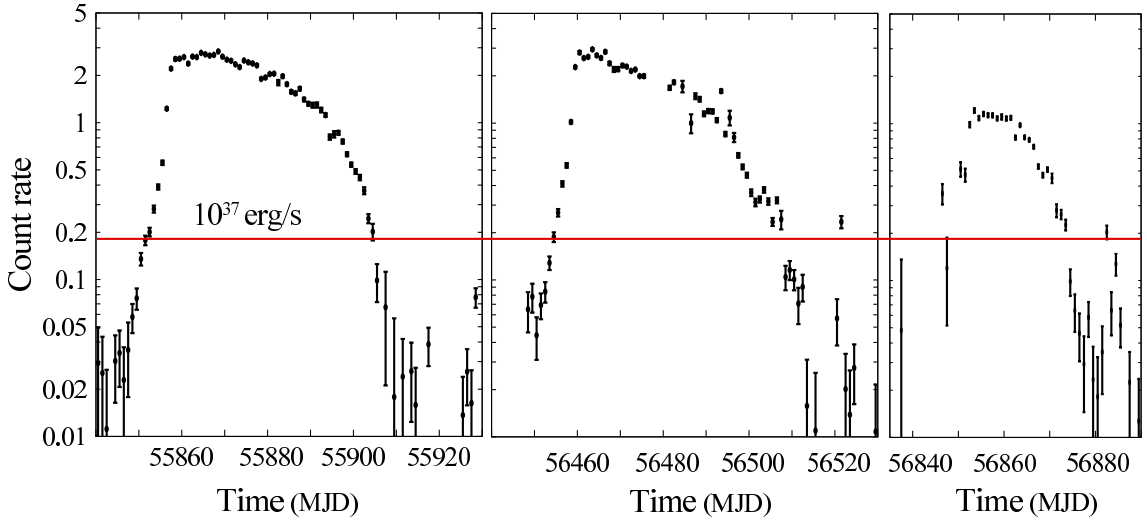

Figure 6.11: Light curves of three outbursts of Aql X-1 (in 2011, 2013, and 2014), taken with *MAXI*/GSC. The employed energy range is $2 - 20$ keV.

The rapid outburst decay is also clear in our data sets. In figure 5.1, the severn spectra were acquired with an approximately the same interval of $4 - 6$ days, but the intensity drop is observed to be very large from Obs-D4 through Obs-D5 to the last two observations. To visualize this, figure 6.12 plots the XIS count rate (In table 4.2) as a function of the elapsed day from Obs-D1. This is consistent with the *MAXI* results, although at that time *MAXI* had not yet been launched onto the International Space Station.

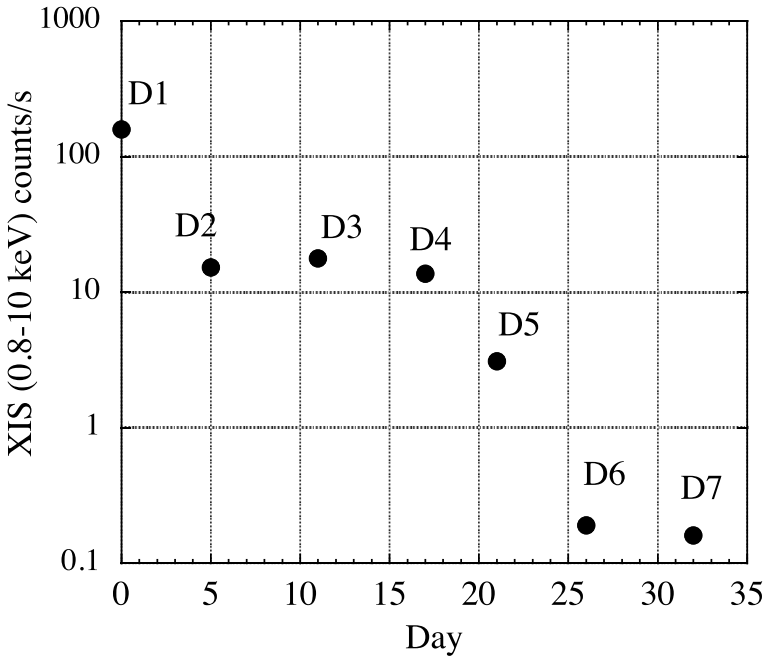

Figure 6.12: A light curve of Aql X-1 in the decaying phase (Obs-D1 to D7). The vertical axis denotes the mean count rates of XIS0 (table 4.2). The time origin is that of Obs-D1.

As a similar example of this case, accreting millisecond X-ray pulsars (AMXPs; e.g. Patruno & Watts 2012, for review) are worth noting. AMXPs are a subgroup of LMXBs, which exhibit X-ray pulsation, with a frequency of $100 - 1000$ Hz. The pulsating X-ray emission is considered to originate from a hot spot on the NS, created by a funneled flow by magnetic fields of $B \sim$ several$\times 10^8$ G or lower (e.g. Di Salvo & Burderi 2003). About 15 AMXPs, such as SAXJ1808.4-3658 (Wijnands & van der Klis 1998) and XTE J1751 —305 (Markwardt et al. 2002), have been found so far. They are observed in the hard state (Patruno & Watts 2012) with $L_{\rm x} \sim 10^{36}$ erg s^{-1}, showing power-law-like spectra (Gilfanov et al. 1998; Gierlinski & Poutanen 2005) which can be possibly expressed by Comptonized BB (Poutanen & Gierlinski 2003). Thus, by an analogy to them, we may expect coherent pulsations also in the normal LMXBs with $L_{\rm x} < 10^{36}$ erg s^{-1}. However, the pulsation has been found so far only from a small number of LMXBs. This is due to; expected small pulse fraction, the low source intensity at $L_{\rm x} \lesssim 10^{36}$ erg s^{-1}, and a need for very accurate corrections of the X-ray arrival times for the orbital Doppler effects (often using rather uncertain orbital elements of the target LMXB).

6.4.4 Chemical composition

Since a companion in an LMXB is usually a main-sequence star, the accreting matter is thought to consist of H ($\sim 75\%$ in weight) and He ($\sim 24\%$). Although we have ignored

chemical composition of accreting matters so far, their effects should be also examined, because a companion can have a H-depleted outer layer, due to some mass exchange effects.

Let us consider the case wherein the hydrogen is all replaced by heavier materials, for instance, helium. Although the optically-thick components (`diskBB` and BB) should not change in principle, a possible effect will appear in the corona. Since the number of electrons per nucleon is halved, the coronal opacity should be half that in an H-dominant system with the same $\dot{M}$. Hence the apparent change will be in the optical depth.

How will the coronal $T_{\rm e}$ be affected? The electron cooling rate by the BB photons depends on A/Z(=protons producing BB photons vs. electrons scattering them) where A is the mass number and Z is the atomic number of the coronal material. On the other hand, the electrons are heated by protons via Coulomb collision. The approximate energy transfer per scattering does not depend on A, because

$$\epsilon = E_{\rm i} \times \frac{m_{\rm e}}{m_{\rm i}} \propto (AE_0) \times \frac{m_{\rm e}}{A} = \text{const.} \tag{6.23}$$

The collision cross-section is $\propto Z^2$ and the number of ions per electron is $\propto Z^{-1}$. As a result, the ratio of the electron heating to cooling becomes proportional to

$$\frac{Z^2 \times Z^{-1}}{(A/Z)} = \frac{Z^2}{A}. \tag{6.24}$$

This predicts that an LMXB with a C/O-rich donor ($Z \geq 6, A \sim 2Z$) should exhibit higher $T_{\rm e}$ than the normal LMXBs. Thus, these effects can be behind the values of τ and $T_{\rm e}$ in figure 6.3, although the quantitative evaluation above may not be accurate.

Actually, as an extreme case, the ultra-compact X-ray binary 4U0614+091 which has a CO or ONe white dwarf as a mass donor (Nelemans et al. 2006), exhibits quite low optical depth of $\tau \sim 0.26$ and high $T_{\rm e}$ (~ 160 keV) in the hard state with $L_{\rm x} \sim 10^{37}$ erg s^{-1} (Piraino et al. 1999). These values are significantly deviated from those at the same $L_{\rm x}$ range in figure 6.3 ($\tau \gtrsim 1$ and $T_{\rm e} \sim 20$ keV). This might be a result of an effect like what we considered above.

Chapter 7

CONCLUSION

In the present thesis, we have investigated 17 *Suzaku* spectra of 8 LMXBs focusing mainly on their hard state. Thanks to the broad-band capability of *Suzaku*, we have obtained a comprehensive scenario that can explain the wide-band hard-state spectra from < 1 keV to $\gtrsim 100$ keV over a vast range of luminosity as 10^{32} erg s^{-1} $\leq L_{\rm x} < 10^{38}$ erg s^{-1}. The outcome can be summarized as follows.

1. In the wide range of luminosity, hard-state spectra of our sample LMXBs are all explained by at most three spectral components: the disk emission, blackbody from the NS surface, and Comptonization. The BB emission is always Comptonized, whereas the disk emission is affected only in a certain luminosity range ($L_{\rm x} \sim 10^{37}$ erg s^{-1}).

2. When $L_{\rm x} \gtrsim 10^{36}$ erg s^{-1}, the optically-thick disk transforms, at a radius of $R_{\rm in} > 20$ km, into an optically-thin and geometrically-thick flow (corona) with an electron temperature of $T_{\rm e} = 20 \sim 60$ keV. The flow plunges rather spherically onto the NS surface, and make the entire surface ($R_{\rm bb} \sim 10$ km) emit BB radiation with $T_{\rm bb} \sim 0.5$ keV. The BB photons are strongly ($y = 0.6 \sim 1.4$) Comptonized by the succeeding corona.

3. As $L_{\rm x}$ becomes lower than 10^{36} erg s $^{-1}$, apparent $R_{\rm bb}$ becomes significantly and progressively smaller than 10 km. In addition, the relation between τ and $L_{\rm x}$ indicates that the flow cross-section and/or radial velocity decrease at low $L_{\rm x}$. These phenomena can be explained either by the color hardening of the BB together with the decrease of radial infall velocity, or the emergence of a magnetosphere and consequent funneling of the flow onto the magnetic poles. The latter is preferred since it can explain the two phenomena simultaneously, although it needs to be further examined from another point of view. Assuming the latter hypothesis

and that the gravitational pressure decreases, at $L_{\rm x} \sim 10^{36}$ erg s^{-1}, to a level comparable to the magnetic pressure, a field strength of $\gtrsim 10^7$ G is inferred.

4. The spectral parameters of the hard state ($T_{\rm in}, R_{\rm in}, T_{\rm bb}, T_{\rm e}$, and y) were found to smoothly connect to those in the soft state. Across the transition, the ratio $Q \equiv T_{\rm e}/T_{\rm bb}$ (> 5 in the hard state and < 5 in the soft state) and the fractional disk luminosity (increasing towards the soft state) change rather quickly, but still continuously. All LMXBs share a common locus on the (Q, y) plane.

These results provide novel understanding of the hard-state LMXBs. The advent of *ASTRO-H* in the FY2015 will push the study further forward, with its wide-band capability and high sensitivity which far exceed those of *Suzaku*.

Acknowledgement

I would like to first appreciate Prof. Kazuo Makishima and Ass. Prof. Kazuhiro Nakazawa. Prof. K. Makishima has enormous contribution to this thesis by giving me advice on the entire construction and revising the whole text. During my five-year of the master/doctor course, he has taught me the importance of the fundamental physics, and a way of thinking as an experimental physicist. His admirable dedication to science and education has made me realize what it means to be a professional. Ass. Prof. K. Nakazawa helped and encouraged me writing master/doctor thesis, and supported me in experiments of the *ASTRO-H* mission. My gratitude for the two supervisors is anyhow beyond description.

I also thank Dr. H. Takahashi and Prof. M. Matsuoka for giving me many precious comments In the present thesis and other papers. Dr. S. Yamada, Dr. H. Noda, and S, Torii taught me basic accretion physics around a BH/NS and how to analyze *Suzaku* data when I entered this laboratory. Dr. Z. Zhang and K. Ono have reviewed this thesis and cross-checked the results. The other laboratory members gave valuable comments for the presentation. I am quite grateful to Dr. T. Yuasa and Dr. H. Odaka, from whom I learned the basic of software coding. They helped me many times in my master thesis and *ASTRO-H* experiments.

And my colleagues, (Dr.) M. Sasano and (Dr.) T. Nakano, have been necessary for my five years in the graduate school. They, together with Dr. H. Uchiyama and so-called "M2s (emni:z)" people (Dr. H. Noda, H. Nishioka, K. Nakajima, and S. Torii), always entertained me and gave spice to my life in the laboratory.

Finally, I appreciate my family and other people around for supporting me ever since.

Bibliography

Anders, E. & Ebihara, M. 1982, Geochimica et Cosmochimica Acta, 46, 2363

Barret, D., Olive, J. F., Boirin, L., et al. 2000, The Astrophysical Journal, 533, 329

Barret, D., Olive, J. F., & Oosterbroek, T. 2003a, Astronomy and Astrophysics, 400, 643

Barret, D., Olive, J. F., & Oosterbroek, T. 2003b, Astronomy and Astrophysics, 400, 643

Barthelmy, S. D., Barbier, L. M., Cummings, J. R., et al. 2005, Space Science Reviews, 120, 143

Belian, R. D., Conner, J. P., & Evans, W. D. 1976, The Astrophysical Journal, 206, L135

Boella, G., Butler, R. C., Perola, G. C., et al. 1997, Astronomy and Astrophysics Supplement Series, 122, 299

Boldt, E. 1987, Observational Cosmology, 124, 611

Bradt, H. V., Rothschild, R. E., & Swank, J. H. 1993, Astronomy and Astrophysics Supplement Series, 97, 355

Burderi, L., Di Salvo, T., Lavagetto, G., et al. 2007, The Astrophysical Journal, 657, 961

Cackett, E. M., Brown, E. F., Miller, J. M., & Wijnands, R. 2010, The Astrophysical Journal, 720, 1325

Campana, S., Mereghetti, S., Stella, L., & Colpi, M. 1997, Astronomy and Astrophysics, 324, 941

Casella, P., Altamirano, D., Patruno, A., Wijnands, R., & van der Klis, M. 2008, The Astrophysical Journal, 674, L41

Chevalier, C., Ilovaisky, S. A., Leisy, P., & Patat, F. 1999, Astronomy and Astrophysics, 347, 4

Chevalier, C., Ilovaisky, S. A., van Paradijs, J., Pedersen, H., & van der Klis, M. 1989, Astronomy and Astrophysics, 210, 114

Christian, D. J. & Swank, J. H. 1997, The Astrophysical Journal Supplement Series, 109, 177

Cocchi, M., Bazzano, A., Natalucci, L., et al. 2000, Astronomy and Astrophysics, 357, 527

Cocchi, M., Farinelli, R., & Paizis, A. 2011, Astronomy & Astrophysics, 529, A155

Cornelisse, R., in 't Zand, J. J. M., Verbunt, F., et al. 2003, Astronomy and Astrophysics, 405, 1033

Cumming, A. 2004, Nuclear Physics B - Proceedings Supplements, 132, 435

Czerny, M., Czerny, B., & Grindlay, J. E. 1987, The Astrophysical Journal, 312, 122

Di Salvo, T. & Burderi, L. 2003, Astronomy and Astrophysics, 397, 723

Egron, E., Di Salvo, T., Motta, S., & Burderi, L. 2011, Extreme and Variable High Energy Sky (Extremesky 2011), -1, 15

Farinelli, R., Titarchuk, L., Paizis, A., & Frontera, F. 2008, The Astrophysical Journal, 680, 602

Feast, M. 1999, New Views of the Magellanic Clouds, 190, 542

Fender, R. P. & Hendry, M. A. 2000, Monthly Notices of the Royal Astronomical Society, 317, 1

Fiocchi, M., Bazzano, A., Ubertini, P., & Jean, P. 2006, The Astrophysical Journal, 651, 416

Fiocchi, M., Bazzano, A., Ubertini, P., & Zdziarski, A. A. 2007, The Astrophysical Journal, 657, 448

Forman, W., Jones, C., Cominsky, L., et al. 1978, The Astrophysical Journal Supplement Series, 38, 357

Fukazawa, Y., Mizuno, T., Watanabe, S., et al. 2009, Publications of the Astronomical Society of Japan, 61, S17

Fukue, J. & Umemura, M. 1994, Publications of the Astronomical Society of Japan, 46, 87

Galloway, D. K., Muno, M. P., Hartman, J. M., Psaltis, D., & Chakrabarty, D. 2008, The Astrophysical Journal Supplement Series, 179, 360

Galloway, D. K., Psaltis, D., Chakrabarty, D., & Muno, M. P. 2003, The Astrophysical Journal, 590, 999

Giacconi, R., Gursky, H., Paolini, F., & Rossi, B. 1962, Physical Review Letters, 9, 439

Giacconi, R., Kellogg, E., Gorenstein, P., Gursky, H., & Tananbaum, H. 1971, The Astrophysical Journal, 165, L27

Gierlinski, M. & Done, C. 2002, Monthly Notices of the Royal Astronomical Society, 337, 1373

Gierlinski, M. & Poutanen, J. 2005, Monthly Notices of the Royal Astronomical Society, 359, 1261

Gilfanov, M., Revnivtsev, M., Sunyaev, R., & Churazov, E. 1998, Astronomy and Astrophysics, 338, L83

Guainazzi, M., Parmar, A. N., Segreto, A., et al. 1998, Astronomy and Astrophysics, 339, 802

Haberl, F. & Titarchuk, L. 1995, Astronomy and Astrophysics, 299, 414

Hasinger, G. & van der Klis, M. 1989, Astronomy and Astrophysics, 225, 79

Hayashi, C., Hshi, R., & Sugimoto, D. 1962, Progress of Theoretical Physics Supplement, 22, 1

in 't Zand, J. J. M., Heise, J., Kuulkers, E., et al. 1999, Astronomy and Astrophysics, 347, 891

in 't Zand, J. J. M., Verbunt, F., Kuulkers, E., et al. 2002, Astronomy and Astrophysics, 389, L43

Ishida, M. 2006, Suzaku Memo

Ishida, M. 2007, Suzaku Memo

Jonker, P. G. & Nelemans, G. 2004, Monthly Notices of the Royal Astronomical Society, 354, 355

Kitamoto, S., Tsunemi, H., Miyamoto, S., & Hayashida, K. 1992, The Astrophysical Journal, 394, 609

Kitamoto, S., Tsunemi, H., Miyamoto, S., & Roussel-Dupre, D. 1993, The Astrophysical Journal, 403, 315

Kokubun, M., Makishima, K., Takahashi, T., et al. 2007, Publications of the Astronomical Society of Japan, 59, S53

Kompaneets, A. 1956, Zh.E.F.T.

Kondo, I., Inoue, H., Koyama, K., et al. 1981, Space Science Instrumentation, 5, 211

Koyama, K., Inoue, H., Makishima, K., et al. 1981, The Astrophysical Journal, 247, L27

Koyama, K., Tsunemi, H., Dotani, T., et al. 2007, Publications of the Astronomical Society of Japan, 59, S23

Kubota, A., Tanaka, Y., Makishima, K., et al. 1998, Publications of the Astronomical Society of Japan, 50, 667

Kuulkers, E., Homan, J., van der Klis, M., Lewin, W. H. G., & Mndez, M. 2002, Astronomy and Astrophysics, 382, 947

Lamb, F. K., Pethick, C. J., & Pines, D. 1973, The Astrophysical Journal, 184, 271

Lavagetto, G., Iaria, R., Di Salvo, T., et al. 2004, Nuclear Physics B - Proceedings Supplements, 132, 616

Lightman, A. P. & Eardley, D. M. 1974, The Astrophysical Journal, 187, L1

Lightman, A. P. & White, T. R. 1988, The Astrophysical Journal, 335, 57

Lightman, A. P. & Zdziarski, A. A. 1987, The Astrophysical Journal, 319, 643

Lightman, A. P., Zdziarski, A. A., & Rees, M. J. 1987, The Astrophysical Journal, 315, L113

Lin, D., Remillard, R. a., & Homan, J. 2007, The Astrophysical Journal, 667, 1073

Lin, D., Remillard, R. a., & Homan, J. 2010, The Astrophysical Journal, 719, 1350

Liu, Q. Z., van Paradijs, J., & van den Heuvel, E. P. J. 2007, Astronomy and Astrophysics, 469, 807

Lochner, J. C. & Roussel-Dupre, D. 1994, The Astrophysical Journal, 435, 840

Lynden-Bell, D. 1969, Nature, 223, 690

Lyu, M., Mendez, M., Sanna, A., et al. 2014, Monthly Notices of the Royal Astronomical Society, 440, 1165

Maeda, Y. 2008, Suzaku Memo

Magdziarz, P. & Zdziarski, A. A. 1995, Monthly Notices of the Royal Astronomical Society, 273, 837

Mainardi, L. I., Paizis, A., Farinelli, R., et al. 2010, Astronomy and Astrophysics, 512, A57

Makino, F. 1987, Astrophysical Letters, 25, 223

Makino, F. 1988, International Astronomical Union Circular, 4653, 2

Makishima, K. 2014, 40th COSPAR Scientific Assembly. Held 2-10 August 2014, in Moscow, Russia, Abstract E1.1-1-14., 40, 1953

Makishima, K., Ishida, M., Ohashi, T., et al. 1989, Publications of the Astronomical Society of Japan, 41, 531

Makishima, K., Kubota, A., Mizuno, T., et al. 2000, The Astrophysical Journal, 535, 632

Makishima, K., Maejima, Y., Mitsuda, K., et al. 1986, The Astrophysical Journal, 308, 635

Makishima, K., Takahashi, H., Yamada, S., et al. 2008, Publications of the Astronomical Society of Japan, 60, 585

Markwardt, C. B., Swank, J. H., Strohmayer, T. E., Zand, J. J. M. i. ., & Marshall, F. E. 2002, The Astrophysical Journal, 575, L21

Matsuoka, M. & Asai, K. 2013, Publications of the Astronomical Society of Japan, 65, 26

Mineshige, S., Tsuribe, T., & Umemura, M. 1998, Publications of the Astronomical Society of Japan, 50, 233

Mitsuda, K., Bautz, M., Inoue, H., et al. 2007, Publications of the Astronomical Society of Japan, 59, S1

Mitsuda, K., Inoue, H., Koyama, K., et al. 1984, Publications of the Astronomical Society of Japan, 36, 741

Mitsuda, K., Inoue, H., Nakamura, N., & Tanaka, Y. 1989, Publications of the Astronomical Society of Japan, 41, 97

Mitsuda, K. & Tanaka, Y. 1986, NATO Advanced Science Institutes (ASI) Series C, 167, 195

Morrison, R. & McCammon, D. 1983, The Astrophysical Journal, 270, 119

Mück, B., Piraino, S., & Santangelo, A. 2013, Astronomy & Astrophysics, 555, A17

Muno, M. P., Belloni, T., Dhawan, V., et al. 2005, The Astrophysical Journal, 626, 1020

Murakami, T., Inoue, H., Koyama, K., et al. 1980, The Astrophysical Journal, 240, L143

Nakamura, N., Dotani, T., Inoue, H., et al. 1989, Publications of the Astronomical Society of Japan, 41, 617

Nelemans, G., Jonker, P. G., & Steeghs, D. 2006, Monthly Notices of the Royal Astronomical Society, 370, 255

Odaka, H., Aharonian, F., Watanabe, S., et al. 2011, The Astrophysical Journal, 740, 103

Orosz, J. A. & Kuulkers, E. 1999, Monthly Notices of the Royal Astronomical Society, 305, 132

Patruno, A. & Watts, A. L. 2012, ARXIV

Piraino, S., Santangelo, A., Ford, E. C., & Kaaret, P. 1999, Astronomy and Astrophysics, 349, L77

Poutanen, J. & Gierlinski, M. 2003, Monthly Notices of the Royal Astronomical Society, 343, 1301

Poutanen, J. & Svensson, R. 1996, The Astrophysical Journal, 470, 249

Pringle, J. E., Rees, M. J., & Pacholczyk, A. G. 1973, Astronomy and Astrophysics, 29, 179

Raichur, H., Misra, R., & Dewangan, G. 2011, Monthly Notices of the Royal Astronomical Society, 416, no

Sakano, M., Koyama, K., Murakami, H., Maeda, Y., & Yamauchi, S. 2002, The Astrophysical Journal Supplement Series, 138, 19

Sakurai, S., Torii, S., Noda, H., et al. 2014, Publications of the Astronomical Society of Japan, 66, 10

Sakurai, S., Yamada, S., Torii, S., et al. 2012, Publications of the Astronomical Society of Japan, 64, 72

Sasano, M., Makishima, K., Sakurai, S., Zhang, Z., & Enoto, T. 2014, Publications of the Astronomical Society of Japan, 66, 35

Savolainen, P., Hannikainen, D. C., Vilhu, O., et al. 2009, Monthly Notices of the Royal Astronomical Society, 393, 569

Serlemitsos, P. J. 1988, Applied optics, 27, 1447

Serlemitsos, P. J., Soong, Y., Chan, K.-W., et al. 2007, Publications of the Astronomical Society of Japan, 59, S9

Shakura, N. I. & Sunyaev, R. A. 1973, Astronomy and Astrophysics, 24, 337

Shapiro, S. L., Lightman, A. P., & Eardley, D. M. 1976, The Astrophysical Journal, 204, 187

Shimura, T. & Takahara, F. 1995, The Astrophysical Journal, 445, 780

Simon, V. 2002, Astronomy and Astrophysics, 381, 151

Skinner, G. K., Willmore, A. P., Eyles, C. J., et al. 1987, Nature, 330, 544

Strider, L., Briel, U., Dennerl, K., et al. 2001, Astronomy and Astrophysics, 365, L18

Sugizaki, M., Yamaoka, K., Matsuoka, M., et al. 2013, Publications of the Astronomical Society of Japan, 65, 58

Takahashi, H. 2004, Ph.D thesis

Takahashi, H., Sakurai, S., & Makishima, K. 2011, The Astrophysical Journal, 738, 62

Takahashi, T., Abe, K., Endo, M., et al. 2007, Publications of the Astronomical Society of Japan, 59, S35

Tanaka, Y., Fujii, M., Inoue, H., et al. 1984, Publications of the Astronomical Society of Japan, 36, 641

Tanaka, Y., Inoue, H., & Holt, S. S. 1994, Publications of the Astronomical Society of Japan, 46, L37

Tarana, A., Bazzano, A., & Ubertini, P. 2008, The Astrophysical Journal, 688, 1295

Tarana, A., Bazzano, A., Ubertini, P., et al. 2006, Astronomy and Astrophysics, 448, 335

Tarana, A., Belloni, T., Bazzano, A., Méndez, M., & Ubertini, P. 2011a, Monthly Notices of the Royal Astronomical Society, 416, 873

Tarana, a., Belloni, T., Bazzano, a., Méndez, M., & Ubertini, P. 2011b, Monthly Notices of the Royal Astronomical Society, 416, 873

Turner, M. J. L., Abbey, A., Arnaud, M., et al. 2001, Astronomy and Astrophysics, 365, L27

Ubertini, P., Bazzano, A., Cocchi, M., et al. 1999, The Astrophysical Journal, 514, L27

Umemura, M. & Fukue, J. 1994, Publications of the Astronomical Society of Japan, 46, 567

Weisskopf, M. C., Tananbaum, H. D., Van Speybroeck, L. P., & O'Dell, S. L. 2000, X-Ray Optics, Instruments, and Missions III, 4012, 2

White, N. & Mason, K. 1985, Space Science Reviews, 40, 167

White, N. E. & Peacock, A. 1988, Memorie della Societa Astronomica Italiana, 59, 7

White, T. R., Lightman, A. P., & Zdziarski, A. A. 1988, The Astrophysical Journal, 331, 939

Wijnands, R. & van der Klis, M. 1998, Nature, 394, 344

Wilson, C. A., Patel, S. K., Kouveliotou, C., et al. 2003, The Astrophysical Journal, 596, 1220

Winkler, C., Courvoisier, T. J.-L., Di Cocco, G., et al. 2003, Astronomy and Astrophysics, 411, L1

Yamada, S., Uchiyama, H., Dotani, T., et al. 2012, Publications of the Astronomical Society of Japan, 64, 53

Zdziarski, A. A., Johnson, W. N., & Magdziarz, P. 1996, Monthly Notices of the Royal Astronomical Society, 283, 15

Zhang, W., Jahoda, K., Kelley, R. L., et al. 1998, The Astrophysical Journal, 495, L9

Zhang, Z., Makishima, K., Sakurai, S., Sasano, M., & Ono, K. 2014, Publications of the Astronomical Society of Japan

Zycki, P. T., Done, C., & Smith, D. A. 1999, Monthly Notices of the Royal Astronomical Society, 309, 561